Understanding the Origin of Planetary Systems: Studying the Kuiper Belt and the Dynamics of Planet Formation

Thesis by

Hilke Elisabeth Schlichting

In Partial Fulfillment of the Requirements

for the Degree of

Doctor of Philosophy

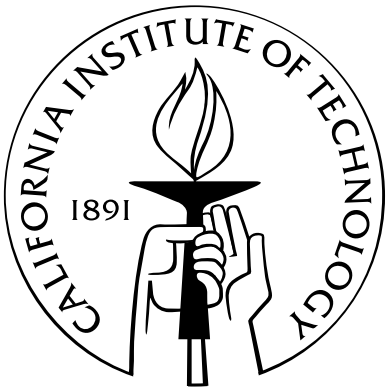

California Institute of Technology

Pasadena, California

2009

(Defended May 22, 2009)

To all children in this world, especially girls, who never had the opportunity to go to school.

Acknowledgements

First and foremost, I would like to thank my advisor, Re'em Sari, who is primarily responsible for my growth and development as a scientist during my time at Caltech. It was a great privilege having had Re'em as my advisor; I very much enjoyed learning from someone with such great scientific insight and infectious enthusiasm. Thank you for all the lessons, your patience and support. I would like to thank Maayan and Re'em for their hospitality, and for taking such good care of me during my visits to Israel that I sometimes could not help but feel like the 5th child in the Sari family household. Thank you for enriching my life academically, culturally and personally.

I would like to thank Mike Brown for teaching an excellent class on 'The formation and Evolution of Planetary Systems' that helped to spark my interest in planet formation and the solar system. I also enjoyed participating in Mike's group meetings which offered a great opportunity to learn about the latest news from the Kuiper Belt and other exciting solar system objects.

I am grateful to Andrew Blain who gave me the opportunity to gain an insight into astrophysics research as a SURF student at Caltech while I was still an undergraduate at Cambridge.

I thank my thesis and candidacy defense committee for their time and efforts: Andrew Blain, Mike Brown, Lynne Hillenbrand, Marc Kamionkowski, and Re'em Sari.

I would like to thank Ranga-Ram Chary for all his love, encouragement and support. Thank you, Ranga, for all the joy and wonderful things that you bought into my life. I am so glad that I met you and cannot imagine that there was once a life without you and without masala chai!

I am very grateful to my parents, especially, for their support, for my cosmopolitan upbringing, and for letting me pursue my goals and dreams. Thank you Mama for being so affectionate and loving. Thank you Sigrid for being the best sister in the world!

In addition, I would like to thank Radha and Dipak Basu for many fun and relaxing moments at their beautiful residence in the Bay Area.

There have been numerous people and colleagues that had a significant impact on my academic life and I cannot possibly list them all here. Nevertheless, I do want to mention my 6th form physics teacher Ian Taylor. His confidence in my scientific abilities and his encouragement to apply to Oxbridge had a tremendous impact on my life.

While at Caltech, I had a lot of fun, inspiring scientific discussions with, and received valuable help and advice from many colleagues and friends. I am particularly grateful to Eran Ofek, Orly Gnat, Ben Collins, Margaret Pan, Johan Richard and Karín Menéndez-Delmestre.

Abstract

This thesis presents theoretical and observational studies pertaining to the early solar system, planet formation and extrasolar planets.

First, we explore the dynamics of protoplanet formation. We find that the growth of protoplanets may be dominated by the accretion of a planetesimal disk that forms from planetesimal-planetesimal collisions, rather than direct planetesimal impacts onto the protoplanet. This has far reaching implications for the formation of planets, their growth rate and dynamics. We focus on the implications for planetary spins: it can explain the prevalence of prograde spins of planets and asteroids in the solar system, which is commonly believed to be an accident.

Second, we present a series of investigations of the formation of multiple systems in the Kuiper Belt. Two of our studies are concerned with the formation of comparable mass binaries. We find that in a dynamically cold Kuiper Belt, binaries become bound predominantly by dynamical friction. This leads to a binary population with mostly retrograde mutual binary orbits. In a dynamically hot Kuiper Belt three-body gravitational interactions dominate the binary formation producing a roughly equal number of prograde and retrograde binaries.

We propose a new formation scenario for Haumea's collisional family. In our scenario, the family members are ejected while in orbit around Haumea rather than directly from Haumea's surface as previously proposed. Our formation scenario offers an explanation for the observed velocity dispersion among the family members which is much smaller than Haumea's escape velocity. It is consistent with detecting just one collisional family in the Kuiper Belt and aids with explaining Haumea's initial giant impact.

We conclude with observational work that aims to detect sub-km sized Kuiper Belt objects and to measure their size-distribution. Our results provide the best constraint on the surface density of small Kuiper Belt objects to date. Our findings support the idea that small Kuiper Belt objects underwent collisional evolution that modified their size distribution. We present our first candidate occultation event and show that it is unlikely to be due to instrumental artifacts or statistical fluctuations in the data.

Contents

List of Figures

List of Tables

Chapter 1

Introduction

The study of the solar system is thousands of years old and one of the oldest branches of astronomy. Some of the most prominent scientists of the past, Copernicus, Kepler, Galilei, Newton, just to name a few, dedicated their lives to the study of the bodies in the solar system and their dynamics. Despite its far-reaching past, research concerned with the solar system and planet formation continues to strive. Three scientific discoveries in the last two decades are chiefly responsible for sparking an augmented interest in the origin of our solar system and planet formation, and created new research areas within the field of astronomy and astrophysics.

The first was the discovery of the first Kuiper Belt object (KBO) in our solar system (Jewitt et al., 1992). The Kuiper Belt consists of a disk of icy objects and is located at $\sim$ 40 AU just beyond the orbit of Neptune. To date, more than 1000 KBOs have been discovered and dedicated surveys revealed the intricate dynamical structure of the Kuiper Belt (see Fig. 1.1) (Malhotra et al., 2000), investigated the multiplicity of KBOs (e.g., Noll et al., 2008), and measured their size-distribution (e.g., Bernstein et al., 2004). In the Kuiper belt, planet formation never reached completion because the runaway growth of the planetary embryos was interrupted by an increase in velocity dispersion of the planetesimals. Studying the Kuiper belt, therefore, opens a new window into understanding the conditions in the early solar system during the formation of its members.

The second discovery was the detection of the first planet orbiting a Sun-like star outside our solar system (Mayor & Queloz, 1995). The number of detected extrasolar

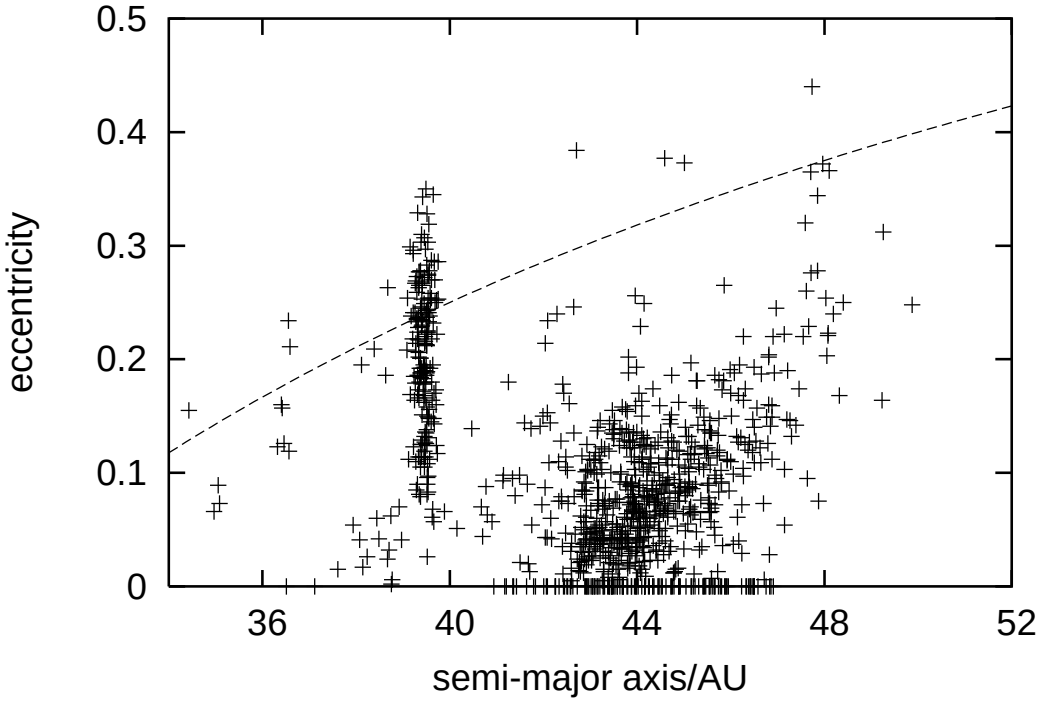

Figure 1.1 Eccentricity vs. semi-major axis of Trans-Neptunian objects. Everything above the dashed line is on Neptune-crossing orbits. The cluster of objects at $\sim$ 39 AU corresponds to the Plutinos which are in the 3:2 mean-motion resonance with Neptune. The 2:1 mean-motion resonance is located at $\sim$ 48 AU. The population of classical KBOs is located between $\sim$ 40 AU and $\sim$ 48 AU on low eccentricity orbits. The eccentricity and semi-major axis information was retrieved from the *Minor Planet Center database.*

planets has risen to more than 300. These discoveries have revealed an unanticipated diversity of planetary systems and led to valuable insights into planet formation. One of the many striking features of the extrasolar planetary systems discovered to date is their orbital architecture with Jupiter-mass planets orbiting their parent star at a fraction of an AU, which is vastly different from that of our own solar system (see Fig. 1.2). Extrasolar planet searches have already revealed an intriguing correlation between the host-star metallicity and the planet occurance rate (Santos et al., 2004; Fischer & Valenti, 2005), they have measured the spin-orbit alinement of about a dozen transiting systems using the Rossiter-McLaughlin effect (e.g., Fabrycky & Winn, 2009), and continue to probe new parameter space as they become sensitive to ever-smaller planet masses.

The third discovery was the detection of circumstellar disks. Both the spectral energy distribution and spatially resolved images of circumstellar gas and dust disks provide valuable constraints for planet formation theories. For example, the ubiquity of circumstellar gas disks around young stars suggests that planet formation might be common. Observations find a gas disk dissipation timescale of a few million years (e.g., Haisch et al., 2001; Hillenbrand, 2008). This places strong constraints on the formation timescale of gaseous planets and their proposed formation scenarios. In a few cases, detailed information on the disk composition, size and mass are available. In addition, several debris disks have been discovered around main-sequence stars (e.g., Stapelfeldt et al., 2004; Greaves et al., 2005; Kalas et al., 2005). These debris disks provide a valuable link between extrasolar planetary systems and the Kuiper Belt in our own solar system.

The wealth of observational discoveries related to extrasolar planets, circumstellar disks and the Kuiper Belt provide unprecedented constraints on planet formation theories.

This thesis consists of a series of theoretical and one observational projects related to the formation of planets and the origin of our solar system.

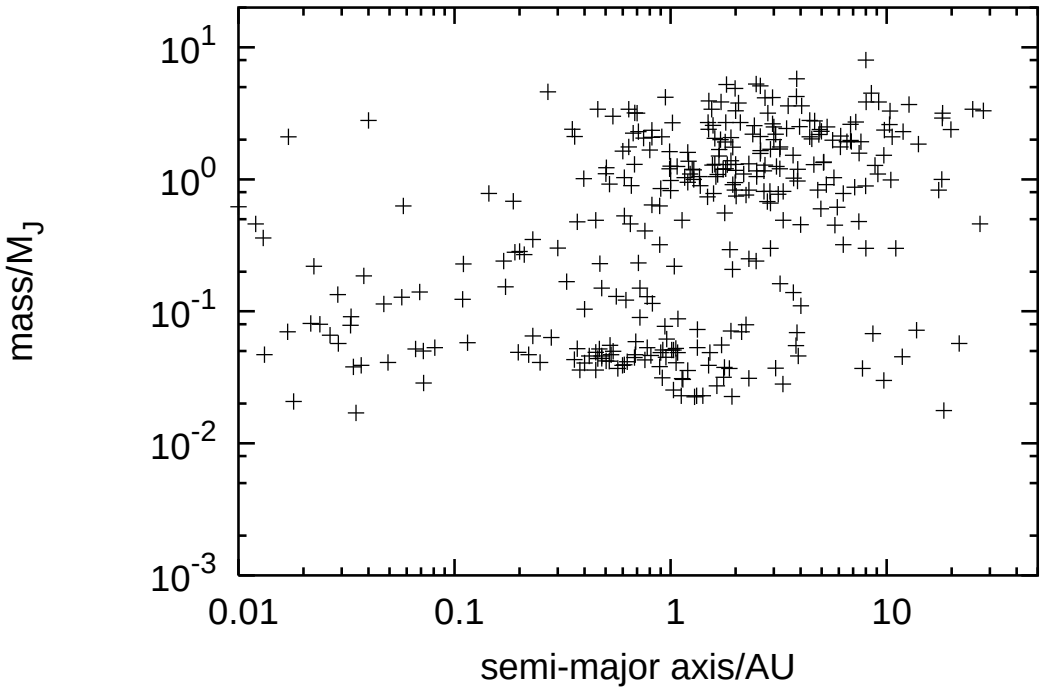

Figure 1.2 Planet mass, in units of Jupiter-masses, as a function of semi-major axis of all the extrasolar planets discovered as of 10th April 2009. In most cases, the planet mass should be regarded as a lower limit of the actual mass, since the majority of the planets were discovered by radial velocity searches. Many extrasolar planetary systems harbor Jupiter-mass planets within 1 AU of the parent star. The mass and semi-major axis information was retrieved from the *Extrasolar Planet Encyclopedia database.*

1.1 Planetesimal Accretion

The first project presented in this thesis investigates the dynamics of planetesimal accretion during the early stages of planet formation. Protoplanets grow by the accretion of small planetesimals. When planetesimals are accreted, they deliver mass and angular momentum to the growing protoplanet. This accretion is usually treated as collisionless, assuming that planetesimal-planetesimal collisions can be neglected while they are within the Hill sphere of the protoplanet. We show that, if planetesimals are small, of the order of a meter in size, then they are likely to collide within the protoplanet's sphere of gravitational influence, creating an accretion disk around the protoplanet. We study this new mode of planetesimal accretion and investigate its effects on the angular momentum distribution of planetary embryos and terrestial planets.

1.2 The Kuiper Belt

The Kuiper Belt with its dynamical structure, large binary population and tremendous color and albedo diversity contains many important clues related to planet formation processes in the early solar system. In addition, it is also a transitional structure that helps to relate our solar system to others. Several main-sequence stars have observed debris disks (e.g., Stapelfeldt et al., 2004; Greaves et al., 2005; Kalas et al., 2005) which are in many ways Kuiper Belt analogs. Studying and understanding the Kuiper Belt in our own solar system may, therefore, also provide insights into the formation and evolution of extrasolar planetary systems.

1.2.1 Binaries and Multiple Systems in the Kuiper Belt

One of the many intriguing discoveries in the Kuiper Belt is that a substantial fraction of its members are binaries. These binaries are particularly interesting to study since their existence is one of the important clues that suggests that the Kuiper Belt was not always dynamically hot and, hence, hostile to binary formation as it is today. The

binaries illuminate the conditions during their formation in the early solar system when the Kuiper Belt was still dynamically cold. The Kuiper Belt is a heaven for binary formation in the sense that for a given object the Hill sphere, which defines the region around a body within which a binary companion can exist, is 40 times larger at Kuiper Belt distances than it is at 1 AU. This, therefore, makes the Kuiper Belt an ideal place for binary formation provided that the velocity dispersion was sufficiently low (i.e., shear-dominated velocity regime). Broadly speaking, we can identify two classes of Kuiper Belt binaries. The first class consists of small satellites around the largest Kuiper Belt objects and the second of roughly equal mass binaries with wide separations. This second class of binaries with roughly equal mass and wide separation is unique to the Kuiper Belt. The dynamical properties of these binaries and their presence in the outer solar system is best explained by a dynamical origin, e.g., three-body gravitational interactions, rather than a collision. Chapters 3 and 4 describe formation processes of comparable mass Kuiper Belt binaries and possible observational signatures of the different scenarios. The 5th chapter in this thesis is concerned with the dwarf planet Haumea, its two moons and collisional family. Haumea is one of the largest objects in the Kuiper Belt and it is orbited by two small collisionally formed satellites. Small satellites are ubiquitous around the largest KBOs and these systems fall in the first class of binaries (Brown et al., 2006a; Brown & Suer, 2007), since their formation is best explained by a collision. Haumea, is thought to have undergone a giant impact that gave rise to Haumea's rapid rotation with a spin period of only 4 hours (Rabinowitz et al., 2006) and that created its multiple satellite system (Brown et al., 2005, 2006b) and collisional family (Brown et al., 2007). We present a new formation scenario for Haumea's collisional family in which the family members are ejected while in orbit around Haumea instead of being directly ejected from Haumea's' surface. We show that our formation scenario can explain the low velocity dispersion observed among its family members, that it is consistent with the abundance of one collisional family in the Kuiper Belt and that it aids with explaining Haumea's initial giant impact.

1.2.2 Detecting Sub-Km-Sized KBOs

KBOs are some of the least processed bodies in the solar system and their size distribution, especially that of large KBOs (i.e., $r > 50$ km), may provide insights into accretion processes in the early solar system. The size distribution of small KBOs (i.e., $r \lesssim 10$ km) was most likely modified by destructive collisions. If this is so, then the slope of the size distribution below the break is determined by the material properties of the KBOs. For example, the slope will be shallower if small KBOs are held together predominantly by gravity (i.e., they are effectively rubble piles) than if they are held together by material strength (Pan & Sari, 2005). The KBO radius at which the size distribution transitions from that of the small bodies to that of large KBOs sets the time span over which destructive collisions have been occurring in the Kuiper Belt. This, therefore, constrains the time at which the Kuiper Belt was excited from its originally dynamically cold to its current dynamically hot state. In Chapter 6 we describe our work on detecting and measuring the size distribution of sub-km sized KBOs. We search for serendipitous stellar occultations caused by small KBOs which enables us to probe KBOs with radii as small as ~ 250 m which corresponds to an R-band magnitude of 36.4. Our findings confirm that the size distribution of sub-km sized KBOs is shallower than that of large KBOs (i.e., $r > 50$km) and is consistent with the idea that small KBOs underwent collisional evolution that modified their size distribution.

Chapter 2

The Effect of Semicollisional Accretion on Planetary Spins[1]

Planetesimal accretion during planet formation is usually treated as collisionless. Such accretion from a uniform and dynamically cold disk predicts protoplanets with slow retrograde rotation. However, if the building blocks of protoplanets, planetesimals, are small, of the order of a meter in size, then they are likely to collide within the protoplanet's sphere of gravitational influence, creating a prograde accretion disk around the protoplanet. The accretion of such a disk results in the formation of protoplanets spinning in the prograde sense with the maximal spin rate allowed before centrifugal forces break them apart. As a result of semi-collisional accretion, the final spin of a planet after giant impacts is not completely random, but is biased toward prograde rotation. The eventual accretion of the remaining planetesimals in the post-giant-impact phase might again be in the semi-collisional regime and delivers a significant amount of additional prograde angular momentum to the terrestrial planets. We suggest that in our solar system, semi-collisional accretion gave rise to the preference for prograde rotation observed in the terrestrial planets and perhaps the largest asteroids.

[1]This chapter was previously published in similar form as Schlichting, H. E., & Sari, R. 2007, ApJ, 658, 593.

2.1 Introduction

Protoplanets form by the accretion of planetesimals. When planetesimals are accreted, they deliver rotational angular momentum due to their relative motion with respect to the protoplanet. This accretion is usually treated as collisionless, assuming that collisions among planetesimals can be neglected while they are within the Hill sphere of the protoplanet. In collisionless accretion, the angular momentum accreted from a uniform and dynamically cold disk of planetesimals results in slow retrograde rotation (Lissauer & Kary, 1991; Dones & Tremaine, 1993a). Lissauer et al. (1997) have shown that rapid prograde rotation can only be achieved if disk density profiles are imposed such that the surface mass density near the outer edges of a protoplanet's feeding zone is significantly greater than that in the rest of the accretion zone. This suggests that protoplanets do not possess any significant spin due to collisionless planetesimal accretion. The final stage of terrestrial planet formation consists of collision and accretion events of a few dozen protoplanets of $\sim 0.05 M_{\oplus}$ (Agnor et al., 1999; Chambers, 2001; Goldreich et al., 2004b). These giant impacts deliver spin angular momentum to the final planet. If giant impacts are solely responsible for the final spin properties of terrestrial planets then, just after the culmination of giant impacts, terrestial planets should display random obliquities (the angle between the orbital and rotational angular momentum) and exercise prograde and retrograde rotation with equal likelihood. However, if the planetesimals are sufficiently small, then their mutual collisions, while inside the Hill sphere of the protoplanet, can no longer be neglected. If the mutual planetesimal collision rate exceeds the rate of direct collisions onto the protoplanet, then the accretion might be dominated by binding planetesimals into an accretion disk rather than direct impacts onto the protoplanet; we call this semi-collisional accretion. Collisional accretion takes over when the optical depth within the disk plane over the Hill radius exceeds unity.

In this chapter, we investigate the possibility of semi-collisional or collisional planetesimal accretion and the effect it would have on planetary spins. In §2.2 we first determine the range of planetesimal sizes for which semi-collisional or collisional ac-

cretion applies and derive the consequences of semi-collisional and collisional accretion for the spin of protoplanets. The spin of terrestrial planets due to giant impacts of protoplanets is calculated in §2.3 and compared with the semi-collisional contribution. Post-giant-impact accretion is discussed in §2.4. Comparison with the solar system and conclusions follow in §2.5.

2.2 Semi-Collisional and Collisional Accretion

The Hill radius is the distance from the protoplanet at which the tidal force due to the Sun and the gravitational force due to the protoplanet both acting on a planetesimal are in equilibrium. It is given by

$$R_H \equiv a \left(\frac{m}{3M_\odot} \right)^{1/3} \tag{2.1}$$

where a is the semi-major axis of the protoplanet and m its mass. When two planetesimals collide with one another while passing through the Hill sphere of the protoplanet, one or both of them become bound to the protoplanet. Further collisions among the bound particles damp their random motions, leading to the formation of an accretion disk around the protoplanet (Sari & Goldreich, 2006) (see Fig. 2.1). Inelastic planetesimal collisions and subsequent capture by the planet's gravitational field has been proposed in order to explain the formation of circumplanetary disks from which regular satellites could form (e.g., Safronov et al., 1986; Estrada & Mosqueira, 2006). Here we explore the possibility that the growth of protoplanets is dominated by the accretion of such a planetesimal disk. The details of this accretion process, such as what fraction of bound particles will be accreted by the growing protoplanet, are uncertain. Perturbations from nearby protoplanets and moons or gas, if still present at the time protoplanets form, may facilitate the dissipation of the planetesimals' angular momenta, allowing efficient accretion onto the protoplanet.

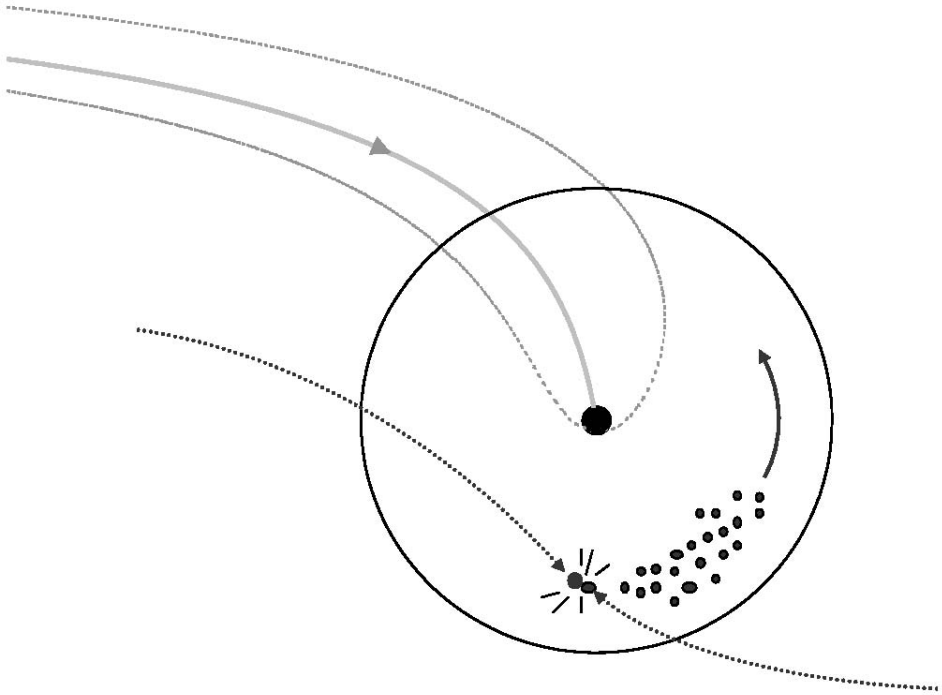

Figure 2.1 Collisionless and semi-collisional accretion. The protoplanet is represented by the filled black circle and its Hill radius is given by the solid black line. In the case of collisionless accretion (light grey lines), only planetesimals with impact parameters that allow direct collision with the protoplanet are accreted. In the semi-collisional and collisional regimes (dark grey lines), unbound planetesimals collide inside the Hill sphere of the protoplanet, producing bound planetesimals that form a prograde accretion disk around the protoplanet. This enables the protoplanet to effectively accrete at its Hill radius.

2.2.1 Planetesimal Sizes

For dynamically cold planetesimal disks, the ratio between the rate of planetesimal collisions within the Hill sphere and the rate of direct collisions onto the protoplanet is $\tau_g \alpha^{-1/2}$, where τ_g is the optical depth within the disk plane over a distance of R_H and $\alpha \equiv r/R_H$, where r is the protoplanet's radius. If $\tau_g \alpha^{-1/2} > 1$, the accretion may be dominated by binding planetesimals into an accretion disk rather than direct impacts onto the protoplanet; we call this semi-collisional accretion. Collisional accretion takes over for $\tau_g > 1$. For inelastic planetesimals with velocity $u < v_H \equiv \Omega R_H$, the optical depth in the disk is given by $\tau_g \sim 3\sigma v_H / s\rho_s u$, where Ω, s, ρ_s, and σ are the protoplanet's Keplerian angular velocity around the Sun, the typical planetesimal radius, material density, and overall mass surface density, respectively. The random velocities of the planetesimals are damped by mutual collisions and stirred by gravitational interactions with the protoplanets. When these two processes are in equilibrium, we have

$$\frac{u}{v_H} \sim \alpha^{-2} \frac{\Sigma}{\sigma} \frac{s}{r}, \qquad \text{for } u < v_H \tag{2.2}$$

where Σ is the mass surface density of the protoplanets (Goldreich et al., 2004b). Most of the planetesimal accretion occurs when $\Sigma/\sigma \sim 1$. The condition for semi-collisional accretion ($\tau_g \alpha^{-1/2} > 1$) together with equation (2.2) defines an upper limit to the planetesimal size for which semi-collisional accretion holds. Using the minimum mass solar nebula (Hayashi, 1981) surface density of ~ 8 g/cm^2 at 1 AU, $\rho_s \sim 3$ g/cm^3 and an isolation mass $\sim 0.05\ M_\oplus$ (Weidenschilling et al., 1997), we find [1] that $s \lesssim 9$ m. A lower limit to the planetesimal size is given by the velocity dispersion for which the disk becomes locally unstable to gravitational collapse. This velocity is ~ 10 cm/s at 1 AU, corresponding to a minimum size for planetesimals of ~ 6 cm. Therefore semi-collisional or collisional accretion applies as long as 6 cm $\lesssim s \lesssim 9$ m. A fragmentation cascade produced by destructive planetesimal collisions leads to the formation of ever

[1] All estimates above assume $u < \alpha^{1/2} v_H$. However, for large enough planetesimals we have $\alpha^{1/2} v_H < u < v_H$. Taking this into account results in a slightly higher upper limit of 17 m for s. For simplicity and given the order-of-magnitude nature of this calculation, we ignore this complication.

smaller planetesimals (Goldreich et al., 2004b). In fact, gravitational instabilities in the disk may be responsible for the lower limit on the planetesimal size, in which case $s \sim 6$ cm. Possible gaseous remnants of the solar nebula may lower the velocity dispersion, preventing fragmentation down to the stability limit. Although this is an uncertainty during protoplanet formation, it is unlikely that significant amounts of gas prevailed after giant impacts. Furthermore, the low bulk density (~ 0.6 g/cm^3) of comets (Astakhov et al., 2005; Davidsson & Gutiérrez, 2006) seems to suggest gentle accretion of small bodies and therefore supports the idea of semi-collisional or collisional accretion.

2.2.2 Spin of Protoplanets Due to Planetesimal Accretion

We assume that the orbits of the planetesimals and the protoplanets are circular and co-planar. The interaction between the planetesimals and the protoplanet can be described by Hill's equations (Hill, 1878; Goldreich & Tremaine, 1980; Petit & Henon, 1986). In our coordinates, the position of the planetesimal is given with respect to the protoplanet. The x-axis points radially outwards and the y-axis in the prograde direction. The equations of motion are given by

$$\ddot{x} - 2\Omega\dot{y} - 3\Omega^2 x = -\frac{Gm}{(x^2+y^2)^{3/2}}x \tag{2.3}$$

$$\ddot{y} + 2\Omega\dot{x} = -\frac{Gm}{(x^2+y^2)^{3/2}}y. \tag{2.4}$$

We solve these equations numerically and sum the specific angular momenta of all planetesimals that pass within some effective accretion radius R_{acc}. In collisionless accretion the protoplanet accretes at its actual radius, so that $R_{acc} = r$; in semi-collisional or collisional accretion, an accretion disk forms and the protoplanet effectively accretes at its gravitational radius such that $R_{acc} \sim R_H$. Figure 2.2 shows that protoplanets acquire a retrograde spin for $R_{acc} < 0.2R_H$ and a prograde rotation for $R_{acc} > 0.2R_H$. The prograde rotation for $R_{acc} \gg R_H$ can be understood by considering the angular momentum supplied by planetesimals due solely to the Keplerian

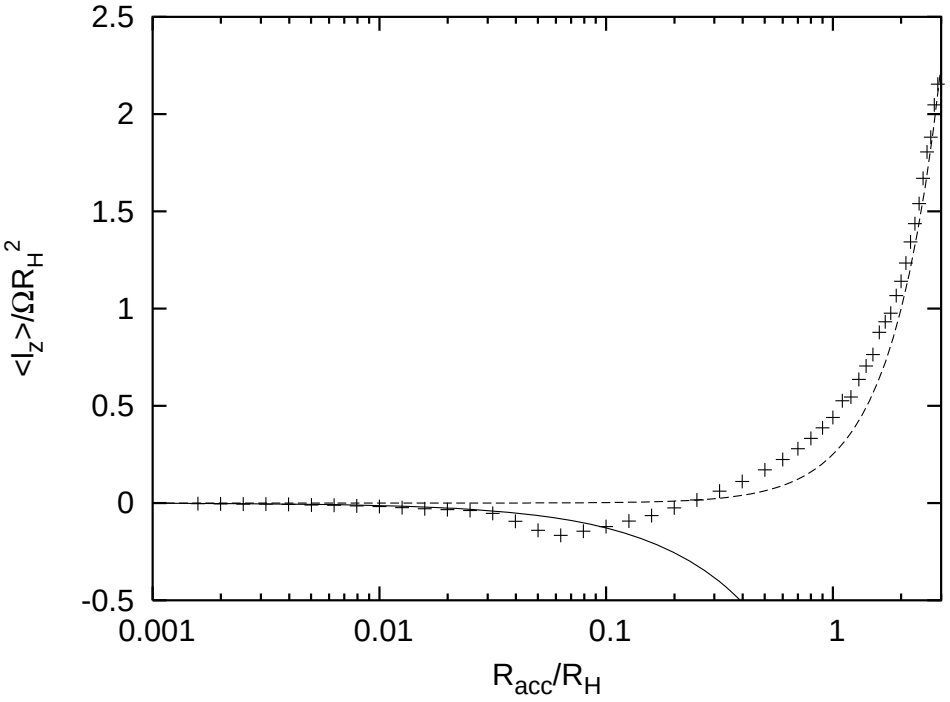

Figure 2.2 Mean specific angular momentum $< l_z >$ in units of ΩR_H^2, of planetesimals from a cold disk that come within accretion radius R_{acc} in units of R_H. The crosses indicate the results from our numerical integration and the dashed line corresponds to the limit in which the gravity of the protoplanet can be neglected, i.e., $R_{acc} >> R_H$. The solid line shows the analytic solution valid for $R_{acc} << R_H$ (Dones & Tremaine, 1993a).

shear of the disk. In this case the specific angular momentum carried into R_{acc} is $R_{acc}^2\Omega/4$ in the prograde sense (Lissauer & Kary, 1991; Dones & Tremaine, 1993a). The actual angular momentum delivered to the planet is given by Figure 2.2 for collisionless accretion only. In the semi-collisional and collisional cases, the disk must lose angular momentum before it can be accreted by the protoplanet. The accretion of such a disk results in the formation of protoplanets spinning in the prograde sense with the maximal spin rate allowed before centrifugal forces break them apart. One should note that Figure 2.2 is only physically meaningful for $R_{acc} < R_H$ since fragments produced by planetesimal collisions outside R_H will not be gravitationally bound to the protoplanet.

2.3 Giant Impacts

The final stage of terrestrial planet formation consists of collision and accretion events among the protoplanets. These giant impacts deliver spin angular momentum to the final planet. Provided that the random velocities of the protoplanets are sufficiently large, one can neglect the shear imposed by the differential rotation of the disk, so there is no preferred direction for giant impacts to occur. Giant impacts therefore deliver angular momentum in a random-walk-like fashion. Lissauer & Safronov (1991) and Dones & Tremaine (1993b) calculated the magnitude of the random component of the spin angular momentum due to a single giant impact and compared it with the observations. Here we determine the random and systematic spin angular momentum delivered to the final planet by N giant impacts using the following toy model. We start with $N+1$ identical protoplanets all of mass m and radius r that are sequentially accreted one by one. After N such accretion events, we are left with a final planet of mass $M = (N+1)m$ and radius $R = (N+1)^{1/3}r$. We assume throughout that protoplanets are spherical with constant density ρ.

2.3.1 Random Component of the Angular Momentum

Assuming that the protoplanets' velocity dispersion is small compared to their impact velocity and that protoplanets have no spin, the maximum angular momentum delivered by one impact is

$$l_{max} = \frac{M_T m}{M_T + m}\sqrt{2G\left(M_T + m\right)\left(R_T + r\right)} \tag{2.5}$$

where M_T is the mass and R_T the radius of the target. The root mean square (rms) angular momentum in the direction perpendicular to the plane of the solar system (z-direction) contributed by a single impact can be obtained by averaging over all possible impact parameters and is given by $l^z_{rms} = \sqrt{1/6}l_{max}$. Adding the contributions of each impact in quadrature, with $M_T = nm$ and $R_T = n^{1/3}r$ for $n = 1, 2, ..., N$, the final rms angular momentum in the z-direction after $N \gg 1$

impacts is

$$L^z_{rms} = \sqrt{\frac{1}{7}} N^{-1/2} \omega_{crit} M R^2 \tag{2.6}$$

where

$$\omega_{crit} = \sqrt{\frac{4\pi G\rho}{3}}. \tag{2.7}$$

The precise number of giant impacts during the late stage of planet formation is uncertain. However, the final "isolation" mass for the minimum mass solar nebula at 1AU is about $0.05 M_\oplus$ (Weidenschilling et al., 1997; Goldreich et al., 2004a). This suggests that about 20 giant impacts would have to occur in order to form an Earth at 1AU. For $N \sim 20$, equation (2.6) predicts a spin period of $\sim$ 4hr for the Earth. N-body simulations find a somewhat shorter spin period of $\sim$ 1.8hr for bodies more massive than $0.5 M_\oplus$ (Agnor et al., 1999). This rapid rotation originates from unphysical mergers between protoplanets encountering each other at more than the escape velocity. As expected, N-body simulations also show that final obliquities due to giant impacts with no initial spin are randomly distributed (Agnor et al., 1999; Chambers, 2001).

2.3.2 Systematic Component of the Angular Momentum

The final spin of a terrestrial planet after giant impacts is no longer random, but contains a systematic component if each protoplanet possesses a systematic spin due to semi-collisional planetesimal accretion. The systematic component of the angular momentum delivered by N impacts of maximally spinning protoplanets with prograde rotation is

$$L_{Spin} = L^z_{Spin} = \frac{2}{5} N^{-2/3} M R^2 \omega_{crit}. \tag{2.8}$$

2.3.3 Comparison

Comparing the random z-component of the angular momentum (eq. [2.6]) to the systematic one (eq. [2.8]), we find that they are similar in magnitude with the random component up to twice the systematic one for $1 \lesssim N \lesssim 60$. The final distribution for

the z-component of the angular momentum is obtained by combining the random and the ordered contributions. It is normally distributed with its mean given by equation (2.8) and its standard deviation given by equation (2.6). Since the mean is positive, corresponding to prograde rotation, we expect more prograde than retrograde spins in a given planetary system. We find about 70% of all planets to be rotating in the prograde sense and only 30% in a retrograde manner for $10 \lesssim N \lesssim 60$ giant impacts.

2.3.4 Uncertainties

The following uncertainties could affect our estimates for prograde and retrograde rotation. We have assumed that the velocity dispersion of the protoplanets is small compared to the impact velocity. However, the velocity dispersion might be as large as the escape velocity from the protoplanet, in which case the random component of the angular momentum could increase up to $\sim \sqrt{2}$. A higher fraction of planets with retrograde rotation would be produced if the mutual accretion of protoplanets were pairwise, such that all giant impacts were between equal-sized bodies, rather than one by one. Furthermore, the majority of the mass accreted is likely due to collisions close to head on, which deliver a smaller random component of angular momentum than grazing ones (Agnor & Asphaug, 2004). On the other hand, grazing collisions could deliver spin angular momentum and little mass. Hydrodynamic simulations show, however, that the efficiency of transfer of orbital angular momentum to spin angular momentum tends to be less than 10% for oblique collisions with disruption (Love & Ahrens, 1997).

2.4 Accretion after Giant Impacts

The stirring force that protoplanets exert on each other can be balanced by the force due to dynamical friction caused by the planetesimals as long as $\sigma > \Sigma$, ensuring small random velocities of the protoplanets. However, as the protoplanets accrete more planetesimals, their surface density increases and dynamical friction becomes less and less effective until it is no longer able to balance the mutual stirring of the

protoplanets. Orbit crossing and giant impacts set in when $\sigma \sim \Sigma$ (Goldreich et al., 2004a). Planetesimal accretion continues, and additional "new" planetesimals are produced as by-products of giant impacts. The exact amount of smaller particles produced in a giant impact depends on the mass ratio of the two colliding protoplanets, their relative velocity, and impact angle. For example, for collisions between like-sized protoplanets with an impact velocity of twice their escape velocity and an impact angle of 30° (where 0° corresponds to a head-on collision), about 10% of the total mass of the system escapes as smaller particles (Agnor & Asphaug, 2004). Due to the production of "new" planetesimals in giant impacts and the fact that giant impacts set in when $\sigma \sim \Sigma$, large amounts of planetesimals are expected to still be present after the culmination of giant impacts. This is also required to relax the high eccentricities of planets expected after giant impacts (Goldreich et al., 2004a). N-body simulations predict eccentricities of ~ 0.1 for terrestrial planets after giant impacts (Chambers, 2001). The eccentricity damping timescale t_{damp} due to dynamical friction caused by leftover planetesimals is given by

$$t_{damp} = -v\frac{dt}{dv} \sim \frac{\rho R}{\sigma \Omega}\left(\frac{v}{v_{esc}}\right)^4. \tag{2.9}$$

This timescale should be shorter than the time required for the remaining planetesimals to be accreted onto the terrestrial planets:

$$t_{acc} = -\sigma\frac{dt}{d\sigma} \sim \frac{\rho R}{\Sigma \Omega}\left(\frac{v}{v_{esc}}\right)^2. \tag{2.10}$$

This yields

$$\sigma \gtrsim \Sigma\left(\frac{v}{v_{esc}}\right)^2 \sim 0.07\Sigma. \tag{2.11}$$

Therefore, more than 7% of the mass should still reside in planetesimals in order to damp the planets' eccentricities. The eventual accretion of the remaining planetesimals delivers additional angular momentum to the planet. For sufficiently small planetesimals, this accretion would again be in the semi-collisional or collisional regime and hence deliver additional prograde angular momentum to the planet. The ac-

cretion of about 10% $M_\oplus$ in a semi-collisional manner would be sufficient to deliver an angular momentum equivalent to that of the Earth-Moon system. For Mars less than 3% of its mass would need to be accreted semi-collisionally to supply its current angular momentum, assuming that it had no previous spin. These small percentages indicate that semi-collisional or collisional accretion of only a small fraction of the planet's mass after giant impacts is sufficient to substantially alter planetary spins leading again to favoritism of prograde rotation. Formation of gaps in the planetesimal disk after giant impacts may complicate this picture.

2.5 Conclusions

We have shown here, that planetesimal accretion might be in the semi-collisional or collisional regime, leading to the formation of a prograde accretion disk around the protoplanet. Such a disk gives rise to a maximally spinning protoplanet with prograde rotation. The final spin of terrestrial planets is therefore no longer random, but is biased toward prograde rotation. The dominance of prograde rotation might be increased further by the accretion of leftover planetesimals in the post-giant-impact phase, provided that semi-collisional or collisional accretion still applies. Comparing our results with the spin properties of the terrestrial planets is somewhat difficult since the spins of Mercury and Venus have evolved considerably since their formation (Laskar & Robutel, 1993; McCue & Dormand, 1993), leaving only Earth and Mars as planets whose spins have evolved to a much lesser degree. Earth and Mars both display prograde rotation with small obliquities, which is consistent with semi-collisional or collisional accretion. However, no firm conclusions can be drawn from such a small data set, and we cannot rule out the possibility that the low obliquities of Earth and Mars are coincidental.

Terrestrial planet formation in the asteroid belt was interrupted when growing planets became massive enough to gravitationally perturb the local population, causing bodies to collide with increased energy, ending accretion and commencing fragmentation. Evidence from Vesta's crust (e.g., Chapman, 1986) and recent models of

collisional evolution in the asteroid belt (Gil-Hutton, 1997; Bottke et al., 2005) suggests that the largest asteroids have survived un-shattered and that they experienced very little collisional evolution. Their current spin properties may therefore still contain some information about their primordial spin state and hence clues about the formation of protoplanets (Davis et al., 1989; Bottke et al., 2005). The two most massive asteroids, Ceres and Vesta, both exercise prograde rotation with periods of 9.1 and 5.3 hr, respectively. Ceres's spin axis has a 12° inclination with respect to the normal of the ecliptic (Thomas et al., 2005), and Vesta's spin axis inclination to the normal of the ecliptic is $\sim 40°$ (Drummond et al., 1998). The spin properties of Ceres and Vesta might therefore be indicative of semi-collisional or collisional accretion in the asteroid belt. Even smaller main-belt asteroids (diameter $\sim$ 100km) that are thought to have undergone more severe collisional evolution display a preference for prograde rotation (Pravec et al., 2002; Magnusson et al., 1989)

Kuiper Belt objects (KBOs) grew mainly by planetesimal accretion. The formation time for Pluto-sized KBOs is comparable to the time required for a collisional cascade to set in, grinding initially kilometer-sized planetesimals to meters in size. If indeed a collisional cascade started by the time the largest KBOs formed, semi-collisional accretion could have dominated their formation. This may explain the intriguingly rapid spin of $2003EL_{61}$, whose rotation period is only $\sim$ 4hr (Rabinowitz et al., 2006). However, the retrograde rotations of Pluto and $2003EL_{61}$ (Brown et al., 2005) (assuming that it spins in the same direction as it is orbited by its largest satellite) conflict with this and tentatively suggest that semi-collisional accretion did not dominate their formation.

Chapter 3

Formation of Kuiper Belt Binaries[1]

The discovery that a substantial fraction of Kuiper Belt objects (KBOs) exists in binaries with wide separations and roughly equal masses, has motivated a variety of new theories explaining their formation. Goldreich and colleagues proposed two formation scenarios: In the first, a transient binary is formed, which becomes bound with the aid of dynamical friction from the sea of small bodies (L^2s mechanism); in the second, a binary is formed by three-body gravitational deflection (L^3 mechanism). Here, we accurately calculate the L^2s and L^3 formation rates for sub-Hill velocities. While the L^2s formation rate is close to previous order of magnitude estimates, the L^3 formation rate is about a factor of 4 smaller. For sub-Hill KBO velocities ($v \ll v_H$) the ratio of the L^3 to the L^2s formation rate is $0.05(v/v_H)$, independent of the small bodies' velocity dispersion, their surface density, or their mutual collisions. For super-Hill velocities ($v \gg v_H$) the L^3 mechanism dominates over the L^2s mechanism. Binary formation via the L^3 mechanism competes with binary destruction by passing bodies. Given sufficient time, a statistical equilibrium abundance of binaries forms. We show that the frequency of long-lived transient binaries drops exponentially with the system's lifetime and that such transient binaries are not important for binary formation via the L^3 mechanism, contrary to Lee and colleagues. For the L^2s mechanism we find that the typical time that transient binaries must last to form Kuiper Belt binaries

[1]This chapter was previously published in similar form as Schlichting, H. E., & Sari, R. 2008, ApJ, 673, 1218.

(KBBs) for a given strength of dynamical friction, D, increases only logarithmically with D. Longevity of transient binaries (with lifetimes $\geqslant 15\Omega^{-1}$ as suggested by Astakhov and colleagues) only becomes important for very weak dynamical friction (i.e., $D \lesssim 0.002$) and is most likely not crucial for KBB formation.

3.1 Introduction

One of the many intriguing discoveries in the Kuiper Belt is that a substantial fraction of its largest members are binaries; 48 such systems are currently known (for a comprehensive review, see Noll et al. (2008)). Broadly speaking, we can identify two classes of Kuiper Belt binaries (KBBs). The first class consists of small satellites around the largest Kuiper Belt objects (KBOs) and the second of roughly equal mass binaries with wide separations. The existence of the first class of binaries is most likely explained by the standard formation scenario involving a collision and tidal evolution, as has been proposed for the formation of the Moon and the Pluto-Charon system (Hartmann & Davis, 1975; Cameron & Ward, 1976; McKinnon, 1989). This formation scenario fails however for the second class of KBBs, since it cannot account for their wide separations. This has motivated a variety of new theories for the formation of comparable-mass KBBs (e.g., Weidenschilling, 2002; Goldreich et al., 2002; Funato et al., 2004; Astakhov et al., 2005; Lee et al., 2007). Weidenschilling (2002) proposed a new formation mechanism for KBBs consisting of a collision between two bodies inside the Hill sphere of a third. However, in the Kuiper Belt, gravitational scattering between the two intruders is about 100 times[1] more common than a collision. Binary formation by three-body gravitational deflection (L^3 mechanism), as proposed by Goldreich et al. (2002), should therefore dominate over such a collisional formation scenario. Goldreich et al. (2002) proposed a second binary formation scenario: it consists of the formation of a transient binary, which becomes bound with the aid of dynamical friction from the sea of small bodies. This is called the L^2s mecha-

[1]For this estimate we used $\alpha \sim 10^{-4}$ and assumed that the velocity dispersion of the KBOs at the time of binary formation is less than their Hill velocity, see §3.2 for details

nism. Astakhov et al. (2005) and Lee et al. (2007) suggest that transient binaries that spend a long time in their mutual Hill sphere, near a periodic orbit, form the binaries in the L^2s and L^3 mechanisms. We address and investigate the relative importance of these long-lived transient binaries for the L^2s and L^3 formation mechanisms and find that they are most likely not significant for the overall binary formation in the Kuiper Belt. Finally, Funato et al. (2004) proposed a binary formation mechanism which involves a collision between two large KBOs which creates a small moon. An exchange reaction replaces the moon with a massive body with high eccentricity and large semi-major axis.

In this chapter, we accurately calculate the L^2s and L^3 formation rates for sub-Hill KBO velocities and discuss how these rates are modified for super-Hill velocities. This allows us to determine for which physical parameters and velocity regime each mechanism dominates the binary formation. Further, we calculate the frequency of long-lived transient binaries and assess their importance for the overall KBB formation.

This chapter is structured as follows. In §3.2 we outline our assumptions, explain our choice of parameters, and define variables that are used throughout this chapter. We calculate the L^3 and L^2s formation rates for sub-Hill KBO velocities in §3.3 and §3.4, respectively. We compare the L^2s and L^3 formation rates in the sub-Hill velocity regime in §3.5. In §3.6 we discuss how these formation rates are modified for super-Hill KBO velocities. The frequency of long-lived transient binaries and their significance for the overall KBB formation is calculated in §3.7. Summary and conclusions follow in §3.8.

3.2 Definitions and Assumptions

The Hill radius denotes the distance from a KBO at which the tidal forces due to the Sun and the gravitational force due to the KBO, both acting on a test particle, are

in equilibrium. It is given by

$$R_H \equiv a \left(\frac{M}{3M_\odot} \right)^{1/3} \tag{3.1}$$

where a is the semi-major axis, M is the mass of the KBO, and $M_\odot$ is the mass of the Sun. We use the "two-group approximation" (Goldreich et al., 2002, 2004b) which consists of the identification of two groups of objects, small ones, which contain most of the total mass with surface mass density σ, and large ones, that contain only a small fraction of the total mass with surface mass density $\Sigma \ll \sigma$. We assume $\sigma \sim 0.3\text{g cm}^{-2}$ which is the extrapolation of the minimum-mass solar nebula to a heliocentric distance of 40AU. Estimates from current Kuiper Belt surveys (Trujillo & Brown, 2003; Trujillo et al., 2001) yield $\Sigma \sim 3 \times 10^{-4}\text{g cm}^{-2}$ for KBOs with radii of $R \sim 100$ km. We use this value of Σ, assuming that Σ during the formation of KBBs was the same as it is now. Our choice for Σ and σ is also consistent with results from numerical coagulation simulations by Kenyon & Luu (1999).

Large bodies grow by the accretion of small bodies. Large KBOs viscously stir the small bodies, increasing the small bodies' velocity dispersion u. As a result, u grows on the same timescale as R provided that mutual collisions among the small bodies are not yet important. In this case, u is given by

$$\frac{u}{v_H} \sim \left(\frac{\Sigma}{\sigma\alpha} \right)^{1/2} \sim 3 \tag{3.2}$$

where $\alpha = R/R_H \sim 10^{-4}$ at 40AU (Goldreich et al., 2002), and v_H is the Hill velocity of the large bodies which is given by $v_H = \Omega R_H$, where Ω is the orbital frequency around the Sun. The velocity v of large KBOs increases due to mutual viscous stirring, but is damped by dynamical friction from the sea of small bodies such that $v < u$. Balancing the stirring and damping rates of v and substituting for u from equation (3.2), we find

$$\frac{v}{v_H} \sim \alpha^{-2} \left(\frac{\Sigma}{\sigma} \right)^3 \sim 0.1. \tag{3.3}$$

For our choice of parameters, we have that $v < v_H$ during the epoch of formation of

bodies with $R \sim 100$km. In addition, we argue that v could not have exceeded v_H significantly during satellite formation in the Kuiper Belt. If $v_{esc} > v > v_H$, where v_{esc} is the escape velocity from the large bodies, then the timescale for mutual collisions is

$$\tau_{coll} \sim 0.13 \left(\frac{\Sigma}{3 \times 10^{-4}\text{g cm}^{-2}}\right)^{-1} \left(\frac{\rho}{1\text{g cm}^{-3}}\right) \left(\frac{R}{100\text{km}}\right) \left(\frac{\alpha}{1 \times 10^{-4}}\right) \times \left(\frac{v}{v_H}\right)^2 \left(\frac{\Omega}{7.9 \times 10^{-10}\text{s}^{-1}}\right)^{-1} \text{Gyr}. \quad (3.4)$$

Equation (3.4) shows that the collision timescale among the largest KBOs ($R >$ 100km) would have been excessively long if $v \gg v_H$ during satellite formation. The ubiquity of small satellites around KBOs, which have radii as large as $\sim$ 1000km, (Brown et al., 2006a; Brown & Suer, 2007) and the Pluto-Charon system (Weaver et al., 2006) suggests that $v < v_H$ during their formation, since their origin is best explained by a giant impact (e.g., Stern et al., 2006; Brown et al., 2007). This is supported further by the recent discovery of a collisional family belonging to EL_{61} (Brown et al., 2007). We therefore focus our work on the shear-dominated velocity regime ($v < v_H$). However, we discuss how our results would be modified if $v > v_H$.

3.3 L^3 Formation Rate

A transient binary forms when two large KBOs enter each other's Hill sphere. This transient binary must lose energy in order to become gravitationally bound. In the L^3 mechanism the excess energy is carried away by an encounter with a third massive body. We calculate the binary formation rate via the L^3 mechanism in the shear-dominated velocity regime. Since the growth of inclinations is suppressed in the shear-dominated velocity regime, the disk of KBOs is effectively two-dimensional (Wetherill & Stewart, 1993; Rafikov, 2003; Goldreich et al., 2004b). We therefore restrict this calculation to two dimensions. As initial condition, we assume that all bodies are on circular orbits. We chose to work in the rotating frame with the x-axis pointing radially outwards and the y-axis in the prograde direction. For a

gravitational deflection of three equal-mass bodies, the L^3 formation rate per body is

$$FR_{L^3} = \int_{\gamma=-\infty}^{\infty} \int_{b_2>b_1}^{\infty} \int_{b_1=0}^{\infty} \left(\frac{\Sigma}{\frac{4\pi}{3}\rho R^3} \right)^2 \frac{3}{2} b_1 \Omega F_{L^3}(b_1, b_2, \gamma) db_1 db_2 d\gamma. \tag{3.5}$$

where $\Sigma/(4\pi\rho R^3/3)$ is the surface number density of the KBOs, b_1 and b_2 are the relative initial separations in the x-direction between bodies 1 and 2 and bodies 1 and 3, respectively, and γ is the offset in the y-direction body 3 would have when bodies 1 and 2 would encounter each other had their relative velocity been solely due to the Kepler shear of the disk: $3b_1\Omega/2$. Finally, $F_{L^3}(b_1, b_2, \gamma)$ is a function that takes on the value 1 if the encounter resulted in the formation of a binary between any two of the three KBOs involved and 0 otherwise. The choice of limits on the integrals in equation (3.5) ensures no double counting of the binaries. Expression (3.5) can be written as

$$FR_{L^3} = A_{L^3} \left(\frac{\Sigma}{\rho R} \right)^2 \alpha^{-4} \Omega \tag{3.6}$$

where

$$A_{L^3} = \left(\frac{27}{32\pi^2} \right) \int_{\gamma=-\infty}^{\infty} \int_{b_2>b_1}^{\infty} \int_{b_1=0}^{\infty} F_{L^3}(b_1, b_2, \gamma) \times \left(\frac{b_1}{R_H} \right) \left(\frac{db_1}{R_H} \right) \left(\frac{db_2}{R_H} \right) \left(\frac{d\gamma}{R_H} \right). \tag{3.7}$$

Expression (3.6) agrees with the order of magnitude estimate of Goldreich et al. (2002) if we set $A_{L^3} = 1$. It is the value of the constant A_{L^3} we determine here. Since we are interested in close encounters among the KBOs, their interaction is well described by Hill's equations (Hill, 1878; Goldreich & Tremaine, 1980; Petit & Henon, 1986) that we modify to include three equal-mass bodies besides the Sun. The equations of motion, with length scaled by R_H and time by Ω^{-1}, for body 1 are given by

$$\ddot{x}_1 - 2\dot{y}_1 - 3x_1 = -\frac{3(x_1 - x_2)}{[(x_1 - x_2)^2 + (y_1 - y_2)^2]^{3/2}} - \frac{3(x_1 - x_3)}{[(x_1 - x_3)^2 + (y_1 - y_3)^2]^{3/2}} \tag{3.8}$$

$$\ddot{y}_1 + 2\dot{x}_1 = -\frac{3(y_1 - y_2)}{[(x_1 - x_2)^2 + (y_1 - y_2)^2]^{3/2}} - \frac{3(y_1 - y_3)}{[(x_1 - x_3)^2 + (y_1 - y_3)^2]^{3/2}}. \tag{3.9}$$

The subscripts 1, 2, and 3 label the x- and y-coordinates of KBO 1, 2, and 3 respectively. Similar equations of motion can be obtained for bodies 2 and 3. The function $F_{L^3}(b_1, b_2, \gamma)$ is calculated by numerically integrating the equations of motion. A binary formation event is detected in the following way. The equations of motion of the three bodies are integrated until a time that corresponds to a separation of at least $30R_H$ between all three bodies (after their conjunction), assuming that their relative velocity is solely due to their Keplerian sheer (i.e., ignoring the actual gravitational interaction between the bodies), plus an additional time of $120\Omega^{-1}$. If after this time the separation between two bodies is still less than $3R_H$, a binary is considered to have formed. We chose a separation of $3R_H$ instead of R_H to allow for binary orbits that reach slightly outside R_H. Numerical integrations are terminated early if the separation between KBOs becomes less than $10^{-4}R_H$ and these events are not counted towards the binaries formed. This serves two purposes. First of all, $10^{-4}R_H$ roughly corresponds to the separation at which physical collisions occur in the Kuiper Belt. Second, by introducing a minimum separation, we prevent divergence in the equations of motion. This cut-off limits, strictly speaking, the validity of the value of A_L^3 calculated here to binary formation at heliocentric distances of ~ 40AU since the separation in units of R_H, corresponding to collisions among the KBOs, is inversely proportional to the heliocentric distance. In order to determine A_{L^3} we need to cover the three-dimensional parameter space spanned by b_1, b_2, and γ. We chose a spacing of $0.1R_H$ for all three parameters; $12.5R_H$ is chosen as the upper limit for b_1 and b_2, and the upper limit for $|\gamma|$ is $25R_H$. The given limits and resolution require numerical integrations of $\sim 4 \times 10^6$ orbits. We obtain

$$A_{L^3} = 0.28 \pm 0.01 \tag{3.10}$$

where 0.01 is the estimated Poisson error. We repeated the calculation for A_{L^3} with randomly chosen grid points for b_1, b_2, and γ and the same number of numerical integrations and confirmed that the value of A_{L^3} is insensitive to the grid points chosen. The value of A_{L^3} tends to 0.35 in the limit that the bodies are treated as

point masses (i.e., the limit that the cut-off tends to zero). We use $A_{L^3} = 0.28$, since it corresponds to the physically relevant situation in the Kuiper Belt. This yields a binary formation rate of

$$FR_{L^3} = (6.3 \pm 0.2) \times 10^{-8} \left(\frac{\Sigma}{3 \times 10^{-4} \text{g cm}^{-2}} \right)^2 \left(\frac{\rho}{1 \text{g cm}^{-3}} \right)^{-2} \times \left(\frac{R}{100 \text{km}} \right)^{-2} \left(\frac{\alpha}{1 \times 10^{-4}} \right)^{-4} \left(\frac{\Omega}{7.9 \times 10^{-10} \text{s}^{-1}} \right) \text{yr}^{-1}, \quad (3.11)$$

which is smaller by $1/A_{L^3} \sim 4$ than the order of magnitude estimate of Goldreich et al. (2002).

3.4 L^2s Formation Rate

So far, we have only considered binary formation due to an encounter with a third body that carries away the excess energy. However, binary formation might also occur due to dynamical friction generated by the sea of small bodies (L^2s mechanism). The random velocity of large KBOs is damped due to gravitational interactions with many small bodies. Since it is not feasible to examine the interactions with each small body individually, their net effect is modeled by an averaged force which acts to damp the large KBOs' non-circular velocity. We parameterize the strength of the damping by a dimensionless quantity D defined as the fractional decrease in non-circular velocity due to dynamical friction over a time Ω^{-1},

$$D \sim \frac{\sigma}{\rho R} \left(\frac{u}{v_H} \right)^{-4} \alpha^{-2} \sim \frac{\Sigma}{\rho R} \alpha^{-2} \left(\frac{v}{v_H} \right)^{-1}. \quad (3.12)$$

The first expression is simply an estimate of dynamical friction by the sea of small bodies assuming $u > v_H$. The second expression describes the mutual excitation among the large KBOs for $v < v_H$. These two expressions can be equated, since the stirring among the large KBOs is balanced by the damping due to dynamical friction. In fact, if v is defined as the product of the median eccentricity and the orbital velocity, we can calculate the exact relationship between D and (v/v_H), since the velocity

distribution in the shear-dominated velocity regime has been fully determined (see Collins & Sari (2006); Collins et al. (2007)). Defining v as the product of the median eccentricity and the orbital velocity, we obtain

$$D = 4.1\frac{\Sigma}{\rho R}\alpha^{-2}\left(\frac{v}{v_H}\right)^{-1}. \tag{3.13}$$

For $\rho \sim 1\text{g cm}^{-3}$ and our estimates for (v/v_H), Σ and R from §3.2, we find $D \sim 0.12$. We calculate the binary formation rate for equal-mass bodies via the L^2s mechanism in the shear-dominated velocity regime. As in §3.3, we restrict this calculation to two dimensions with circular motion as an initial condition for the large KBOs and use the same coordinate system as in §3.3. The binary formation rate per body via the L^2s mechanism can be written as

$$FR_{L^2s} = \int_{b=0}^{\infty}\left(\frac{\Sigma}{\frac{4\pi}{3}\rho R^3}\right)\frac{3}{2}b\Omega F_{L^2s}(D,b)db \tag{3.14}$$

where $\Sigma/(4\pi\rho R^3/3)$ is the surface number density of the KBOs, b is the relative initial separation in the x-direction between the two KBOs, and $F_{L^2s}(D,b)$ is a function that takes on the value 1 if the encounter resulted in the formation of a binary for a given D and b and 0 otherwise. Equation (3.14) can be written as

$$FR_{L^2s} = A_{L^2s}D\left(\frac{\Sigma}{\rho R}\right)\alpha^{-2}\Omega \tag{3.15}$$

where

$$A_{L^2s} = D^{-1}\left(\frac{9}{8\pi}\right)\int_{b=0}^{\infty}F_{L^2s}(D,b)\left(\frac{b}{R_H}\right)\left(\frac{db}{R_H}\right). \tag{3.16}$$

Goldreich et al. (2002) showed, using numerical integrations, that FR_{L^2s} is indeed proportional to D. Here we want to determine the actual value of A_{L^2s}. In Hill coordinates the equations of motion of the two KBOs can be decomposed into their center of mass motion and their relative motion with respect to one another. The relative motion of two equal-mass KBOs, including the dynamical friction term, is

governed by

$$\ddot{x} - 2\dot{y} - 3x = -\frac{6x}{(x^2+y^2)^{3/2}} - D\dot{x} \tag{3.17}$$

$$\ddot{y} + 2\dot{x} = -\frac{6y}{(x^2+y^2)^{3/2}} - D(\dot{y} + 1.5x). \tag{3.18}$$

where x and y correspond to the relative separation between the two KBOs in the x- and y-direction respectively. Again, length has been scaled by R_H and time by Ω^{-1}. Equations (3.17) and (3.18) are integrated for different values of D and impact parameters ranging from $2.2R_H$ to $3.2R_H$. Impact parameters outside this range result in a distance of closest approach between the two KBOs of more than R_H. Figure 3.1 shows that the rate of binary formation is proportional to D. The value of A_{L^2s}, estimated from the line of best fit, is 1.4. This yields a binary formation rate of

$$\begin{aligned} FR_{L^2s} = 1.3 \times 10^{-5} &\left(\frac{D}{0.12}\right)\left(\frac{\Sigma}{3\times10^{-4}\text{g cm}^{-2}}\right)\left(\frac{\rho}{1\text{g cm}^{-3}}\right)^{-1} \\ &\times \left(\frac{R}{100\text{km}}\right)^{-1}\left(\frac{\alpha}{1\times10^{-4}}\right)^{-2}\left(\frac{\Omega}{7.9\times10^{-10}\text{s}^{-1}}\right)\text{yr}^{-1}. \end{aligned} \tag{3.19}$$

Using equation (3.12) we can retrieve the scalings of Goldreich et al. (2002). Although, we know the exact L^2s formation rate for a given D and have an exact expression for D in terms of v (see equation [3.13]), the relation between v and the actual physical parameters, i.e., the numerical coefficient in equation (3.3), which is needed for a precise value of D, is uncertain to a factor of order unity.

Contrary to claims by Astakhov et al. (2005) and Lee et al. (2007), the L^2s mechanism does predict a mass-ratio selection. This can be seen from the first part of equation (3.12). For a given u, we have that $D \propto R^3$, since $v_H\alpha^{-1/2} \sim v_{esc} \propto R$. Large KBOs experience stronger dynamical friction (larger D) than smaller ones. This is not at all surprising and is a general feature of dynamical friction (Chandrasekhar, 1943; Binney & Tremaine, 1987). We can write $D = D_0M$, where $D_0 \sim \sigma G^2/u^4$; D_0 is a constant independent of the KBO mass for a given σ and u. For two KBOs with masses M_1 and M_2, the position of body 1 essentially coincides with the center of mass of the two bodies provided that $M_1/M_2 \gg 1$. In the limit that the KBOs'

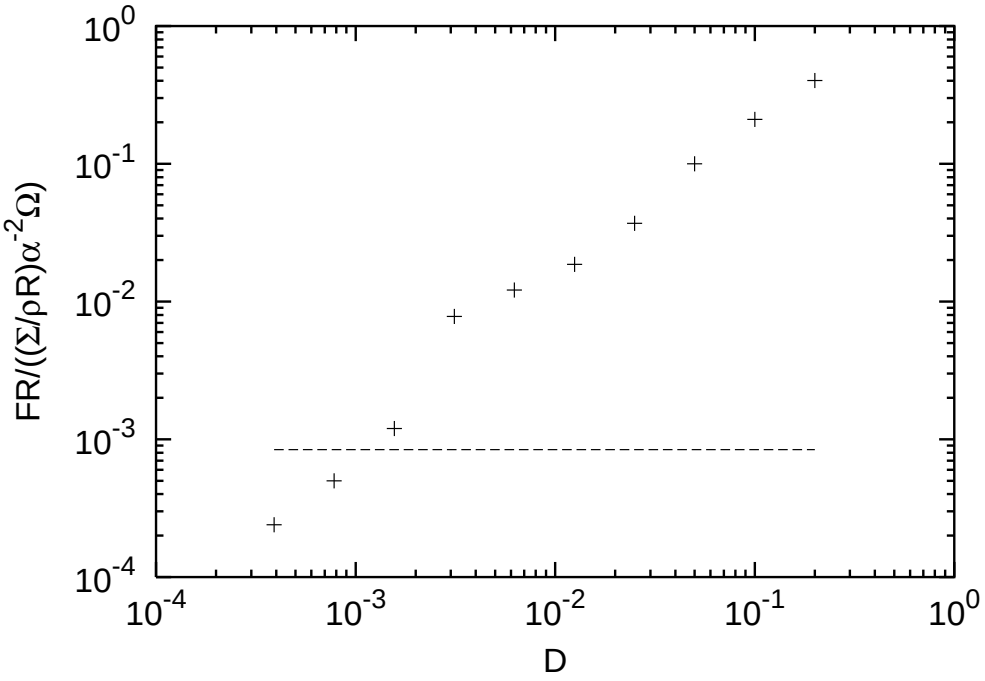

Figure 3.1 Binary formation rate as a function of dynamical friction strength D. The crosses correspond to the formation rate via the L^2s mechanism, and the dashed horizontal line corresponds to the L^3 formation rate for $(\Sigma/\rho R)\alpha^{-2} = 3 \times 10^{-3}$. The L^2s formation rate is proportional to D. In §3.4 we estimate that $D \sim 0.12$, as a result of which $FR_{L^3}/FR_{L^2s} \sim 0.005$.

random velocity tends to zero and that $D_0 M_2 \ll 1$, we can place body 1 at the origin of the Hill coordinate system and treat the center of mass as stationary throughout the interaction. In this limit we find that the relative motion of the two KBOs is governed by

$$\ddot{x} - 2\dot{y} - 3x = -\frac{3x}{(x^2+y^2)^{3/2}} - 2D_0 M_2 \dot{x} \tag{3.20}$$

$$\ddot{y} + 2\dot{x} = -\frac{3y}{(x^2+y^2)^{3/2}} - 2D_0 M_2 (\dot{y} + 1.5x) \tag{3.21}$$

where length is scaled by R_H of KBO 1 and time is scaled by Ω^{-1}. For extreme mass-ratio binaries the relevant strength of the dynamical friction that enters equations (3.20) and (3.21) is twice that acting on the small body (i.e., $2D_0 M_2$) and significantly less than that acting on the large body (i.e., $D_0 M_1$). The $L^2 s$ mechanism therfore favors the formation of comparable-mass binaries from the largest available bodies over high-mass-ratio ones. It is an open question whether this preference for comparable-mass binaries remains after the Kuiper Belt mass spectrum during their formation and their survival probability are accounted for.

3.5 Comparison of $L^2 s$ and L^3 Formation Rates

We are now able to compare the binary formation rates for the $L^2 s$ and L^3 mechanism for sub-Hill velocities. The ratio of the L^3 to $L^2 s$ formation rates is

$$\frac{FR_{L^3}}{FR_{L^2 s}} = 0.20 D^{-1} \frac{\Sigma}{\rho R} \alpha^{-2} = 0.05 \frac{v}{v_H} \tag{3.22}$$

where we substituted for D using the exact relationship from equation (3.13). It is remarkable that this expression depends explicity only on v/v_H and is independent of what sets D. It is therefore independent of the velocity dispersion of the small bodies, their surface density, and the importance of collisions among the small bodies. We therefore conclude that for $v \ll v_H$, binaries in the Kuiper Belt formed primarily due to dynamical friction rather than three-body encounters. Figure 3.1 shows the $L^2 s$ and L^3 formation rates as a function of D. For our estimate of $(v/v_H) \sim 0.1$, we have

that $FR_{L^3}/FR_{L^2s} \sim 0.005$.

3.6 Super-Hill Velocity: $v > v_H$

Obviously, there is some uncertainty in what the actual values of σ and Σ were during binary formation. For a few times larger value of Σ with σ unchanged, we enter the regime in which $v > v_H$ (this can be seen from equation [3.2]). Although it is rather unlikely that $v \gg v_H$ during binary formation (see §3.2), we discuss here briefly how this would affect the L^2s and L^3 formation rates.

For $v > v_H$ the velocity dispersion of the large bodies is still set by the balance between their mutual stirring and the damping due to dynamical friction generated by the sea of small bodies. Therefore, dynamical friction shrinks the orbit of a KBB with a mutual orbital velocity v_B at a rate

$$D\Omega \sim \frac{\Sigma}{\rho R}\alpha^{-2}\Omega\left(\frac{v}{v_H}\right)^{-4} \tag{3.23}$$

where we assume that $v_B < u$. For $v_B \lesssim v$, binaries are broken up by passing KBOs at a rate

$$R_{break} \sim \frac{\Sigma}{\rho R}\alpha^{-2}\Omega\left(\frac{v}{v_H}\right)^{-2}\left(\frac{v_B}{v_H}\right)^{-2}. \tag{3.24}$$

The ratio of these two rates yields

$$\frac{D\Omega}{R_{break}} \sim \left(\frac{v_B}{v}\right)^2. \tag{3.25}$$

Since the ratio in equation (3.25) is < 1 for $v_B < v$, we conclude that KBBs with separations $R_B > R_H(v_H/v)^2$ (i.e. KBBs with $v_B < v$) tend to be broken up by passing KBOs. Binaries with separations of $R_{crit} = R_H(v_H/v)^2$ or less tend to survive. The cross section for the L^3 mechanism is therefore reduced with respect to the sub-Hill case. The probability of having a KBO within R_{crit} of a given KBO is $(\Sigma\Omega)/(\rho R^3 v)\ R_{crit}^3$, where $(\Sigma\Omega)/(\rho R^3 v)$ is the volume number density of KBOs. The flux of KBOs into area R_{crit}^2 is $(\Sigma\Omega)/(\rho R^3 v)\ vR_{crit}^2$. The super-Hill formation rate for

tight binaries with separations $\sim R_{crit}$, via the L^3 mechanism, is therefore

$$FR_{L^3} \sim \left(\frac{\Sigma\Omega}{\rho R^3 v}\right)^2 v R_{crit}^5 \sim \left(\frac{\Sigma}{\rho R}\right)^2 \alpha^{-4} \left(\frac{v_H}{v}\right)^{11} \Omega \tag{3.26}$$

(see also Noll et al. (2008)). In addition to tight binaries with separations of R_{crit} and less, there exists a second class of binaries with larger separations. Binaries with separations $R_B > R_{crit}$ are constantly created and destroyed via the L^3 mechanism. KBBs can form from two KBOs that approach each other with relative velocity $v_B \lesssim v$ while a third KBO removes energy, through gravitational scattering, enabling the KBOs to become bound. Since we are selecting bodies with relative velocities $\sim v_B$ or less, the number of KBOs that can form binaries with separation $R_B = R_H(v_H/v_B)^2$ is reduced by $\sim (v_B/v)^3$. The formation rate for binaries with separation $R_B = R_H(v_H/v_B)^2$ is

$$FR_{L^3}(R_B > R_{crit}) \sim \left(\frac{\Sigma}{\rho R}\right)^2 \alpha^{-4} \left(\frac{v_H}{v}\right)^6 \left(\frac{v_H}{v_B}\right)^5 \Omega. \tag{3.27}$$

These wider binaries ($R_B > R_{crit}$) have a higher formation rate compared to the tight ones which have a separation $\sim R_{crit}$. The ratio of the formation rate (equation [3.27]) to the destruction rate (equation [3.24]) yields an equilibrium abundance of binaries per KBO at any given time that is given by

$$\frac{N_{KBB}}{N_{KBO}} \sim \frac{\Sigma}{\rho R} \alpha^{-2} \left(\frac{v_H}{v}\right)^4 \left(\frac{v_H}{v_B}\right)^3. \tag{3.28}$$

The number of binaries scales as $(R_B/R_H)^{3/2}$. Binaries with separation R_B are therefore $(R_B/R_{crit})^{3/2} \sim (v/v_B)^3$ times more common than those with separation R_{crit} provided there is sufficient time for the equilibrium to be established. The same statistical equilibrium abundance can be derived using phase-space arguments. The phase-space number density of KBOs is $(\Sigma\Omega)/(\rho R^3 v^4)$. The phase-space volume corresponding to a binary separation R_B and velocity v_B is $R_B^3 v_B^3 = R_H^3 v_H^3 (v_H/v_B)^3$. Multiplying the KBO phase-space number density by the binary phase space volume

yields a statistical equilibrium abundance per KBO of

$$\frac{N_{KBB}}{N_{KBO}} \sim \frac{\Sigma\Omega}{\rho R^3 v^4} R_H^3 v_H^3 \left(\frac{v_H}{v_B}\right)^3 \sim \frac{\Sigma}{\rho R}\alpha^{-2}\left(\frac{v_H}{v}\right)^4\left(\frac{v_H}{v_B}\right)^3, \tag{3.29}$$

which is in agreement with the binary abundance derived in (3.28). Whether any of these binaries would survive the dynamical excitation of the Kuiper Belt remains an open question.

The L^2s mechanism fails in creating binaries with separations $\sim R_{crit}$, since dynamical friction is not able to dissipate sufficient energy for tight binaries to form. Dynamical friction is only able to assist in the formation of binaries with wide separations ($\sim R_H$) that form from KBOs that happen to approach each other with low relative velocities ($\sim v_H$). This reduces the number density of KBOs that can participate in binary formation by a factor of $\sim (v_H/v)^3$. In this case, the L^2s formation rate is given by

$$FR_{L^2s}(R_B \sim R_H) \sim D\left(\frac{\Sigma}{\rho R}\right)\alpha^{-2}\left(\frac{v_H}{v}\right)^4\Omega \sim \left(\frac{\Sigma}{\rho R}\right)^2\alpha^{-4}\left(\frac{v_H}{v}\right)^8\Omega \tag{3.30}$$

where we have substituted for D from equation (3.23) in the last step. These wide binaries face the same fate as the wide ones formed via the L^3 mechanism in that they will be broken up quickly due to scattering of other large bodies. However, the L^2s mechanism does not even contribute significantly to the binary equilibrium abundance calculated in equation (3.28), since $FR_{L^2s}(R_B \sim R_H)/FR_{L^3}(R_B \sim R_H) \sim (v_H/v)^2 \ll 1$. Therfore, the L^2s mechanism does not play an important role in KBB formation if super-Hill velocities prevail.

In summary, the L^3 mechanism forms tight binaries, that tend to be saved from break up, at a rate that is reduced by a factor of $(v_H/v)^{11}$ compared to the sub-Hill case. In addition, the L^3 mechanism forms wider binaries ($R_B > R_{crit}$), at a higher rate that is "only" reduced by a factor of $(v_H/v)^6(v_H/v_B)^5$ relative to the sub-Hill rate. These wide binaries are constantly created and destroyed, leading to an equilibrium abundance of binaries that scales as $(R_B/R_H)^{3/2}$. The L^2s mechanism is

not important if KBOs have super-Hill velocities.

3.7 Frequency of Long-Lived Transient Binaries and Their Significance for Binary Formation

Astakhov et al. (2005) propose that transient binaries that spent a time of $15\Omega^{-1}$ ($\sim$ 600yr at 40AU) or longer in their mutual Hill sphere, near a periodic orbit, are responsible for binary formation in the L^2s and L^3 mechanisms. Here, we determine how the frequency of long-lived transient binaries depends on the transient binary lifetime. This allows us to quantify the importance of long-lived transient binaries for the overall binary formation. Finally, we address the significance of long-lived transient binaries for the L^2s and L^3 formation mechanisms.

3.7.1 Frequency of Long-Lived Transient Binaries

First, we assess how common long-lived transient binaries are. We integrate equations (3.17) and (3.18) without the dynamical friction term and determine the time t_{3R_H} over which the separation between the two KBOs is less than $3R_H$ for all KBOs that approach one another to R_H and less. We chose to calculate the time the two KBOs spent with a separation of less than $3R_H$ to allow for orbits that reach slightly outside of R_H but return back to within R_H during the encounter. We integrate $\sim 10^5$ orbits in total with impact parameters ranging from $2.2R_H$ to $3.2R_H$. Impact parameters outside this range result in a distance of closest approach between the two KBOs of more than R_H. As initial conditions, we assume that the orbits of the bodies are circular. Figure 3.2 shows that the frequency of transient binaries decreases exponentially with the transient binary lifetime, t_{3R_H}. The line of best fit yields a differential transient binary frequency, valid for $t_{3R_H} \gtrsim 1\Omega^{-1}$, of

$$\frac{d(FR_{tb})}{d(t_{3R_H}\Omega)} = 1.0 \times 10^{-(0.25 t_{3R_H}\Omega)} \frac{\Sigma}{\rho R} \alpha^{-2} \Omega. \tag{3.31}$$

The frequency of transient binaries that spend a time of $\gtrsim 15\Omega^{-1}$ with a separation of less than $3R_H$ is 3 orders of magnitude smaller than that of short-lived ones with $t_{3R_H} \gtrsim 3\Omega^{-1}$. The analysis discussed here was carried out assuming that the KBOs approach each other with relative velocities $v_{rel} < v_H$. Long-lived transient binaries do not exist for bodies that encounter each other at $v_{rel} \gg v_H$. This can be understood by looking at the Jacobi constant. The Jacobi constant in Hill coordinates with length scaled by R_H and time by Ω^{-1} is given by

$$C_J = 3x^2 - z^2 + \frac{12}{(x^2 + y^2 + z^2)^{1/2}} - \dot{x}^2 - \dot{y}^2 - \dot{z}^2. \tag{3.32}$$

KBOs that approach each other with $v_{rel} \gg v_H$ at R_H will experience at most one encounter before they separate. Evaluation of their Jacobi constant at R_H yields that it is large and negative. In order to experience multiple encounters, KBOs must approach each other with $v_{rel} \sim v_H$ at R_H which corresponds to C_J of order unity. Since the Jacobi constant is a conserved quantity, we can be sure that no long-lived transient binaries exist for KBOs that encounter each other at $v_{rel} \gg v_H$. Long-lived transient binaries therefore offer no solution to the fine-tuning problem, contrary to claims by Lee et al. (2007). For KBOs with a given velocity distribution there always exist a few bodies that have $v_{rel} < v_H$ even if $v \gg v_H$. Such bodies can give rise to long-lived transient binaries in the same way that they can form wide binaries (see §3.6 for details), but the frequency of transient binaries due to such bodies is reduced by a factor of $(v_H/v)^4$.

3.7.2 Importance of Long-Lived Transient Binaries in the L^3 Formation Mechanism

Lee et al. (2007) claim that the probability of binary formation from transient binaries with $t_{3R_H} \lesssim 2.5\Omega^{-1}$ is extremely small and they therefore include only transient binaries with $t_{3R_H} \gtrsim 5\Omega^{-1}$ in the main set of their integrations. However, their conclusion that the probability of binary formation from transient binaries with $t_{3R_H} \lesssim 2.5\Omega^{-1}$

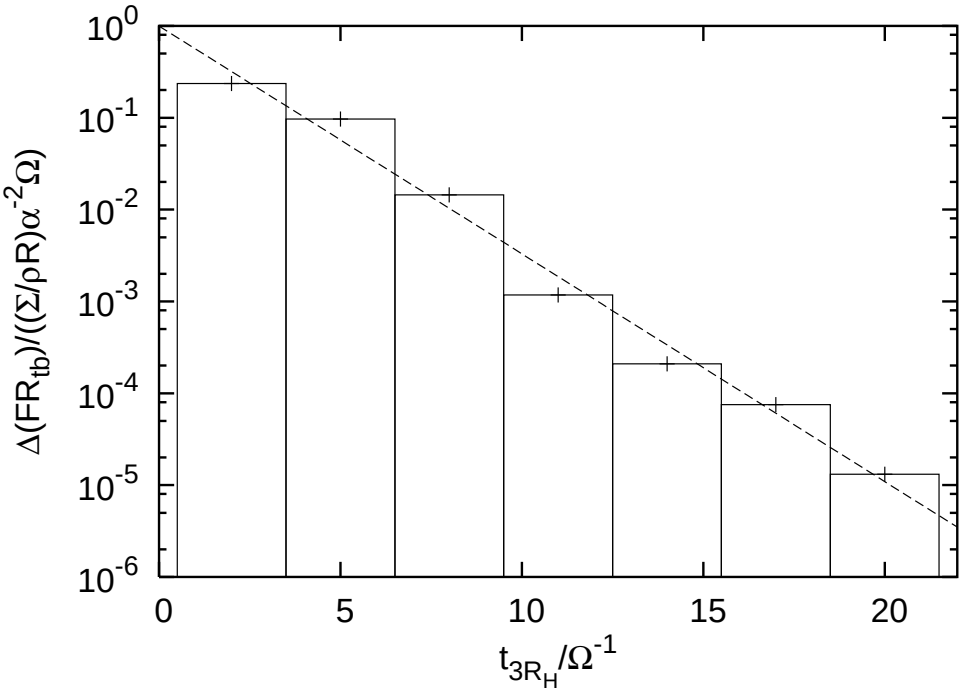

Figure 3.2 Differential transient binary frequency, $\Delta(FR_{tb})$, as a function of the transient binary lifetime, t_{3R_H}, in the shear-dominated velocity regime, where t_{3R_H} is the time the transient binary separation is less than $3R_H$. The frequency decreases exponentially with $t_{3R_H}\Omega$.

is extremely small is due to a bias in their initial conditions that discriminates against binary formation from transient binaries with $t_{3R_H} \lesssim 5\Omega^{-1}$. The shortcoming of their analysis is due to the fact that they launch the third body from an initial separation $> 38R_H$ when the first two KBOs come within a few R_H of each other.[2] Since Lee et al. (2007) select the initial conditions for the third body such that it penetrates within $2.5R_H$, the largest impact parameter is $\sim 4.5R_H$. The minimum time it takes for the third body to come within a few R_H of the transient binary is therefore $\sim 38R_H/(1.5\times 4.5R_H\Omega) \sim 5.6\Omega^{-1}$. The third body therefore only reaches the vicinity of the transient binary for $t_{3R_H} \gtrsim 5.6\Omega^{-1}$, but it is exactly this proximity of the third body that is required for binary formation by strong gravitational scattering. This explains why Lee et al. (2007) find such a small probability for binary formation by transient binaries with $t_{3R_H} \lesssim 5.6\Omega^{-1}$. The range of impact parameters that lead to binary formation is comparable for short- and long-lived transient binaries. This means that the transient binary lifetime is the only advantage long-lived transient binaries have compared to short-lived ones, in terms of binary formation likelihood. However, as we showed in §3.7, the frequency of transient binaries drops exponentially as a function of their lifetime. The ratio of the binary formation rate due to short-lived transient binaries ($t_{3R_H} \gtrsim 3\Omega^{-1}$) compared to that due to long-lived ones ($t_{3R_H} \gtrsim 15\Omega^{-1}$), is therefore

$$\frac{FR(t_{3R_H} \gtrsim 3\Omega^{-1})}{FR(t_{3R_H} \gtrsim 15\Omega^{-1})} \sim \frac{3\Omega^{-1}}{15\Omega^{-1}} \frac{10^{-(0.25\times 3)}}{10^{-(0.25\times 15)}} \sim 200. \tag{3.33}$$

Although the binary formation rate scales linearly with transient binary lifetime, the frequency of transient binaries drops exponentially as a function of its lifetime. Therefore, long-lived transient binaries are not important for binary formation via the L^3 mechanism.

[2]The numerical values stated by Lee et al. (2007) are multiplied by a factor of $2^{1/3}$ to compensate for the different definitions of R_H

3.7.3 Importance of Long-Lived Transient Binaries in the L^2s Formation Mechanism

In general, KBOs that spend a longer time in the Hill sphere lose more energy due to dynamical friction, and are therefore more likely to be captured. However, they might not be responsible for the majority of the binary formation, if the frequency for long-lived transient binaries is sufficiently small. To address this question we determine the typical time, t_{Typ}, required for a transient binary to become bound with the aid of dynamical friction. We define t_{Typ} as the time it takes for 50% of all the KBOs, that form a binary to become bound for a given strength of dynamical friction D; t_{Typ} is measured from the point at which the relative separation between the two KBOs is less than $3R_H$. We determine t_{Typ} in the following way. First, we integrate the same equations as in §3.4 (i.e., eqs. [3.17] and [3.18]). We switch off the dynamical friction at different times and continue the evolution of the KBOs until $t = 1000\Omega^{-1}$. This process is repeated until we find the time for which dynamical friction has to act for 50% of all KBOs that form a binary to become bound. A transient binary is considered to have become bound when it remains a binary (i.e., relative separation $< 3R_H$) until $t = 1000\Omega^{-1}$. We repeat this for different D in order to reveal the relationship between t_{Typ} and D. Again, impact parameters are chosen to range from $2.2R_H$ to $3.2R_H$. Figure 3.3 shows that, for $D \gtrsim 0.002$, the typical time for permanent capture does not depend linearly on the strength of the dynamical friction D, but shows a weaker logarithmic dependence. The typical time t_{Typ} only ranges from $\sim 2\Omega^{-1}$ for $D \sim 0.2$ to $\sim 10\Omega^{-1}$ for $D \sim 0.002$. Furthermore, Figure 3.3 shows a noticeable break around $D \sim 0.001$; for $D \lesssim 0.001$ t_{Typ} increases significantly to $20\Omega^{-1}$ and more. From this, we conclude that longevity of the transient binary (as discussed by Astakhov et al. (2005) with $t_{3R_H} \geqslant 15\Omega^{-1}$) becomes only important for very weak dynamical friction (i.e., $D \lesssim 0.002$) and is most likely not crucial for KBB formation. In §3.4 we estimate $D \sim 0.12$, in which case longevity of transient binaries ($t_{3R_H} \geqslant 15\Omega^{-1}$) is unlikely to be a major requirement for binary formation.

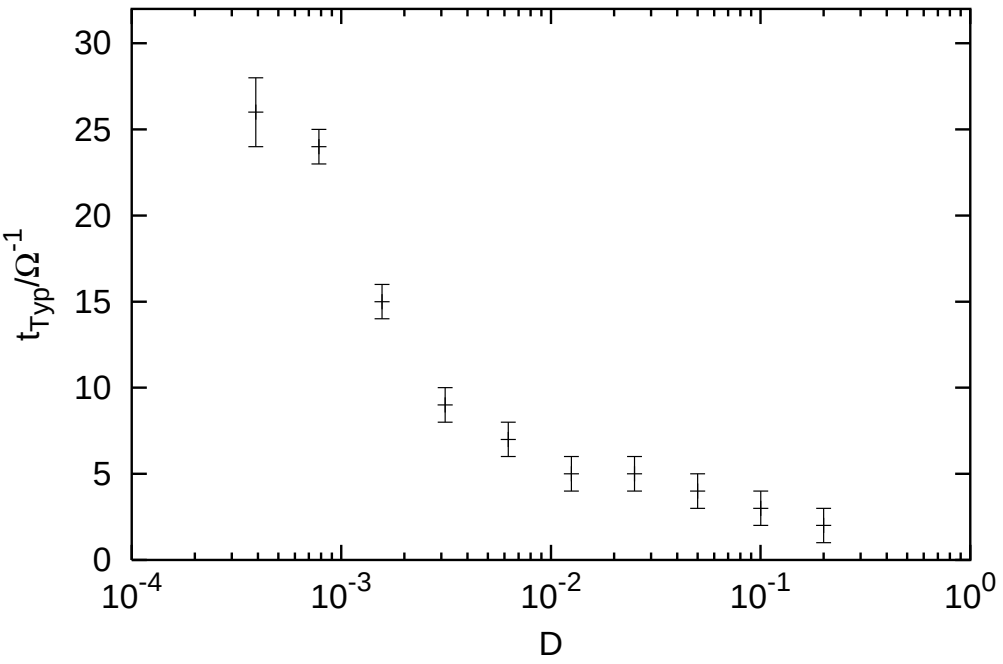

Figure 3.3 Variation of t_{Typ}, the time taken for 50% of binaries to become bound, plotted against strength of dynamical friction D. For about 2 orders of magnitude change in D ($D \sim 0.2$ to $D \sim 0.002$), t_{Typ} only changes from $\sim 2\Omega^{-1}$ to $\sim 10\Omega^{-1}$. A rapid rise in t_{Typ} occurs for $D \lesssim 0.001$.

3.8 Summary and Conclusions

We accurately determine the L^2s and L^3 formation rates for $v < v_H$. We find that while the L^2s formation rate is close to previous order of magnitude estimates, the L^3 formation rate is about a factor of 4 smaller. For $v \ll v_H$, the ratio of the L^3 to the L^2s formation rates is $\sim 0.05(v/v_H)$ and is independent of what sets D. It is therefore independent of the velocity dispersion of the small bodies, their surface density, and the importance of collisions among the small bodies. For sub-Hill KBO velocities, binaries in the Kuiper Belt are formed primarily due to dynamical friction rather than three-body encounters. For super-Hill KBO velocities ($v \gg v_H$) the L^2s mechanism becomes unimportant. The L^3 mechanism forms tight binaries that tend to be saved from break up at a rate that is reduced by a factor of $(v_H/v)^{11}$ compared to the sub-Hill case. In addition, the L^3 mechanism forms wider binaries ($R_B > R_{crit}$), at a higher rate that is "only" reduced by a factor of $(v_H/v)^6(v_H/v_B)^5$ relative to the sub-Hill rate. These wide binaries are constantly created and destroyed leading to an equilibrium abundance of binaries that scales as $(R_B/R_H)^{3/2}$. Whether and how any of these wide binaries would survive the dynamical excitation of the Kuiper Belt remains an open question.

In addition, we determine the frequency of long-lived transient binaries. We show that the frequency of long-lived transient binaries drops exponentially with the system's lifetime for $v_{rel} < v_H$. About 1000 transient binaries occur with $t_{3R_H} \gtrsim 3\Omega^{-1}$ for each transient binary with $t_{3R_H} \gtrsim 15\Omega^{-1}$. The long-lived transient binaries investigated by Astakhov et al. (2005) and Lee et al. (2007) are therefore very rare. Long-lived transient binaries are not important for binary formation via the L^3 mechanism, since the binary formation rate scales only linearly with transient binary lifetime, but the frequency of transient binaries drops exponentially as a function of its lifetime. Long-lived transient binaries do not exist for $v_{rel} \gg v_H$. We show that the apparent shortage of binaries forming from short-lived transient binaries (i.e., $t_{3R_H} \lesssim 2.5\Omega^{-1}$) found by Lee et al. (2007) can be explained by a bias in their initial conditions that discriminates against binary formation from transient binaries with $t_{3R_H} \lesssim 5\Omega^{-1}$. Fi-

nally, to assess the importance of long-lived transient binaries in the L^2s mechanism, we determine the typical time t_{Typ} required for a transient binary to become bound with the aid of dynamical friction. We show that longevity of the transient binary (as discussed by Astakhov et al. (2005) with $t_{3R_H} \geqslant 15\Omega^{-1}$) only becomes important for very weak dynamical friction (i.e., $D \lesssim 0.002$). We estimate $D \sim 0.12$, in which case longevity of transient binaries ($t_{3R_H} \geqslant 15\Omega^{-1}$) is unlikely to be a major requirement for binary formation.

Acknowledgments We thank Peter Goldreich for stimulating discussions and the anonymous referee for valuable comments that helped to clarify this chapter. Some of the numerical calculations presented here were performed on Caltech's Division of Geological and Planetary Sciences Dell cluster.

Chapter 4

The Ratio of Retrograde to Prograde Orbits: A Test for Kuiper Belt Binary Formation Theories[1]

With the discovery of Kuiper Belt binaries that have wide separations and roughly equal masses, new theories were proposed to explain their formation. Two formation scenarios were suggested by Goldreich and collaborators. In the first, dynamical friction generated by a sea of small bodies enables a transient binary to become bound (the L^2s mechanism); in the second, a transient binary gets bound by an encounter with a third body (the L^3 mechanism). We show that these different binary formation scenarios leave their own unique signatures in the relative abundance of prograde to retrograde binary orbits. This signature is due to the fact that stable retrograde orbits can exist much further out in the Hill sphere than prograde orbits. This provides an excellent opportunity to distinguish between the different binary formation scenarios observationally. We predict that if binary formation proceeded while sub-Hill velocities prevailed, the vast majority of all binaries with comparable masses would have retrograde orbits. This dominance of retrograde binary orbits is a result of binary formation via the L^2s mechanism, or any other mechanism that

[1]This chapter was previously published in similar form as Schlichting, H. E., & Sari, R. 2008, ApJ, 686, 741.

dissipates energy in a smooth and gradual manner. For super-Hill velocities, binary formation proceeds via the L^3 mechanism, which produces a roughly equal number of prograde and retrograde binaries. These predictions assume that subsequent orbital evolution due to dynamical friction and dynamical stirring of the Kuiper Belt did not alter the sense of the binary orbit after formation.

4.1 Introduction

The detection of binaries with comparable masses and wide separations in the Kuiper Belt called for new theories to explain their formation (e.g., Weidenschilling, 2002; Goldreich et al., 2002; Funato et al., 2004; Astakhov et al., 2005; Lee et al., 2007). Their existence cannot be explained with a formation scenario that involves a collision and tidal evolution, as has been proposed for the formation of the Moon and Charon (Hartmann & Davis, 1975; Cameron & Ward, 1976; McKinnon, 1989), since it cannot account for the current angular momentum of the binary system. In a formation scenario proposed by Weidenschilling (2002) two Kuiper Belt objects (KBOs) collide with each other inside the Hill sphere of a third. However, in the Kuiper Belt, gravitational scattering between the two intruders is about 100 times[1] more common than a collision. Therefore, three-body gravitational deflection (the L^3 mechanism), as proposed by Goldreich et al. (2002), should dominate the binary formation over such a collisional scenario. A second binary formation scenario suggested by Goldreich et al. (2002), called the L^2s mechanism, consists of the formation of a transient binary that gets bound with the aid of dynamical friction from a sea of small bodies. In the formation scenario of Astakhov et al. (2005) and Lee et al. (2007), the existence of long-lived transient binaries that spend a long time in their mutual Hill sphere, near a periodic orbit, is responsible for the creation of Kuiper Belt binaries (KBBs). Finally, Funato et al. (2004) proposed a binary formation mechanism that involves a collision between two large KBOs. This collision creates a small moon that is replaced in an

[1]For this estimate we used $\alpha \sim 10^{-4}$ and assumed that the velocity dispersion of the KBOs at the time of binary formation is less than their Hill velocity; see §4.2 for details

exchange reaction by a massive body with a high eccentricity and a large semi-major axis.

In this chapter, we show that the L^2s and L^3 mechanisms leave unique signatures in the relative abundance of prograde to retrograde binary orbits. The L^2s mechanism dominates over the L^3 mechanism for sub-Hill velocities (see Chapter 3). We argue that binaries formed from dynamically cold KBOs by the L^2s mechanism have retrograde orbits. This is due to the existence of stable retrograde binary orbits with modified Jacobi constants similar to those of unbound KBOs on circular orbits that have impact parameters that correspond to distances of closest approach of less than the Hill radius. No equivalent prograde orbits exist (e.g., Henon, 1970; Innanen, 1979; Zhang & Innanen, 1988; Hamilton & Burns, 1991; Hamilton & Krivov, 1997). Since dynamical friction only gradually increases the modified Jacobi constant (for a binary, this corresponds to gradually increasing the absolute value of the binding energy), all binaries that form via the L^2s mechanism, or any other mechanism that dissipates energy in a smooth and gradual manner, will start with modified Jacobi constants that are close to those of unbound KBOs that penetrate the Hill sphere and hence have retrograde orbits. For super-Hill KBO velocities, only the L^3 mechanism can form tight binaries that tend to survive (see Chapter 3). The fact that retrograde orbits are stable for larger semi-major axes is no longer of importance, since only tight binaries are saved from break-up. This therefore leads to the formation of a roughly equal number of prograde and retrograde binaries for super-Hill KBO velocities.

This chapter is structured as follows. In §4.2 we outline our assumptions, explain our choice of parameters, and define variables that will be used throughout this chapter. We calculate the ratio of prograde to retrograde binary orbits for the L^2s and L^3 mechanisms and predict the relative abundance of prograde to retrograde orbits for sub-Hill and super-Hill KBO velocities in §4.3. We compare our predictions with observations in §4.4. Discussion and conclusions follow in §4.5.

4.2 Definitions and Assumptions

The Hill radius denotes the distance from a body at which the tidal forces due to the Sun and the gravitational force due to the body, both acting on a test particle, are in equilibrium. It is given by

$$R_H \equiv a_\odot \left(\frac{m_1 + m_2}{3M_\odot} \right)^{1/3} \tag{4.1}$$

where m_1 and m_2 are the masses of the two KBOs, $a_\odot$ is their semi-major axis around the Sun, and $M_\odot$ is the mass of the Sun. Our definition of the Hill radius differs from that used in Chapter 3, since we include the combined mass of both KBOs here. We chose to do so since it will make comparisons with works by other authors easier.

We use the "two-group approximation" (Goldreich et al., 2002, 2004b), which consists of the identification of two groups of objects: small ones, which contain most of the total mass, with surface mass density σ; and large ones, which contain only a small fraction of the total mass, with surface mass density $\Sigma \ll \sigma$. We assume that $\sigma \sim 0.3\text{g cm}^{-2}$, which is the extrapolation of the minimum-mass solar nebula (Hayashi, 1981) to a heliocentric distance of 40AU. Estimates from Kuiper Belt surveys (Trujillo et al., 2001; Trujillo & Brown, 2003; Petit et al., 2008; Fraser et al., 2008; Fuentes et al., 2009) yield a value of $\Sigma \sim 3 \times 10^{-4}\text{g cm}^{-2}$ for KBOs with radii of $R \sim 100$ km. We use this value of Σ, assuming that the value of Σ during the formation of KBBs was the same as it is now. Our choices for the values of Σ and σ are also consistent with results from numerical coagulation simulations by Kenyon & Luu (1999).

Large bodies grow by the accretion of small bodies. Large KBOs viscously stir the small bodies, increasing the small bodies' velocity dispersion u. As a result, u grows on the same timescale as R, provided that mutual collisions among the small bodies are not yet important. In this case, u is given by

$$\frac{u}{v_H} \sim \left(\frac{\Sigma}{\sigma\alpha} \right)^{1/2} \sim 3 \tag{4.2}$$

where $\alpha = R/R_H \sim 10^{-4}$ at 40AU (Goldreich et al., 2002) and v_H is the Hill velocity of the large bodies, which is given by $v_H = \Omega R_H$, where Ω is the orbital frequency around the Sun. The velocity v of the large KBOs increases due to mutual viscous stirring, but is damped by dynamical friction from a sea of small bodies such that $v < u$. Balancing the stirring and damping rates of v and substituting for u from equation (4.2), we find that

$$\frac{v}{v_H} \sim \alpha^{-2} \left(\frac{\Sigma}{\sigma}\right)^3 \sim 0.1. \tag{4.3}$$

For our choice of parameters, we have sub-Hill KBO velocities during the epoch of formation of bodies with $R \sim 100$km. We therefore focus our work on the shear-dominated velocity regime ($v \ll v_H$). However, we also discuss how our results would be modified if $v \gg v_H$.

4.3 Prograde Versus Retrograde Binary Orbits

4.3.1 Sub-Hill Velocities: $v \ll v_H$

The disk of KBOs is effectively two-dimensional in the shear-dominated velocity regime ($v \ll v_H$), since the growth of their inclinations is suppressed (Wetherill & Stewart, 1993; Rafikov, 2003; Goldreich et al., 2004b). We therefore restrict our calculations for the shear-dominated velocity regime to two dimensions. Since we are interested in close encounters among the KBOs, their interaction is well described by Hill's equations (Hill, 1878; Goldreich & Tremaine, 1980; Henon & Petit, 1986). In Hill coordinates, the equations of motion of the two KBOs can be decomposed into their center-of-mass motion and their relative motion with respect to one another. The modified Jacobi constant is exactly conserved in the Hill formalism, but the Hill formalism itself is an approximation to the general three-body problem. It assumes that the masses of bodies 1 and 2 (in our case, the two KBOs) are much less than that of the Sun. We use the standard Hill coordinate system and reference frame, as in Henon & Petit (1986) and Ida (1990). In this rotating frame, the direction of

the x-axis is given by the line connecting the Sun and the center of mass of the two KBOs, such that the positive x-direction is pointing away from the Sun. The y-axis is perpendicular to the x-axis, pointing in the direction of the motion of the KBOs' center of mass around the Sun. In Hill coordinates, the modified Jacobi constant is

$$J_C = 3x^2 + \frac{6}{(x^2+y^2)^{1/2}} - \dot{x}^2 - \dot{y}^2 \tag{4.4}$$

where x and y correspond to the relative separation between the two KBOs in the x- and y-directions, respectively (Henon & Petit, 1986). Length has been scaled by R_H and time by Ω^{-1}. In Hill coordinates, the Lagrangian points L_1 and L_2 are located at $(-1, 0)$ and $(+1, 0)$, respectively, where we define L_1 as the Lagrangian point located between the KBO and the Sun. Their modified Jacobi constants are $J_C(L_1) = J_C(L_2) = 9$. From equation (4.4), we can see that tight binaries with small separations have values of $J_C \gg 9$. We call a binary orbit prograde if its angular momentum about the binary center of mass, as viewed in the non-rotating frame, is in the same direction as the orbital angular momentum of the binary around the Sun. If the binary angular momentum is in the opposite direction to the orbital angular momentum of the binary around the Sun, the orbit is called retrograde. Several authors recognized that planar retrograde orbits are stable for larger semi-major axes than prograde orbits (e.g., Henon, 1970; Innanen, 1979; Zhang & Innanen, 1988; Hamilton & Burns, 1991; Hamilton & Krivov, 1997). A prograde binary with an initially circular orbit becomes unbound for values of $a \gtrsim 0.49 R_H$, where a is the initial semi-major axis of the mutual binary orbit (Hamilton & Burns, 1991). This implies that prograde orbits with modified Jacobi constants that are less than those of the Lagrangian points L_1 and L_2 are unbound. In contrast to the prograde case, there exist stable retrograde binary orbits that have values of $J_C \lesssim J_C(L_1) = J_C(L_2) = 9$. This result is also shown in Figure 4.1. Figure 4.1 shows histograms of J_C for prograde and retrograde binaries formed by the L^3 mechanism from KBOs with initially circular orbits around the Sun. In the remainder of this chapter, we discuss the stability of prograde and retrograde orbits in terms of J_C and not the semi-major axis, since the

latter is not well defined (i.e., it is not a constant of motion) for wide orbits with $a \sim R_H$. The modified Jacobi constant for two KBOs that approach each other from infinity is

$$J_C = 3x^2 - \dot{x}^2 - \dot{y}^2 = \frac{3}{4}b^2 - e^2 \tag{4.5}$$

where b is the initial separation between the two KBOs in the x-direction and e is the relative eccentricity in Hill units, given by $|\mathbf{e_1} - \mathbf{e_2}|$ where $\mathbf{e_1}$ and $\mathbf{e_2}$ are the eccentricity vectors of body 1 and body 2, respectively. Only KBOs with values of b ranging from $1.7R_H$ to $2.5R_H$ penetrate each other's Hill spheres if started on circular orbits. From equation (4.5), we have therefore determined that only KBOs with values of $2.2 \leq J_C \leq 4.7$ have a distance of closest approach of R_H or less, provided that they started on circular orbits around the Sun.

4.3.1.1 L^2s Mechanism

In the L^2s mechanism, KBBs form from transient binaries that become bound with the aid of dynamical friction from a sea of small bodies. This dynamical friction provides a gentle force that damps the random velocity of large KBOs. For typical parameters, the dynamical friction force only extracts a small fraction of energy over an orbital timescale. Therefore, KBBs that form via the L^2s mechanism, or any other mechanism that dissipates energy gradually, have initially modified Jacobi constants similar to those of the unbound KBOs that penetrate within the Hill sphere. As mentioned above, for KBOs that started on circular orbits around the Sun, this corresponds to values of $2.2 \leq J_C \leq 4.7$. However, only stable retrograde orbits exist for values $J_C \lesssim 9$. This implies that all KBBs that form this way must have retrograde orbits, since no stable prograde orbits exist for values of $J_C \lesssim 9$. Once a binary is formed, dynamical friction increases the modified Jacobi constant and the absolute value of the binary binding energy. We confirm that all binaries that form from KBOs on initially circular orbits around the Sun via the L_s^2 mechanism are retrograde by numerical integrations that are presented below.

Since it is not feasible to examine the interactions with each small body individ-

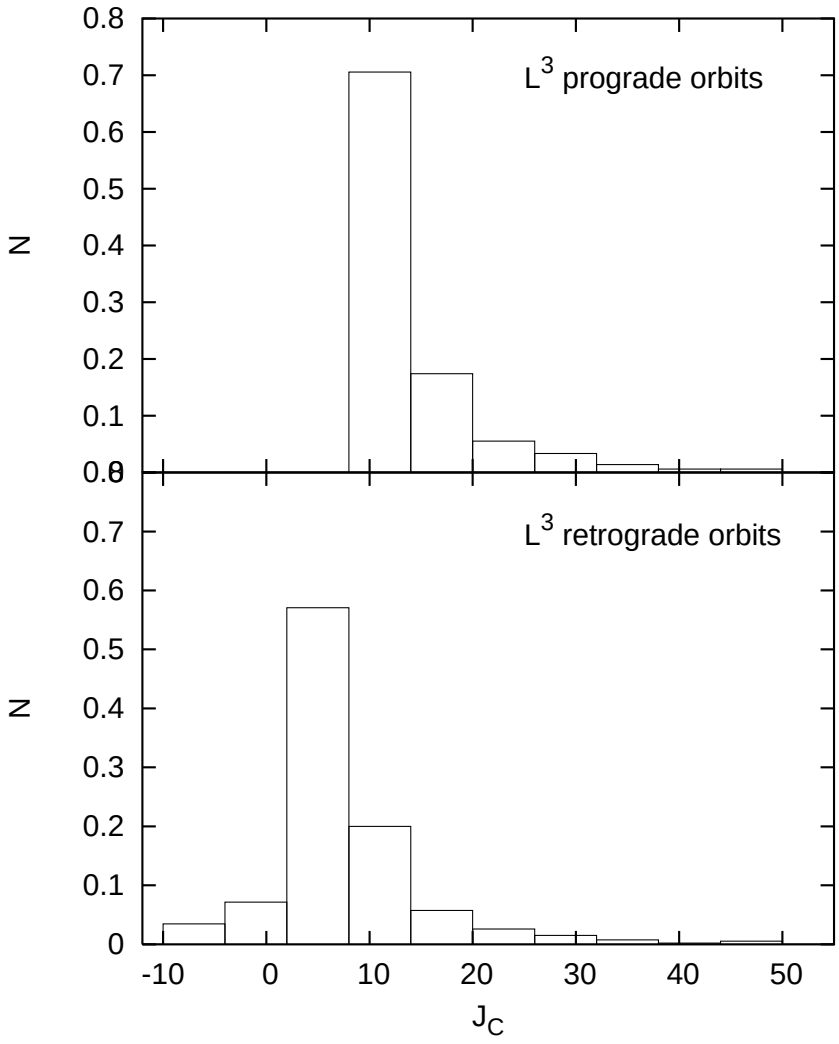

Figure 4.1 Histograms of the modified Jacobi constants, J_C, of prograde and retrograde KBBs that formed via three-body gravitational deflection, the L^3 mechanism, for $v \ll v_H$. Each histogram is normalized to unity, but overall, the retrograde orbits are twice as abundant as the prograde orbits. Note that prograde binaries exist only for values of $J_C \gtrsim 9$, whereas retrograde binaries also exist for values of $J_C \lesssim 9$.

ually, their net effect is modeled by an averaged force that acts to damp the large KBOs' non-circular velocity around the Sun. We parameterize the strength of the damping by a dimensionless quantity D, defined as the fractional decrease in non-circular velocity due to dynamical friction over a time Ω^{-1}:

$$D \sim \frac{\sigma}{\rho R}\left(\frac{u}{v_H}\right)^{-4}\alpha^{-2} \sim \frac{\Sigma}{\rho R}\alpha^{-2}\left(\frac{v}{v_H}\right)^{-1}. \tag{4.6}$$

The first expression is simply an estimate of dynamical friction due to a sea of small bodies, in the regime in which $u > v_H$. The second expression describes the mutual excitation among the large KBOs for values of $v \ll v_H$. The velocity dispersion of the large KBOs, v, achieves a quasi-steady state on a timescale shorter than at which R grows, since only a subset of the deflected bodies are accreted. The stirring among the large KBOs can therefore be equated to the damping due to dynamical friction (for a detailed derivation, see Goldreich et al. (2004b)).

Since the growth of the inclinations is suppressed in the shear-dominated velocity regime, the disk of KBOs is effectively two-dimensional (Wetherill & Stewart, 1993; Rafikov, 2003; Goldreich et al., 2004b). We therefore restrict this calculation to two dimensions. In Hill coordinates, the relative motion of two equal-mass KBOs, including the dynamical friction term, is governed by

$$\ddot{x} - 2\dot{y} - 3x = -\frac{3x}{(x^2+y^2)^{3/2}} - D\dot{x} \tag{4.7}$$

$$\ddot{y} + 2\dot{x} = -\frac{3y}{(x^2+y^2)^{3/2}} - D(\dot{y} + 1.5x). \tag{4.8}$$

Length has been scaled by R_H and time by Ω^{-1}. Equations (4.7) and (4.8) are integrated for different values of D and impact parameters ranging from $1.7R_H$ to $2.5R_H$ with equal step size. Impact parameters outside this range result in a distance of closest approach between the two KBOs of more than R_H.

For $D = 0.01$, we performed 20000 integrations. About 2% of these integrations resulted in the formation of a binary. Figure 4.2 shows three examples of the evolution of the specific angular momentum and J_C of the binary formation events from our

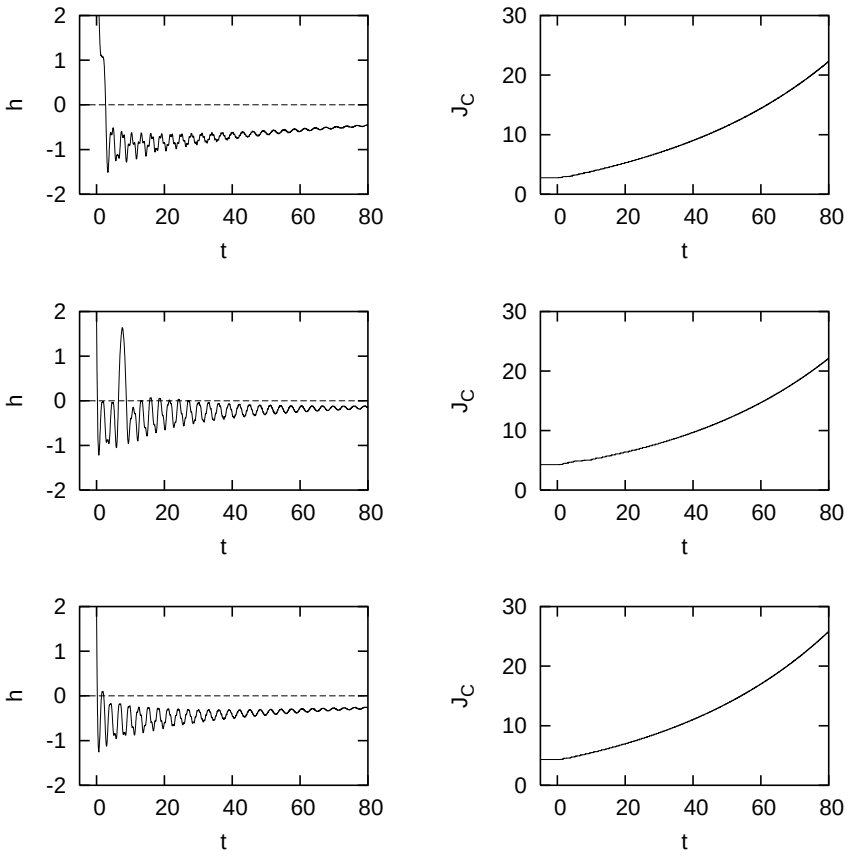

Figure 4.2 Three examples of KBO encounters in the L^2s mechanism for $v \ll v_H$ and $D = 0.01$ that result in the formation of a binary. The plots on the left- and right-hand sides show the evolution of the specific angular momentum, h, and the modified Jacobi constant, J_C, respectively, as a function of time. The time $t = 0$ corresponds to the time at which $y = 0$ if the relative KBO velocity is solely due to the Keplerian shear (i.e., ignoring the actual gravitational interaction between the bodies). The evolution of h and J_C is shown until the binary separation has decreased to $0.1R_H$ or less. These examples show that the sense of rotation is practically preserved. The specific angular momentum, h, displays large variations right after capture that are caused by solar tides. The most extreme case of angular momentum sign change found in our simulations for bodies that form binaries is displayed in the second of the three examples. The angular momenta of the binaries are all negative, corresponding to retrograde binary orbits. In fact, all binaries that form via the L^2s mechanism in our numerical integrations display retrograde orbits. Dynamical friction shrinks the binary separation, leading to a decrease in the magnitude of h and an increase of J_C with time. The modified Jacobi constants of the newly formed binaries are smaller than $J_C(L1) = 9$, which explains why all their orbits are retrograde (see §3.1.1 for details).

integrations for $D = 0.01$. In addition, we performed integrations for values of D ranging from 0.1 to 0.0004 and find that, just as in the $D = 0.01$ case, only retrograde binaries form. We define h as the specific angular momentum of the binary in the non rotating frame. It can be written as $h = x\dot{y} - y\dot{x} + x^2 + y^2$ and is related to the total binary orbital angular momentum, L, by $h = (1/m_1 + 1/m_2)L$. The time $t = 0$ corresponds to the time at which $y = 0$ if the relative KBO velocity is solely due to the Keplerian shear (i.e., ignoring the actual gravitational interaction between the bodies). The evolution of h and J_C is shown until the binary separation has decreased to $0.1R_H$ or less. Binaries with separations of $0.1R_H$ or less are sufficiently tight that perturbations from the Sun are too weak to flip the sign of the angular momentum. As expected from our discussion above, the angular momenta of the binaries are negative corresponding to retrograde binary orbits. In fact, all binaries that form via the L^2s mechanism in our numerical integrations display retrograde orbits. Dynamical friction shrinks the binary separation. As a result, the magnitude of the binary angular momenta decreases with time. The right-hand side of Figure 4.2 shows the evolution of the modified Jacobi constant. Newly formed binaries initially have a modified Jacobi constant of < 9, which is possible only for retrograde binaries. Dynamical friction shrinks the semi-major axes of the binaries, which leads to an increase of J_C with time while keeping the sense of the rotation, i.e., the sign of h, fixed. Eventually the modified Jacobi constant grows to values above $J_C(L1) = J_C(L2) = 9$. For values of $J_C \gtrsim 9$, prograde orbits can exist; however, all binaries that formed with the aid of dynamical friction started out with values of $J_C < 9$, for which only retrograde orbits are stable. Therefore, all KBBs that form via the L^2s mechanism, or any other mechanism that gradually removes energy from transient binaries, orbit each other in the retrograde sense, since otherwise they would not have been able to form in the first place. Figure 4.3 shows the evolution of h and J_C as a function of time for KBO encounters that did not lead to the formation of a binary. These examples show that KBOs encounter each other and leave each other with positive angular momenta. This is a result of the Keplerian shear and follows from the definition of h.

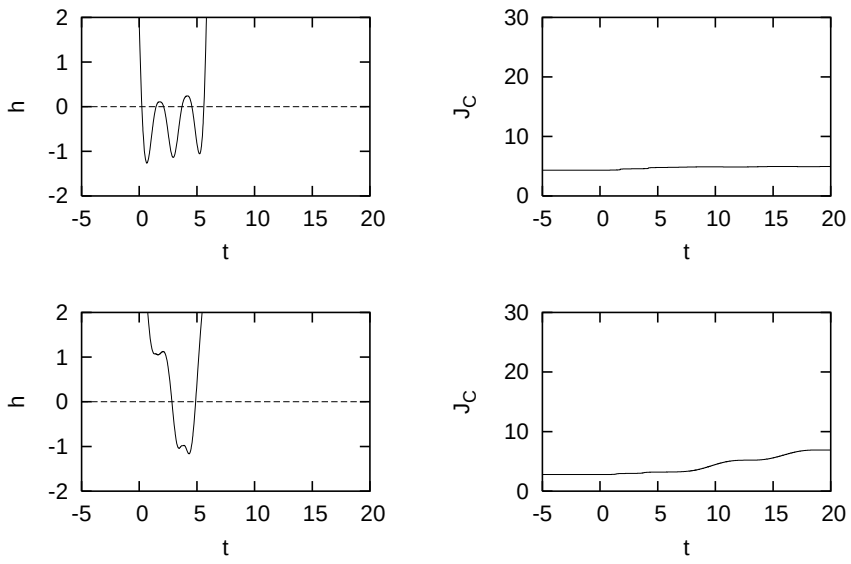

Figure 4.3 Same as in Fig. 4.2 but for two examples of KBO encounters in the L^2s mechanism with $v \ll v_H$ and $D = 0.01$ that do not result in the formation of a binary. As a result of the Keplerian shear, KBOs encounter and leave each other with positive values of h.

We have assumed here that all KBOs are initially on circular orbits around the Sun, and we have shown that this leads to the formation of exclusively retrograde binaries in the L^2s mechanism. If, however, the velocity dispersion of the KBOs is sufficiently large, such that e is of the order of the Hill eccentricity, bigger impact parameters allow the KBOs to penetrate each other's Hill spheres. In this case, there now exist KBOs that have an initial value of J_C just a little below 9 (see eq. [4.5]), in which case only a small change in J_C is sufficient for the formation of retrograde and prograde binaries. Therefore, prograde binaries can form with the aid of dynamical friction, provided that the velocity dispersion of the KBOs is approximately v_H.

Our prediction for the sense of the binary orbit relies on the assumption that dynamical friction does not alter the sense of the binary orbit in the subsequent binary evolution. Although we have shown in our simulations that for our dynamical friction model this is indeed the case, the actual behavior of dynamical friction may differ from the model implemented here.

4.3.1.2 L^3 Mechanism

A transient binary forms when two large KBOs penetrate each other's Hill spheres. This transient binary must lose energy in order to become gravitationally bound. In the L^3 mechanism the excess energy is carried away by an encounter with a third massive body. This encounter can provide a significant change in energy, which corresponds to a considerable change in J_C. The modified Jacobi constants of KBBs that form via the L^3 mechanism are therefore not constrained to values similar to those of their initial J_C; their orbits can therefore be either prograde or retrograde. We show that this is indeed the case with numerical integrations discussed below, and we determine the ratio of prograde to retrograde orbits for binary formation via the L^3 mechanism.

Our calculation is performed in the shear-dominated velocity regime in two dimensions. As an initial condition, we assume that all bodies are on circular orbits. We modify Hill's equations (Hill, 1878; Goldreich & Tremaine, 1980; Petit & Henon, 1986) to include three equal-mass bodies besides the Sun. The equations of motion, with length scaled by R_H and time by Ω^{-1}, for body 1 are given by

$$\ddot{x}_1 - 2\dot{y}_1 - 3x_1 = -\frac{3(x_1 - x_2)}{2[(x_1 - x_2)^2 + (y_1 - y_2)^2]^{3/2}} - \frac{3(x_1 - x_3)}{2[(x_1 - x_3)^2 + (y_1 - y_3)^2]^{3/2}} \quad (4.9)$$

$$\ddot{y}_1 + 2\dot{x}_1 = -\frac{3(y_1 - y_2)}{2[(x_1 - x_2)^2 + (y_1 - y_2)^2]^{3/2}} - \frac{3(y_1 - y_3)}{2[(x_1 - x_3)^2 + (y_1 - y_3)^2]^{3/2}}. \quad (4.10)$$

The subscripts 1, 2, and 3 label the x- and y-coordinates of KBOs 1, 2, and 3, respectively. Similar equations of motion can be obtained for bodies 2 and 3. The resulting binary orbits are calculated by numerically integrating the equations of motion. We refer the reader to Chapter 3 for the exact details of these calculations.

Figure 4.1 shows histograms of the modified Jacobi constants of prograde and retrograde binaries that formed via the L^3 mechanism. Both histograms are normalized to unity. As discussed above, we indeed find that prograde orbits only exist for values of $J_C \gtrsim 9$. The stability of retrograde orbits extends below $J_C = 9$, down to $J_C \sim -10$. It therefore includes the values of J_C for circular heliocentric orbits

that have a distance of closest approach of R_H or less (i.e., $2.2 < J_C < 4.7$). Unlike the L^2s mechanism, the L^3 mechanism does produce both retrograde *and* prograde binaries for $v \ll v_H$. We find that 65% of all binary orbits are retrograde and 35% are prograde (see Fig. 4.4). Here, we only considered binary formation from three equal-mass bodies that started on initially circular orbits around the Sun. We therefore caution that the ratio of prograde to retrograde orbits due to the L^3 mechanism might differ for other mass ratios and velocity dispersions.

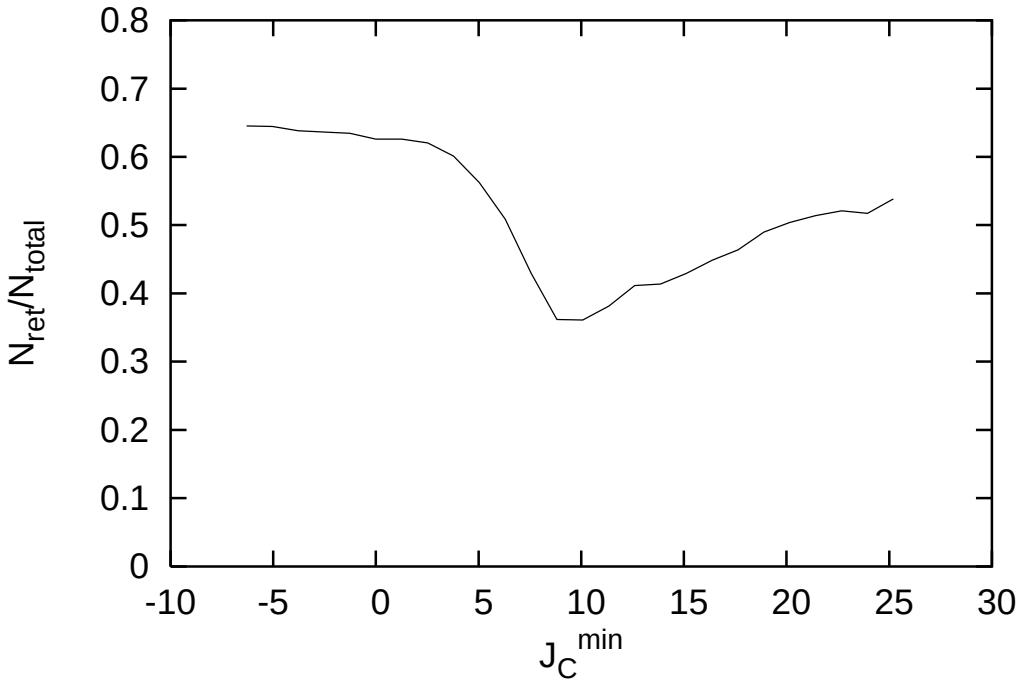

Figure 4.4 Ratio of retrograde binaries, N_{ret}, that have a modified Jacobi constant of J_C^{min} or larger to the total number of binaries, N_{total}, that formed via the L^3 mechanism for $v \ll v_H$. For small values of J_C^{min}, i.e., when all binaries are included, about 2/3 have retrograde orbits. More retrograde than prograde binaries form because retrograde binary orbits are stable further out in the Hill sphere than prograde ones. As J_C^{min} increases the fraction of retrograde binaries decreases reaching a minimum of about 1/3 for $J_C^{min} \sim 9$. This may be due to the Keplerian shear, which increases the duration of a prograde encounter between unbound KBOs compared to a retrograde encounter. The fraction of prograde and retrograde binaries becomes comparable for $J_C^{min} \gg 9$, because for such binaries, neither the Keplerian shear nor the increased stability of retrograde orbits are important.

4.3.1.3 The Ratio of Retrograde to Prograde Orbits

In Chapter 3 we have shown that for sub-Hill KBO velocities the ratio of the L^3 binary formation rate to the L^2s binary formation rate is

$$\frac{FR_{L^3}}{FR_{L^2s}} = 0.05\frac{v}{v_H}. \tag{4.11}$$

Therefore, for sub-Hill KBO velocities, binaries in the Kuiper Belt form primarily because of dynamical friction. For our estimate of $(v/v_H) \sim 0.1$, we find that $FR_{L^3}/FR_{L^2s} \sim 0.005$, in which case $\sim 0.5\%$ of all binaries form directly by the L^3 mechanism. Since prograde binaries can only form via the L^3 mechanism, they make up a negligible fraction of the total binaries. Below we discuss how a somewhat larger fraction of prograde binaries can arise as a result of exchange reactions with unbound KBOs.

Once a binary is formed, its semi-major axis shrinks because of the dynamical friction provided by a sea of small bodies. Dynamical friction decreases the orbit of a KBB that has an orbital velocity v_B at a rate of

$$\mathcal{R}_{sh} \sim D\Omega \sim \frac{\Sigma}{\rho R}\alpha^{-2}\left(\frac{v}{v_H}\right)^{-1} \tag{4.12}$$

where we assume that $v_B < u$. Exchange reactions or binary break-up due to passing KBOs occurs at a rate of

$$\mathcal{R}_{ex} \sim \frac{\Sigma}{\rho R}\alpha^{-2}\Omega\left(\frac{v_B}{v_H}\right)^{-1}. \tag{4.13}$$

The ratio of these two rates is given by

$$\frac{\mathcal{R}_{sh}}{\mathcal{R}_{ex}} \sim \left(\frac{v_B}{v}\right) \tag{4.14}$$

where $v \ll v_H$ and $v_B \gtrsim v_H$. Break up or exchange reactions are most likely for wide binaries, in which case $v_B \sim v_H$ since v_B increases as the semi-major axis of the mutual binary orbit decreases. Therefore, we find from equation (4.14) that

$\mathcal{R}_{sh}/\mathcal{R}_{ex} \sim (v_H/v) \sim 10$ for our estimate of $(v/v_H) \sim 0.1$. This implies that $\sim$ 10% of all binaries that formed will suffer an exchange reaction or break up. We performed numerical integrations of binary break-up and exchange reactions in order to obtain a more accurate estimate, and we find that only about 3% of the binaries suffer an exchange reaction and/or break up. Our order-of-magnitude calculation, therefore, slightly overestimates the number of binaries that experience an exchange reaction and/or break up. Moreover, only a fraction of the these binaries will end up as binaries with prograde orbits. In conclusion, we predict that the vast majority ($\gtrsim$ 97%) of binaries with comparable masses will have retrograde orbits if KBO velocities of $v \lesssim 0.1 v_H$ prevailed during binary formation. This prediction assumes that subsequent orbital evolution due to dynamical friction does not alter the sense of the binary orbit after formation.

4.3.2 Super-Hill Velocity: $v \gg v_H$

There is some uncertainty as to what the actual values of σ and Σ were during binary formation. For a few times larger value of Σ and an unchanged value of σ, we enter the regime in which v exceeds the Hill velocity (this can be seen from eq. [4.3]). We discuss here briefly how this would affect the ratio of prograde to retrograde binary orbits.

In chapter 3 we have shown that for $v \gg v_H$, only binaries that form with a binary separation of $R_{crit} = R_H(v_H/v)^2$ or less tend to be saved from break-up. The L^2s mechanism fails to create binaries with separations of $\sim R_{crit}$ or less since dynamical friction is not able to dissipate sufficient energy for tight binaries to form. Therefore, the L^2s mechanism is not important if the KBOs have super-Hill velocities. Tight binaries (with separations less than $\lesssim R_{crit}$) can form via the L^3 mechanism. However, in this case, the binary formation cross section is significantly reduced with respect to the sub-Hill velocity regime (see Noll et al. (2008) and Chapter 3 for details). The fact that retrograde orbits are stable for larger semi-major axes is no longer of importance, since only tight binaries tend to survive. We therefore

predict that a roughly equal number of prograde and retrograde binaries form if super-Hill velocities prevail. This prediction is supported by Figure 4.4. Figure 4.4 shows the ratio of retrograde binaries with a modified Jacobi constant of J_C^{min} or larger to the total number of binaries that formed via the L^3 mechanism for $v \ll v_H$. When all binaries are included, we find that about 2/3 have retrograde orbits. More retrograde than prograde binaries form because retrograde binary orbits are stable further out in the Hill sphere than prograde ones. As J_C^{min} increases, the fraction of retrograde binaries decreases reaching a minimum of about 1/3 for $J_C^{min} \sim 9$. This may be due to the Keplerian shear, which increases the duration of a prograde encounter between unbound KBOs compared to a retrograde encounter. The fraction of prograde and retrograde binaries becomes comparable for $J_C^{min} \gg 9$, because for such binaries, neither the Keplerian shear nor the increased stability of retrograde orbits are important. This is the relevant regime for binaries that form for $v \gg v_H$ since these large modified Jacobi constants correspond to tight binaries, which are the only binaries that are saved from break-up if super-Hill velocities prevail.

4.4 Comparison with Observations

To date, the orbits of more than a dozen KBBs have been well determined (e.g., Noll et al., 2008). Unfortunately, due to projection effects, the prograde and retrograde orbital solutions of the KBBs are nearly degenerate. This degeneracy can usually only be broken after several years once the viewing angle of the KBBs has changed sufficiently. Very recently, after the submission of our original manuscript, two groups reported unique orbital solutions for the KBBs Typhon-Echidna (Grundy et al., 2008) and 2001 QW_{322} (Petit et al., 2009). Grundy et al. (2008) find a prograde orbit for Typhon-Echidna, and Petit et al. (2009) report a retrograde orbit for 2001 QW_{322}. 2001 QW_{322} has such a large binary separation that, even in the current Kuiper Belt, it experiences significant dynamical interactions with other large KBOs. However, it is too early to draw conclusions for the whole binary population, but if comparable numbers of retrograde and prograde binaries are found, this would imply that

KBBs formed from a dispersion-dominated KBO disk, which would also be consistent with observed binary inclinations. Dispersion-dominated KBO velocities would imply that the value of Σ/σ was larger during binary formation than what we used in equation (4.3). However, the velocity dispersion during binary formation cannot have exceeded v_H significantly, since the binary formation timescales would otherwise become excessively long (see Chapter 3).

4.5 Discussion and Conclusions

The relative abundance of prograde to retrograde orbits enables us to differentiate between various proposed binary formation scenarios observationally. We predict that the vast majority ($\gtrsim 97$ %) of binaries with comparable masses will have retrograde orbits if KBO velocities of $\lesssim 0.1 v_H$ prevailed during their formation. This dominance of retrograde over prograde binary orbits is due to the fact that for sub-Hill velocities, binaries form primarily via the $L^2 s$ mechanism, rather than the L^3 mechanism. Since dynamical friction only gradually increases the modified Jacobi constant, all binaries that form via the $L^2 s$ mechanism, or any other mechanism that dissipates little energy over an orbital timescale, will start with modified Jacobi constants close to those of unbound KBOs. Only stable retrograde orbits exist for binaries with modified Jacobi constants similar to those of KBOs with initially circular orbits around the Sun that penetrate inside the Hill sphere. Therefore, KBBs have retrograde orbits, provided that they form from dynamically cold KBOs via the $L^2 s$ mechanism.

As the KBO velocities approach v_H, the preference of retrograde orbits decreases. Further, we predict that a comparable number of prograde and retrograde binaries form for super-Hill KBO velocities. This is because only the L^3 mechanism can form tight binaries that tend to survive if super-Hill velocities prevail (see Chapter 3). The fact that retrograde orbits are stable for larger semi-major axes is no longer of importance, since only tight binaries tend to survive. This therefore leads to the formation of a roughly equal number of prograde and retrograde binaries for super-Hill KBO velocities.

The analysis presented here has also implications for some of the other proposed binary formation scenarios. Weidenschilling (2002) suggested that KBBs form by a collision among two KBOs inside the Hill sphere of a third. Although the L^3 mechanism dominates over such a collisional binary formation scenario, we briefly discuss our predictions for this collisional binary formation mechanism. For sub-Hill velocities, more retrograde than prograde binaries form, because retrograde binary orbits are stable further out in the Hill sphere than prograde ones (i.e., the phase space for forming retrograde binaries is larger than that for prograde binaries). For super-Hill velocities a comparable number of prograde and retrograde binaries form because the fact that retrograde orbits are stable for larger semi-major axes is no longer of importance, since only tight binaries are saved from break-up. In the formation scenario of Astakhov et al. (2005), the existence of long-lived transient binaries that spend a long time in their mutual Hill sphere, near a periodic orbit, is responsible for the creation of KBBs. Lee et al. (2007) find an excess of prograde over retrograde binaries and suggest that this is a signature of their binary formation process. Our work indicates that an excess of prograde over retrograde binaries might simply be the result of the velocity regime (i.e., $v \sim v_H$) in which the binaries form (see Fig. 4.4).

All of the above predictions rely on the assumption that subsequent orbital evolution due to dynamical friction and dynamical stirring of the Kuiper Belt does not alter the sense of the binary orbit. The Kuiper Belt has undergone a phase of dynamical excitation that probably modified the orbital properties of KBBs. A detailed study on how dynamical stirring of the Kuiper Belt and dynamical friction affects binary inclinations would be very worthwhile for determining whether these effects were able to reverse the binary orbit from prograde to retrograde rotation.

Acknowledgments Some of the numerical calculations presented here were performed on Caltech's Division of Geological and Planetary Sciences Dell cluster.

Chapter 5

The Creation of Haumea's Collisional Family[1]

Recently, the first collisional family was discovered in the Kuiper belt. The parent body of this family, Haumea, is one of the largest objects in the Kuiper belt and is orbited by two satellites. It has been proposed that the Haumea family was created from dispersed fragments that resulted from a giant impact. This proposed origin of the Haumea family is however in conflict with the observed velocity dispersion between the family members (~ 140 m/s) which is significantly less than the escape velocity from Haumea's surface (~ 900 m/s). In this chapter we propose a different formation scenario for Haumea's collisional family. In our scenario the family members are ejected while in orbit around Haumea. This scenario, therfore, naturally leads to a lower velocity dispersion among the family members than expected from direct ejection from Haumea's surface. In our scenario Haumea's giant impact forms a single moon that tidally evolves outward until it suffers a destructive collision from which the family is created. We show that this formation scenario yields a velocity dispersion of ~ 190 m/s among the family members and that it is consistent with the detection of one collisional family in the Kuiper belt which is in good agreement with the observations. We discuss an alternative scenario that consists of the formation and tidal evolution of several satellites that are ejected by collisions with unbound Kuiper belt objects. However, the formation of the Haumea family in this latter way

[1]This chapter has been accepted for publication in the *Astrophysical Journal*.

is difficult to reconcile with the large abundance of Kuiper belt binaries. We therefore favor forming the family by a destructive collision of a single moon of Haumea. The probability for Haumea's initial giant impact in todays Kuiper belt is less than 10^{-3}. In our scenario, however, Haumea's giant impact can occur before the excitation of the Kuiper belt and the ejection of the family members afterwards. This has the advantage that one can preserve the dynamical coherence of the family and explain Haumea's original giant impact which is several orders of magnitude more likely to have occurred in the primordial dynamically cold Kuiper belt compared to the dynamically excited Kuiper belt today.

5.1 Introduction

Collisions are thought to have played a major role in the Kuiper belt ever since its formation (e.g., Davis & Farinella, 1997; Stern & Colwell, 1997; Kenyon & Luu, 1999; Goldreich et al., 2002; Pan & Sari, 2005). This idea is supported further by the recent discovery of the first collisional family in the Kuiper belt (Brown et al., 2007). Haumea (also known as 2003 EL_{61}), one of the largest Kuiper belt objects (KBOs), is thought to have undergone a giant impact that gave rise to Haumea's rapid rotation with a spin period of only 4 hours (Rabinowitz et al., 2006) and that created its multiple satellite system (Brown et al., 2005, 2006b) and collisional family (Brown et al., 2007). The family of KBOs (1995 SM_{55}, 1996 TO_{66}, 1999 OY_3, 2002 TX_{300}, 2003 OP_{32}, 2003 UZ_{117}, 2005 CB_{79}, 2005 RR_{43}) was linked to Haumea because its members display surface properties and orbits similar to those of Haumea. It has been proposed that this family of KBOs are collisional fragments of the ejected ice mantel of Haumea that were produced and ejected in Haumea's giant impact (Brown et al., 2007). However, the velocity dispersion between the family members is only ~ 140 m/s which is unusually small for fragments of disruptive impacts which should typically be ejected with a velocity comparable to the escape velocity (i.e., ~ 900 m/s for Haumea) (Benz & Asphaug, 1999; Nesvorný et al., 2006). In addition, simulations suggest that high velocity giant impacts lead to either the formation of a

disk of satellites or the dispersion of collisional fragments. The simultaneous creation of multiple satellites and the dispersion of collisional fragments has not been seen (Melosh & Ryan, 1997; Benz & Asphaug, 1999; Agnor & Asphaug, 2004; Canup, 2004, 2005); however, one should bear in mind that none of the simulations tried to specifically explain Haumea's giant impact.

In this chapter we propose and discuss a different formation scenario for the origin of Haumea's collisional family. In our scenario the family members are ejected while in orbit around Haumea. Ejecting the family members while in orbit around Haumea has the advantage that it naturally gives rise to a lower velocity dispersion among the family members than a direct ejection of fragments from Haumea's surface and, in addition, it aids in explaining Haumea's initial giant impact.

This paper is structured as follows. In §5.2 we introduce our definitions and assumptions. We give a detailed account of our model for the formation of Haumea's collisional family in §5.3. §5.4 is concerned with Haumea's giant impact. Discussion and conclusions follow in §5.5.

5.2 Definitions and Assumptions

The Haumea family currently consists of Haumea and eight additional KBOs. The family members have typically an eccentricity of ~ 0.12 and an inclination of $\sim 27°$. The actual masses of the family members are uncertain since Haumea is the only object in its family with a measured albedo. Haumea's visible albedo, with about 70% (Rabinowitz et al., 2006; Stansberry et al., 2008), is among the highest in the solar system. In addition, lower limits for the visible geometric albedo of family members 2002 TX_{300}, 1995 SM_{55} and 1996 TO_{66} were determined to be 19% (Ortiz et al., 2004; Grundy et al., 2005a), 6.7%, and 3.3% (Altenhoff et al., 2004; Grundy et al., 2005a), respectively. Given the common origin of the Haumea family and their similar surface characteristics with strong water ice absorption features it is likely that the family members have, like Haumea, high albedo surfaces (Rabinowitz et al., 2008). We will therefore assume that all family members have an albedo similar to

Table 5.1. Definition of Symbols

Symbol	Value	Definition
M	4.2×10^{24}g	mass of Haumea (Brown et al., 2005)
R	694km	mean radius of Haumea[a]
Ω_B	9.2×10^{-4}rad/s	angular break up velocity of Haumea
v_B	635m/s	break up velocity of Haumea
Ω	7.1×10^{-10}rad/s	angular velocity around the sun[b]
v_{disp}	3km/s	velocity dispersion in the scattered Kuiper belt
Σ	3×10^{-4}g/cm^2	Kuiper belt mass surface density of $\sim$ 100km sized bodies
m_s	$\sim 2 \times 10^{20} - 3 \times 10^{22}$g	mass range of Haumea's family member[c]

[a]for a density of 3g/cm^3 (Rabinowitz et al., 2006)

[b]evaluated at 43AU

[c]derived from magnitude difference between Haumea and the family members & assuming same albedo as Haumea and a density of 1g/cm^3, magnitudes are taken from Ragozzine & Brown (2007) and references within

that of Haumea and we calculate the masses of the family members from absolute magnitudes from Ragozzine & Brown (2007) and references within.

Estimates from current Kuiper Belt surveys yield for the mass surface density $\Sigma \sim 3 \times 10^{-4}$g cm^{-2} for KBOs of $\sim$ 100 km in size (Petit et al., 2008; Fuentes & Holman, 2008; Fraser et al., 2008; Trujillo & Brown, 2003; Trujillo et al., 2001). We use this value of Σ, assuming that no 100 km sized objects were lost from the Kuiper belt after it was dynamically excited. We use a power law distribution $N(r) \propto r^{1-q}$ with power-law index $q \sim 4$ (Bernstein et al., 2004; Fuentes et al., 2009; Fraser & Kavelaars, 2009) when estimating the number density of objects smaller than $\sim$ 100 km in this paper.

For simplicity, we define symbols and their numerical values that will be used throughout this paper in Table 5.2.

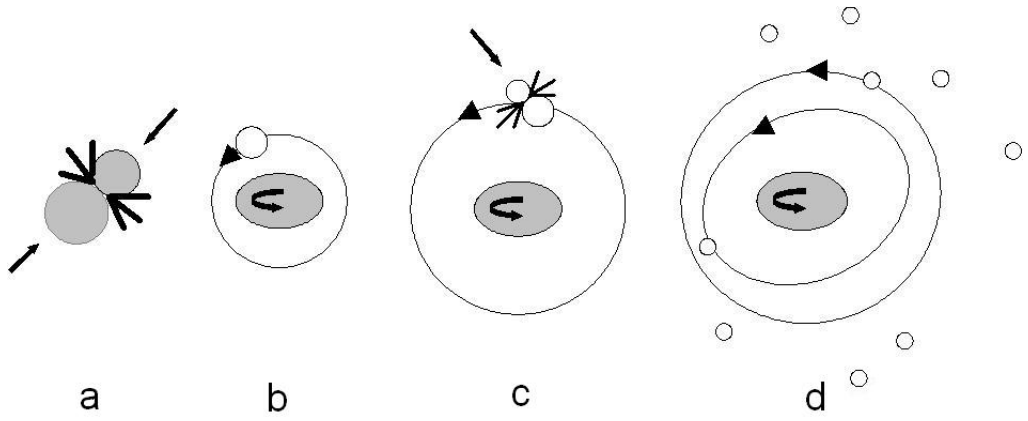

Figure 5.1 Cartoon of our model for the formation of Haumea's collisional family. From left to right; first, Haumea suffers a giant impact (a). This collision gives rise to Haumea's fast, 4 hour spin period and ejects material that accumulates into a tightly bound satellite around Haumea (b). The newly formed satellite undergoes tidal evolution that increases its orbital separation from Haumea. Haumea's satellite suffers a destructive collision with an unbound KBO (c). This collision creates and ejects the family and forms the two moons (d).

5.3 The Formation of Haumea's Collisional Family

5.3.1 Formation of a Single Satellite and Ejection by Destructive Satellite Collision

Our formation scenario for Haumea's collisional family can be divided into three steps. First, Haumea suffers a large collision. This collision gives rise to Haumea's fast, 4 hour spin period and ejects material that accumulates into a tightly bound satellite around Haumea. Second, the newly formed satellite undergoes tidal evolution that increases its orbital separation from Haumea. Third, the satellite suffers a destructive collision with an unbound KBO which creates and ejects the collisional family (see Fig. 5.1). In this case, the typical velocity dispersion of the family will be of the order of the escape velocity from the satellite which is $\sim 190\ m/s$ as will be shown below.

Starting with a tightly bound satellites around Haumea, the tidal evolution timescale for a satellite of mass, m_s, to evolve from an initial separation of a few times Haumea's

radius, R, to a separation $a \gg R$ is given by

$$\tau_{tidal} = \left(\frac{2}{39}\right)\left(\frac{Q}{k}\right)\left(\frac{M}{m_s}\right)\left[\frac{v_B}{v(a)}\right]^{13}\Omega_B^{-1}, \tag{5.1}$$

where $v(a)$ is the orbital velocity of the satellite with semi-major axis, a. Q is the tidal dissipation function and k the tidal Love number of Haumea. We refer the reader to Table 5.1 for the definitions of the remaining symbols.

The satellite suffers a destructive collision with unbound KBOs at a rate

$$\mathcal{R}_{coll} \sim \frac{\Sigma\Omega}{\rho r^3} r_s^2, \tag{5.2}$$

where r is the radius of the 'bullet' that can break up the satellite by collisions. The initial satellite needs to have been at least as large as all the identified family members combined (including Hi'iaka and Namaka but with the exclusion of Haumea) which yields a satellite radius of $\sim$ 260km. Bodies of this size are predominantly held together by their own gravity. We can estimate the bullet size needed for satellite-break-up by considering energy and momentum conservation of the shock that propagates from the impact point to the antipode of the target. Since energy and momentum conservation represent two limiting cases for impact processes (Holsapple, 1994); we estimate the range of bullet sizes needed for satellite-break-up to be

$$\left(\frac{G\rho r_s^5}{v_{disp}^2}\right)^{1/3} < r < \left(\frac{G\rho r_s^8}{v_{disp}^2}\right)^{1/6}, \tag{5.3}$$

where the lower limit is derived by requiring that the kinetic energy of the bullet be equal to the total gravitational energy of the target and the upper limit results from conservation of momentum. We refer the reader to Pan & Sari (2005) for a detailed derivation and discussion of these two destruction criteria for strengthless bodies. Evaluating equation (5.3) yields bullet sizes of 20 km $<$ r $<$ 70 km. Substituting expression (5.3) into equation (5.2) we find that the typical timescale for Haumea's satellite to suffer a destructive collision is 2 Gyr $< \tau_{\rm coll} <$ 80 Gyr. The timescale for

satellite-break-up by a collision and the consequent formation of the family ranges therefore from a few to tens of Gyrs. The actual τ_{coll} is most likely closer to tens of Gyrs since the majority of the binaries in the Kuiper belt should have been destroyed by collisions otherwise. This, therefore, implies a probability for a family forming event of $\sim 10\%$ over the age of the solar system. Estimates of the current Kuiper belt population indicate that there should be about 10 objects with radii as larger as Haumea (Trujillo et al., 2001; Bernstein et al., 2004; Fuentes et al., 2009; Fraser & Kavelaars, 2009). The abundance of Haumea-sized objects and the ubiquity of collisionally formed satellites around the largest KBOs (Brown et al., 2006a; Brown & Suer, 2007) makes our formation scenario consistent with having one collisional family in the Kuiper belt. The typical velocity dispersion between the family members that are produced in the satellite-break-up discussed above is of the order of the escape velocity of the initial satellite. For a satellite radius of ~ 260 km and a density of 1 g/cm^3 we have an escape velocity from the satellite, v_{esc}, of ~ 190 m/s. Simulations of disruptive impacts on ice and basalt targets find typical ejection velocities of $\sim 0.7 v_{esc}$ for the largest remnant and impact velocities of 3 km/s (Benz & Asphaug, 1999). It could therefore be that the actual velocity dispersion of the family from a disruptive impact is somewhat smaller than the ~ 190 m/s estimated here.

Finally one needs to compare the escape velocity from the satellite, v_{esc}, with its orbital velocity around Haumea, $v(a)$. A satellite-break-up only leads to ejection from the Haumea system, and therefore to the formation of a collisional family, if the tidal evolution has increased the orbital separation of the satellite such that $v_{esc} \gtrsim v(a)$. We need to estimate the tidal Love number, k, for Haumea in order to evaluate the orbital evolution timescale. We infer from Haumea's density of ~ 3 g/cm^3 that it must be mainly composed of rock. Using the rigidity of basalt rock, $\mu \sim 2 \times 10^{11}$ erg/cm^3 (Benz & Asphaug, 1999), we find $k = 1.5/(1 + \widetilde{\mu}) \sim 0.01$ where $\widetilde{\mu}$ is the effective rigidity given by $\widetilde{\mu} = 57\mu/(8\pi\rho^2 G R^2)$. Evaluating the tidal evolution timescale in equation (5.1) we find that the timescale for the semi-major axis to increase such that $v(a) \sim v_{esc}$ is $\sim 6(Q/100)(0.01/k)$ Myr. The satellite therefore has sufficient time to undergo tidal evolution that increases its semi-major axis such that $v_{esc} \gtrsim v(a)$ before

it suffers a destructive collision. Due to the long collision timescale, the satellite will most likely undergo tidal evolution for ~ 1 Gyr before it is broken apart. This yields a satellite separation from Haumea at the time of the satellite break up of ~ 17000 km.

Haumea's spin angular momentum provides an upper limit on the mass of the initial satellite that was later broken up into the family members. Assuming no angular momentum was added to the system after the giant impact and that Haumea was initially spinning close to break up, we find a maximum satellite orbital angular momentum of $\sim 4 \times 10^{36}$ g cm^2/s. For a destructive satellite collision at an orbital separation of ~ 17000 km this yields a satellite mass of $\sim 2 \times 10^{23}$ g. Our formation scenario, therefore, predicts that the total mass of all the family members combined should not exceed $\sim 1/20$ of the mass of Haumea or about 3 times the mass of the $R \sim 260$ km satellite considered in the calculation for the family forming event above.

In summary, we propose that Haumea suffered a giant impact that leads to the formation of a large, ~ 260 km radius, satellite. Tidal evolution increases the semi-major axis of the satellite such that $v_{esc} \gtrsim v(a)$ in $\sim 10^7$ years. The satellite suffers a destructive collision with an unbound KBO. This collision breaks the satellite into the different family members and ejects them from the Haumea system. This results in a typical velocity dispersion among the family members of ~ 190 m/s. We propose that Hi'iaka and Namaka are remnants of this collision that did not escape from the Haumea system. The destructive satellite collision that leads to the formation of the Haumea family has a collision timescale of several tens of Gyrs, which makes our formation scenario consistent with having one collisional family in the Kuiper belt.

5.3.2 Formation of Multiple Satellites and Ejection by Collisions with Unbound KBOs

One can imagine that Haumea's initial giant impact did not generate just one but several tightly bound satellites. The newly formed satellites undergo tidal evolution that increases their orbital separation from Haumea. Once the orbital separation is sufficiently large, the majority of the satellites become gravitationally unbound from

Haumea due to collisions with small, unbound KBOs. In this case, the typical velocity dispersion of the family will be of the order of the orbital velocity around Haumea before ejection which we show is ~ 120 m/s.

The rate at which a given satellite suffers collisions with unbound KBOs is given by equation (5.2). The satellite sizes and impactor size needed to eject a satellite by collision, however, differ from that required for satellite destruction in the previous section. In a given collision, the velocity change of the satellite is given by the conservation of linear momentum, $\Delta v(a) r_s^3 = \chi r^3 v_{disp}$. The coefficient χ accounts for the final momentum of the impactor. If the unbound KBO is perfectly reflected $\chi = 2$. Momentum loss from an impact crater can lead to $\chi > 2$ where the exact value of χ depends on the properties of the colliding bodies (Melosh et al., 1994). Since we are primarily concerned with deriving an order of magnitude estimate for the impactor size we will adopt $\chi = 1$ for the rest of this paper. A satellite of Haumea can be ejected by a collision with an unbound KBO if it suffers a velocity change $\Delta v(a) \sim v(a)$. Therefore, in order to be ejected, a satellite needs to collide with a KBO that typically has a radius of $r \sim r_s [v(a)/v_{disp}]^{1/3}$.

Substituting this expression for r into equation (5.2) we find that the ejection timescale for Haumea's satellites by a collision with an unbound KBO is given by

$$\tau_{coll} = \mathcal{R}_{coll}^{-1} \sim \frac{\rho r_s}{\Sigma} \left(\frac{v(a)}{v_{disp}} \right) \Omega^{-1}. \tag{5.4}$$

For the ejection of Haumea's satellites by collisions with unbound KBOs to be the typical outcome we need $\tau_{coll} \sim \tau_{tidal}$ since otherwise most of the satellites should have remained bound to Haumea which is contradicted by observations of the Haumea family. Equating the tidal evolution and ejection timescales allows us to derive the typical velocity with which the family members left the Haumea system. Equating equations (5.1) and (5.4) and solving for $v(a)$ we have

$$v(a) \sim v_B^{13/14} v_{disp}^{1/14} \left[\left(\frac{2}{39} \right) \left(\frac{Q}{k} \right) \left(\frac{M}{m_s} \right) \left(\frac{\Sigma}{\rho r_s} \right) \left(\frac{\Omega}{\Omega_B} \right) \right]^{1/14} \sim 120 \text{ m/s} \tag{5.5}$$

where we used $Q/k \sim 10^4$ and $m_s \sim 4.2 \times 10^{21}$ g (i.e., $M/m_s \sim 10^3$) to estimate $v(a)$. Evaluating equation (5.5) for the various masses of the family members we find that $v(a)$ ranges from 98 m/s to 178 m/s with a typical value of $\sim$ 120 m/s. Therefore, Haumea's satellites will be ejected from the Haumea system by collisions with unbound KBOs once their orbital velocity around Haumea is $\sim$ 120 m/s. This will also be, roughly, the expected velocity dispersion between family members which is in good agreement with the observations (Brown et al., 2007; Ragozzine & Brown, 2007).

Evaluating both the collisional and tidal evolution timescale using $v(a) \sim 120\, m/s$ we find from equations (5.4) and (5.1) that the typical ejection timescale is $\sim$ 60 Gyr. The ejection timescales for the various masses of the family members are all tens of Gyrs and therefore exceed the age of the solar system. Our calculation here can only estimate the ejection timescale to an order of magnitude, it might therefore be that the actual ejection timescale is somewhat shorter than estimated here. In addition, we might have underestimated the number of unbound KBOs that can lead to the ejection of family members, since we extrapolated the surface density of 100 km sized bodies to smaller sizes assuming a power-law index q of 4, whereas the actual power-law index might be a little larger than this. Since this second formation scenario for the Haumea family involves the ejection of all the family members separately the ejection process cannot be a rare event. The ejection timescales therefore need to be shorter than the age of the solar system for this formation scenario to be feasible. This however raises a different problem. If the ejection timescales are indeed shorter than the age of the solar system, then most of the binaries in the Kuiper belt should have been broken apart by the same process. This is in contradiction with the observations and we therefore conclude that formation of the Haumea family by a destructive collision of a single satellite is the preferred scenario.

In addition to problems discussed above, this second scenario faces yet another challenge. If the initial giant impact of Haumea produced several satellites then satellite-satellite interactions need to be taken into account. The timescale for satellite ejection due to satellite-satellite interactions is $\sim (M/m_s)^2 a/v(a)$ (Goldreich et al.,

2004b). This timescale is very short (i.e., $\sim 4\times10^3$ years for $M/m_s \sim 10^3$ and a 10-day satellite orbit). Initially, however, $v(a) > v_{esc}$, which implies that the satellites tend to collide with each other rather than eject each other from the system. Satellite-satellite collisions may either lead to accretion or break up. In either case it is questionable whether several satellites can survive and tidally evolve outwards such that they could be ejected by collisions with unbound KBOs. Satellite-satellite interactions are therfore yet another reason to favor our first scenario in which a single satellite is created and broken apart.

As an alternative to ejecting the satellites by collisions with unbound KBOs, one can imagine that the satellites could have been removed from the Haumea system by gravitational scattering of passing KBOs. However, in the high velocity regime discussed here ($v_{disp} > v_{esc}$), the rate of satellite ejection due the gravitational scattering is much less than that due to direct impacts of unbound KBOs onto the satellites. See Collins & Sari (2008) for comparison of collisional and gravitational evolution of binaries.

5.4 Haumea's Initial Giant Impact

Brown et al. (2007) estimate that Haumea's radius before its giant impact was $\sim$ 830 km and that the impactor was $\sim$ 500km in radius. The timescale for such an impact to occur in todays Kuiper belt can be found from equation (5.2) which yields a collision timescale of $\sim 8\times10^{12}$ years when evaluated for $R = 830$km and $r = 500$ km. Such a collision is therefore extremely unlikely but needed if one wants to form and eject the family directly from the giant impact. Levison et al. (2008) propose a giant impact scenario for Haumea that circumvents this low probability by requiring a collision between two scattered disk objects, assuming that the scattered disk was a 100 times more massive than it is today. In our formation scenario Haumea can suffer its giant impact before the Kuiper belt was dynamically excited, which shortens the collision timescale significantly. The timescale for Haumea's giant impact in the

sub-Hill velocity regime is (Goldreich et al., 2004b) (see also Chapter 3)

$$\tau_{coll} \sim \frac{\rho r^3}{\Sigma \Omega R^2} \alpha^{3/2} \sim 8 \times 10^6 \text{years} \tag{5.6}$$

where $\alpha = R/R_H \sim 10^{-4}$ and R_H is Haumea's Hill radius. Therefore, allowing Haumea's giant impact to occur while the Kuiper Belt was still dynamically cold decreases the giant impact timescale by 6 orders of magnitude, even without enhancing the mass surface density in the Kuiper Belt above its estimated current value. We therefore propose that Haumea's initial giant impact occurred while the velocity dispersion of large KBOs was still in the sub-Hill regime. This is supported by the ubiquity of small, collisionally formed satellites around KBOs, which have radii as large as 1000 km (Brown et al., 2006a; Brown & Suer, 2007) and the Pluto-Charon system (Weaver et al., 2006) which strongly suggests that sub-Hill KBO velocities prevailed during satellite formation and that collisional satellite formation was common, especially around the largest KBOs. The satellite, which we propose forms in Haumea's giant impact, is initially tightly bound to Haumea and the long tidal evolution timescale ensures that the Haumea-satellite system remains intact until after the dynamical excitation of the Kuiper belt. The family members are created and ejected from the Haumea system only after the dynamical excitation of the Kuiper belt which ensures the dynamical coherence of the family members. This scenario, therefore, does not face the potential challenge of removing 99% of the mass in the scattered disk without destroying the dynamical coherence of the family.

5.5 Discussion and Conclusions

We propose a new formation scenario for the Haumea family. In our scenario Haumea's giant impact forms a single moon that tidally evolves outward until it suffers a destructive collision from which the family is created. The advantage of this scenario is that it naturally gives rise to a lower velocity dispersion among the family members than expected from direct ejection from Haumea's surface. We show that this forma-

tion scenario yields a velocity dispersion of $\sim$ 190 m/s among the family members. This is in good agreement with the measured dispersion $\sim$ 140 m/s in semi-major axis, eccentricity, and inclination of the family members (Brown et al., 2007; Ragozzine & Brown, 2007), which is a lower limit to the actual velocity dispersion since the orbital angles were chosen to minimize the velocity dispersion of the family (Ragozzine & Brown, 2007). Our formation scenario yields about one collisional family for Haumea-sized objects in the Kuiper Belt. Ejecting the family members from Haumea's orbit has the additional advantage that it is easy to reconcile with Haumea's initial giant impact. The family must have been ejected from Haumea after the Kuiper belt was dynamically excited in order to preserve the dynamical coherence of the family. If the family members are dispersed fragments of the giant impact itself, then the giant impact must have occurred after the Kuiper belt was dynamically excited. Such a giant impact occurs with a probably of less than 10^{-3} over the age of the solar system and is therefore extremely unlikely in todays Kuiper belt. Levison et al. (2008) suggest that Haumea's giant impact could be the result of collision between two scattered disk objects during a phase when the scattered disk was a 100 times more massive than it is today. In our scenario, Haumea's giant impact can occur before the dynamical excitation of the Kuiper Belt since the giant impact and the ejection of the family are two different events separated in time by at least $\sim 10^7$ years. The timescale for Haumea's giant impact in the sub-Hill velocity regime is $\sim 8 \times 10^6$ years. Observations show that the majority of the largest KBOs have small, collisionally formed satellites (Brown et al., 2006a; Brown & Suer, 2007). Giant impacts that lead to satellite formation around large Kuiper Belt objects were therefore common in the history of the Kuiper Belt and we propose that Haumea's initial giant impact was one of them. Our formation scenario is also in agreement with results from simulations of giant impacts since it only requires the formation of a satellite and not the simultaneous formation of satellites and direct ejection of fragments in a single collision (Melosh & Ryan, 1997; Benz & Asphaug, 1999; Agnor & Asphaug, 2004; Canup, 2004, 2005) which is required in the original formation scenario proposed by Brown et al. (2007).

In addition to the family members discussed above, Haumea has also two satellites.

Hi'iaka the larger outer satellite ($M/m_s \sim 200$) has a semi-major axis of 49500 km and a free eccentricity of 0.07 (Brown et al., 2005; Ragozzine & Brown, 2009). Namaka, the smaller ($M/m_s \sim 2000$) inner satellite, has a semi-major axis of 25700 km, a free eccentricity of 0.21 and its inclination with respect to Hi'iaka is 13° (Ragozzine & Brown, 2009). Hi'iaka and Namaka display, just like all other family members, strong water ice absorption features in their infrared spectra (Barkume et al., 2006; Fraser & Brown, 2009). Since this spectral signature seems to be only present among the family members it seems unlikely that Hi'iaka and Namaka were captured; instead they most likely formed together with the other family members. It is unlikely that Hi'iaka and Namaka evolved to their current separation by tides, since the tidal evolution timescales are excessively long. From equation (5.1) we have for Hi'iaka $\tau_{tidal} \sim 4 \times 10^{12}$ years and for Namaka $\tau_{tidal} \sim 6 \times 10^{11}$ years where we used again $Q \sim 100$ and $k \sim 0.01$. Both timescales exceed the age of the solar system by more than two orders of magnitude. We suggest that Hi'iaka and Namaka were produced in the same satellite-break-up that created the other family members, only that in their case the impulse was not sufficient to escape Haumea but instead it increased their semi-major axis by a factor of ~ 2 to their current separation. Such a collision will however also raise the eccentricity to order unity. Is is possible that the satellites, especially Hi'iaka, formed by re-accumulation of collisional fragments of the satellite break up. Such a re-accumulation scenario typically leads to more circular satellite orbits. We also note that Hi'iaka's free eccentricity of 0.07 is consistent with dynamical excitations by passing KBOs (Collins & Sari, 2008). Namaka, which is ten times less massive than Hi'iaka, could be a single collisional fragment of the satellite break up, hence its large free eccentricity of 0.21. We therefore find that our formation scenario for Haumea's family can account for the large semi-major axis and modest eccentricities of Hi'iaka and Namaka. The 13° mutual inclination between the two moons remains somewhat of a puzzle, since it is surprisingly low if the moons formed from fragments of a disruptive satellite collision as suggested in this paper.

Acknowledgments We would like to thank Darin Ragozzine for valuable discussions.

Chapter 6

Measuring the Kuiper Belt Size Distribution by Serendipitous Stellar Occultations

The measurement of the size distribution of small Kuiper Belt objects (KBOs) is a powerful tool to learn about the formation of KBOs, their effective strength and their collisional evolution. However, objects smaller than about 10 km in radius are too faint to be directly observed. They can, however, be detected indirectly by serendipitous stellar occultations. For the past 14 years, the HST/Fine Guidance Sensors (FGSs) have been collecting a large number of photometric measurements of stars with 40 Hz time resolution. Our FGS survey is about two orders of magnitude more powerful than any ongoing visible-light search for KBO occultations, and we expect to find between 0.3 to 52 events in the entire data set. We present here our analyses and preliminary results spanning 3 years of archival FGS data, which corresponds to ∼21% of our entire survey. These 3 years of FGS data consist of $\sim$ 7900 star hours of low ecliptic latitude ($-20 < i < +20$ deg) observations. The mean and median of the photon counts of our data in a 1/40 second interval are $\sim$ 700 and $\sim$ 340, respectively, and the noise is typically 4% larger than Poisson noise. We present our first candidate occultation event and show that we cannot attribute it to instrumental artifacts. Its probability of being a false positive due to statistical fluctuations in the data is only $\sim$ 0.4% and we conclude that it is likely that the candidate event is a real occultation. We constrain the surface density of KBOs with

radii larger than 350m to $< 4.9 \times 10^7$ deg^{-2} at the 95% confidence level. This is the best constraint to date and improves the previous best estimate for the KBO surface density by an order of magnitude. We rule out a power-law index of $q > 3.9$ for the differential size distribution of sub-km sized KBOs at the 95% confidence level. Our findings confirm that the size distribution of sub-km sized KBOs is shallower than that of large KBOs (i.e., $r > 50$ km) and is consistent with the idea that small KBOs underwent collisional evolution that modified their size distribution.

6.1 Introduction

Since the discovery of the first Kuiper Belt object (KBO) in 1992 (Jewitt et al., 1992) more than a 1000 objects have been detected. Large KBOs (radius $r \gtrsim 10$ km) can be detected directly, since they reflect sufficient sunlight. The size distribution of objects larger than ~ 50 km in radius is well described by a single power-law cumulative size distribution that is parameterized by $N(r) \propto r^{1-q}$, where $N(r)$ is the number of objects with radii greater than r, and q is the power-law index. Observations find that the power-law index for large KBOs is $q \sim 4.5$ (Fuentes & Holman, 2008; Fraser et al., 2008). The size distribution of large KBOs is a signature of their growth history.

Strong evidence from observations and theory suggests the existence of a break in the power-law size distribution at smaller KBO sizes (Bernstein et al., 2004; Fuentes & Holman, 2008; Fraser et al., 2008). The break in the size distribution is generally attributed to collisions that break-up small KBOs (radius $r \lesssim 10$ km) and that modify their size distribution. If this is so, then the location of the break (i.e., the break radius) constrains the time period over which destructive collisions have been occurring in the Kuiper Belt. With time, collisions move the break radius to ever larger sizes. Furthermore, the power-law index below the break radius constraints the material properties of the KBOs. Small KBOs that are in collisional equilibrium and that are held together predominantly by material strength have a size distribution with power-law index $q \sim 3.5$, which is the so-called Dohnanyi spectrum (Dohnanyi, 1969). The size distribution is shallower with a power-law index of $q \sim 3$ if small

KBOs are held together predominantly by gravity (i.e., they are effectively rubble piles) (Pan & Sari, 2005). The break radius and the power-law index below the break, therefore, constrain the collisional history of the Kuiper Belt and reveal the material properties of small KBOs, respectively. However, the slope of the power-law distribution below the break, as well as the exact point of the power-law break, are still uncertain observationally (e.g., Trujillo et al., 2001; Bernstein et al., 2004; Fuentes & Holman, 2008; Fraser et al., 2008) and theoretically (e.g., Davis & Farinella, 1997; Stern & Colwell, 1997; Kenyon & Luu, 1999; Pan & Sari, 2005). Observational work by Fuentes & Holman (2008) and Fraser et al. (2008) locate the break at KBO radii between 25 to 50km. The albedo of KBOs, which has only been measured for a handful of ~ 100 km-sized objects (Grundy et al., 2005b), displays remarkable diversity and remains a major uncertainty when converting the observed KBO magnitudes into sizes. There are no reliable measurements of the abundance of KBOs smaller than about 10 km in radius, since objects of this size are too faint to be detected directly. They can, however, be detected indirectly by stellar occultations (e.g., Bailey, 1976; Dyson, 1992; Axelrod et al., 1992). A small KBO passing through the line of sight to a star will partially obscure the light from the star, which, under suitable circumstances, can be detected in the stellar light curve. For visible light, the Fresnel scale is given by $(\lambda a/2)^{1/2} \sim 1.3$ km, where $a \sim 40$ AU is the distance to the KBO and $\lambda \sim 600$ nm is the wavelength at which the observations are being conducted. Since the sizes of KBOs of interest are comparable to the Fresnel scale, diffraction effects cannot be neglected. The diffraction pattern is determined by the size and shape of the KBO, the angular size of star, the wavelength range of the observations and the impact parameter between the star and the KBO. The duration of the occultation is approximately given by the ratio of the Fresnel scale to the relative velocity between the observer and the KBO, and only lasts a fraction of a second. A fast sampling frequency is therefore key in order to search for serendipitous stellar occultations caused by objects in the Kuiper Belt.

Both optical (Roques et al., 2006; Zhang et al., 2008; Bickerton et al., 2008; Bianco et al., 2009) and X-ray (Chang et al., 2006) occultation searches have been

conducted to probe the population in the Kuiper Belt. The technical parameters for the various surveys are listed in Table 6.1. Chang et al. (2006) searched for occultation signatures in the archival RXTE X-ray data of Scorpius-X1 and reported a surprisingly high event rate. However, Jones et al. (2008) showed that most of the dips in the Scorpius-X1 light curves are artificial effects caused by the RXTE photomultiplier (PMT). Only 12 of the original 58 events were not ruled out as artifacts; however Bickerton et al. (2008) point out that the duration and/or depth of most of the 12 remaining events are inconsistent with the diffraction signature of occultation events. Roques et al. (2006) and Bickerton et al. (2008) both conducted occultation surveys in the optical regime. Neither survey reported any detections of objects in the Kuiper Belt, which is not surprising given the low expected event rate of both surveys. Ground-based observations may suffer from a high rate of false positives due to atmospheric scintillation and birds. The only ground-based system that is currently able to screen events caused by atmospheric scintillation and other kinds of interference is the TAOS (Taiwanese American Occultation Survey), which consists of four telescopes that observe the same position simultaneously (e.g., Alcock et al., 2003; Lehner et al., 2006). TAOS collected over 150,000 star hours with 5 Hz sampling frequency and reported no detections so far. The strongest upper limit to date on the surface density of sub-km sized KBOs has been reported by Bianco et al. (2009), who constrain the surface density of KBOs with radii larger than 350 m to be less than 4.8×10^8 deg^{-2}.

For the past 14 years, HST's Fine Guidance Sensors (FGS) have been collecting a large number of photometric measurements of stars with 40 Hz time resolution. The following sections describe our occultation survey that consists of searching for serendipitous stellar occultations in archival HST/FGS data. Our survey is about two orders of magnitude more powerful than any ongoing visible-light search for stellar occultations (see Table 6.1).

This chapter is structured as follows. We describe our HST/FGS survey and the data we received so far in §6.2 and §6.3, respectively. Details about our search algorithm and detection efficiency follow in §6.4. In §6.5 we present our preliminary

Table 6.1. Our FGS survey compared to previous work

Δt/days[a]	Sampling/Hz	r_{min}/km[b]	N_{det}[c]	Power[d]	Reference
~ 1500	40	0.25		1	our HST/FGS survey
0.63	20	0.2	1?	8×10^{-4}	Roques et al. (2003)
1.4	46	0.2	3?	2×10^{-3}	Roques et al. (2006)
0.40	40	0.43	0	5×10^{-5}	Bickerton et al. (2008)
~ 6400	5	2	0	8×10^{-3}	TAOS/Zhang et al. (2008)
9.2	200	0.2	0	1×10^{-2}	Bianco et al. (2009)
6.5	2000	0.06	0-10?	0.17	RXTE/Chang et al. (2006)

[a]Δt is the total number star days of observations at low ecliptic latitude in each survey

[b]r_{min} is the minimum radius of a KBO that can be detected with a detection efficiency of 10%

[c]N_{det} is the number of detections originally claimed, note that none of these detections is validated by the latest analyses (Bickerton et al., 2008; Jones et al., 2008; Blocker et al., 2009)

[d]Power is the number of expected detections normalized to our HST/FGS survey (= 1). The power of each survey was calculated assuming $q = 4$. In this case, the number of expected events is $\propto \Delta t r_{min}^{-3}$.

results. Conclusions and future work follow in §6.6.

6.2 HST/FGS Survey

The FGSs are an integral part of the HST pointing control system. The three FGSs ensure a pointing stability of HST at the milli-arc-second level over exposure times of tens of minutes. Each FGS is a dual-axis white light shearing interferometer and the photon count of each FGS is recoded by 4 PMTs. The interferometer consists of a polarizing beam splitter followed by two Koesters prisms. The incoming unpolarized light is split in two orthogonal plane-polarized beams. Each beam with roughly half the initial intensity transverses a Koesters prism and its associated optics, and is recorded at the two PMTs. Due to this instrumental design, the photon counts recorded in PMTs 1 and 2 are correlated with each other and similarly there exists a correlation between the photon counts of PMT 3 and 4 (see Fig. 6.1). The combined photon counts of PMT 1 and 2 are not correlated with the combined photon counts of PMT 3 and 4. Figure 6.1 illustrates the light path through the Koesters prism to the PMTs.

In addition to ensuring the pointing stability of HST, the FGSs have been used

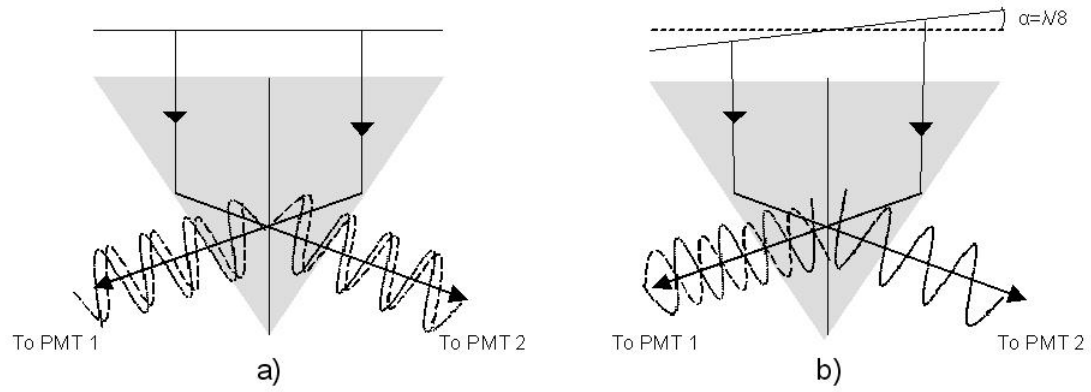

Figure 6.1 The Koesters prisms are divided by a dielectric beam splitter, which divides the incoming bean into two equal intensity beams, reflecting half and transmitting the other half with a 90 degree phase lag. The beam reflected from one side of the prism interferes constructively or destructively with the beam transmitted from the other side due to the division and phase shift imparted by the beam splitter. The degree of interference between the two beams is related to the angle between the direction of incoming wavefront and the plane of the dielectric beam splitter's surface (see cases a) and b) in this figure for comparison).

as science instruments. For example, the FGS was used to measure the parallaxes of cataclysmic variables and nova stars (McArthur et al., 2001; Harrison et al., 2000), to search for astrometric signatures of planets orbiting nearby stars (Benedict et al., 1999), and to obtain high-precision transient light curves of extra solar planets (e.g., Bean et al., 2008). For over a decade, the three FGSs have been collecting a large number of photometric measurements of the guide stars with 40 Hz time resolution. We analyze this archival data set with the aim to detect small KBOs and to measure their size distribution. The entire data set consists of $\sim 110,000$ star hours with a signal-to-noise ratio of $10 \lesssim S/N \lesssim 100$. Nominal HST operation uses two FGSs for guiding, with each FGS observing its own guide star. We are therefore able to remove false positives due to instrumental effects and, for example, day/night-time variations due to HST's orbit around the Earth. Figure 6.2 shows the HST integration time as a function of ecliptic latitude. About 34% of the observations are taken in the low ecliptic latitude region (i.e., -20 deg $<$ i $<$ $+20$ deg) of the Kuiper Belt. The remaining high-ecliptic latitude observations provide an excellent control sample

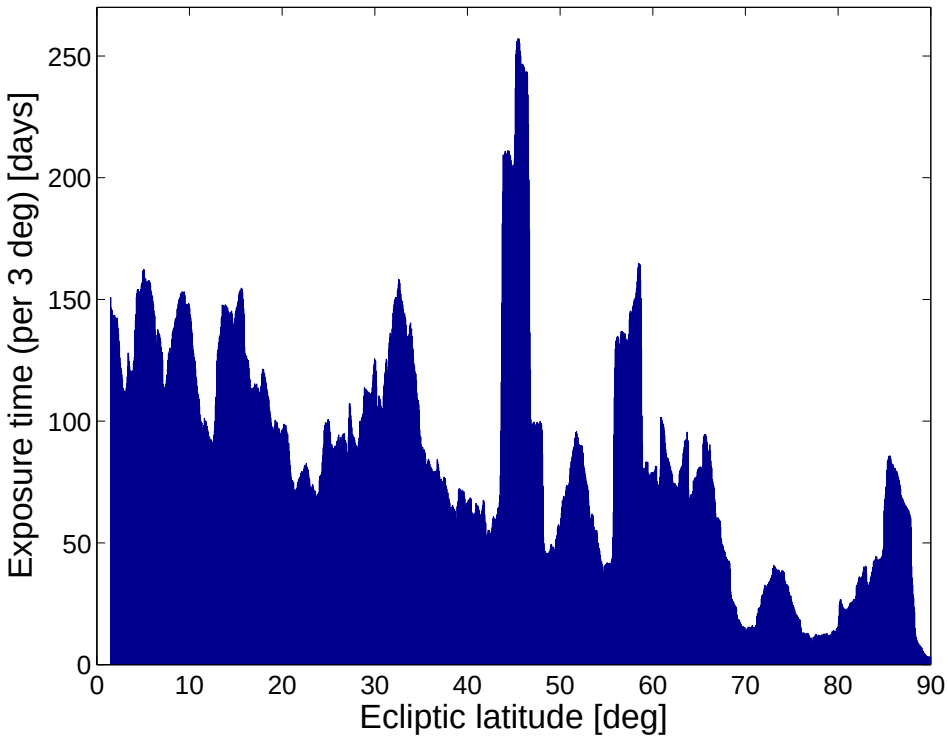

Figure 6.2 The total HST integration time, from cycle 1 to cycle 15, as a function of ecliptic latitude. The total integration time within 3, 6, and 20 deg of the ecliptic is 151, 305, and 884 days, respectively. High-ecliptic latitude observations provide an excellent control sample to test the rate of possible false positive detections.

which we use to test for possible false positive detections.

Figure 6.3 shows the distribution of angular sizes of the HST guide stars in units of the Fresnel scale at 40 AU and for observations at a wavelength of 600 nm. The vast majority of the HST guide stars have angular sizes less than the Fresnel scale. This is very important, since only stars with angular sizes less than the Fresnel scale will give rise to a diffraction pattern when occulted by a KBO.

6.3 Data

Currently, the FGS archival data is stored on limited access media at GSFC and must first be extracted. This task is carried out by Mike Wenz at STScI/GSFC. Technically, this includes the extraction of the FGS photometry streams from the files archived at GSFC, screening the data to retain only measurements taken in fine-

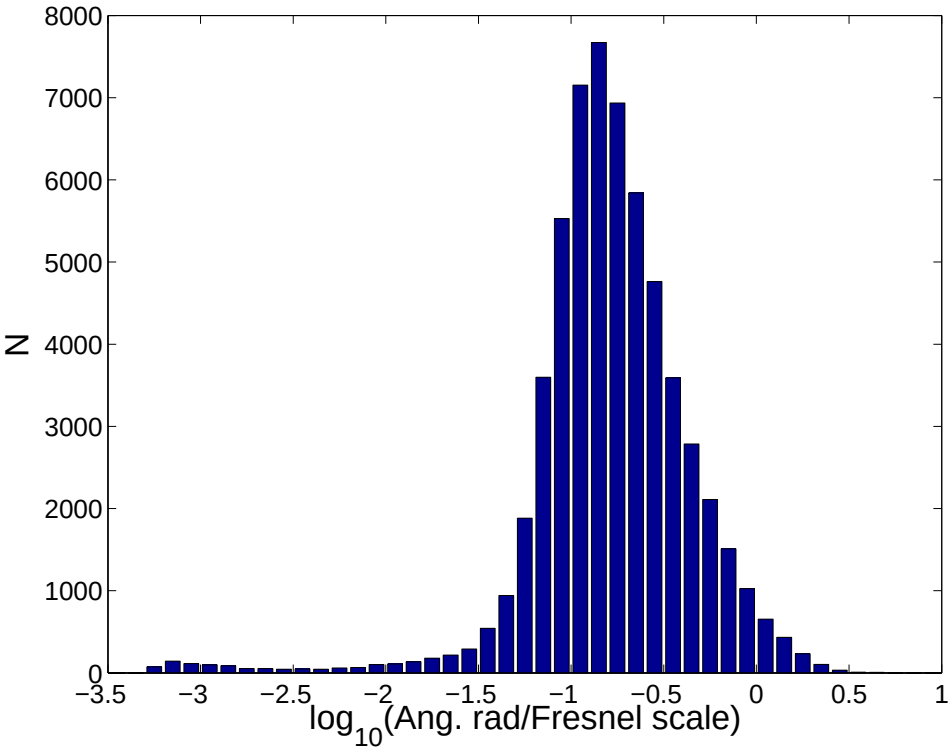

Figure 6.3 Distribution of angular sizes of HST guide stars, in units of the Fresnel scale, which is ~ 1 km for visible wavelengths at the distance of the Kuiper Belt. The angular sizes of the stars are calculated by using the star's apparent magnitude and $B - R$ colors to calculate their blackbody effective temperature.

lock mode and assigning a time-stamp and HST velocity to each photometry stream, as well as the coordinates and magnitudes of the guide star observed. As part of this work, we are constructing an easy-to-access archive of the FGS observations, which we intend to make available to the entire astronomical community. To date, we have been able to access and analyze a little over 3 years of FGS data. Figure 6.4 displays the estimated stellar magnitudes form the HST guide star catalog as a function of the photon counts recorded by the FGSs. The photon counts span more than two orders of magnitude from about 100 to 10,000. Figure 6.4 shows that the response of the PMTs is linear over the entire magnitude range of the FGS guide star observations.

The mean and median of the photon counts are ~ 700 and ~ 340, respectively, and the noise is typically 3 to 5% larger than Poisson noise. The photon count distribution of a 13 magnitude star is shown in Figure 6.5. Although we can currently not pinpoint the source of the excess noise above the Poisson noise limit, we know that the noise is not correlated. In a handful of cases we did detect some correlated noise but it could always be clearly attributed to instrumental artifacts, i.e., a slower read-out mode (see Fig. 6.6) or an abrupt change in the mean photon count.

6.4 Event Detection and Detection Efficiency

6.4.1 Detecting Events in Photometric Time Series

The 40 Hz time resolution allows for the detection of the actual diffraction pattern rather than a simple decrease in the photon count. Our detection algorithm therefore employs a template search using theoretical light curves and performs chi-square fitting of the templates to the data. This template fitting procedure improves the sensitivity of the survey compared to algorithms that search only for dips in the light curve and aids with the identification of false positives.

In general, the shape of the diffraction pattern is determined by the size of the KBO, the angular size of the star, the wavelength range of the observations and the impact parameter between the star and the KBO. A large fraction of HST guide

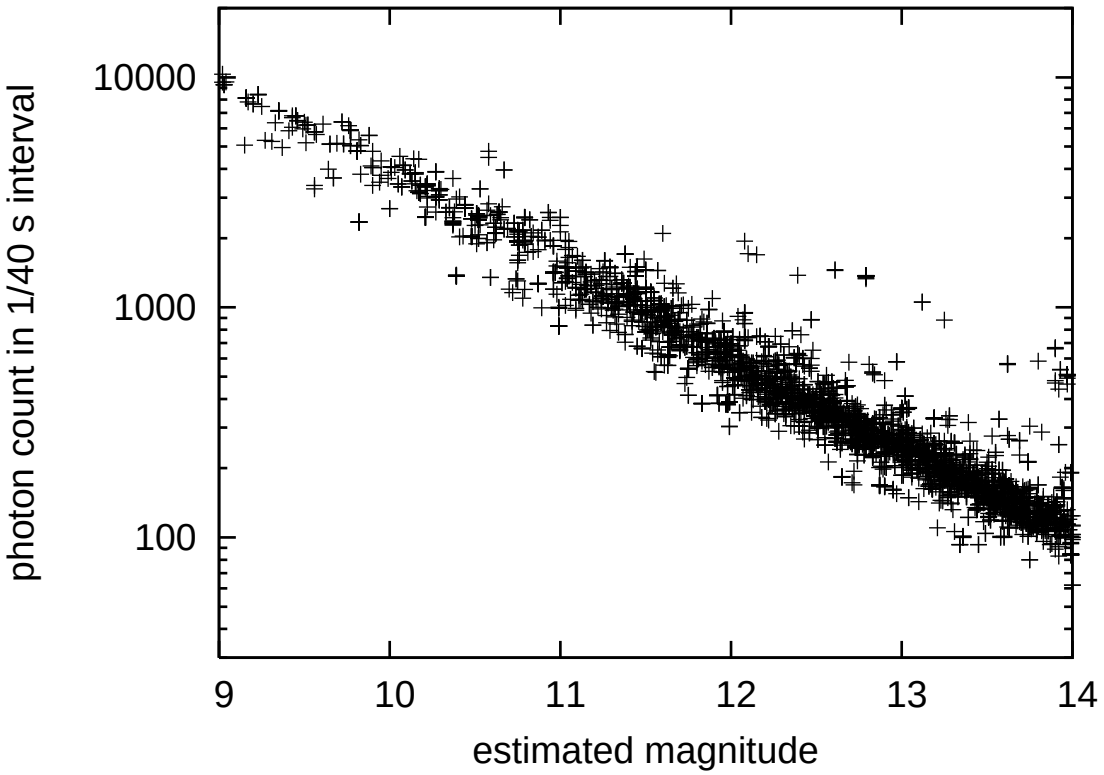

Figure 6.4 Photon count in 1/40 second interval as a function of the guide star's estimated magnitude of the FGS data obtained in 2007. The estimated magnitudes of the guide stars were obtained by feeding the magnitudes from the guide star catalog 1 and 2 into a transformation equation to convert them to FGS magnitudes. Since the FGSs are not looking through any filters at the star the color response of the PMT over the entire spectrum has to be taken into account. The predicted guide star magnitudes are therefore only rough estimates with a typical error of $+/-0.4$ magnitudes (private communication Mike Wenz). Some of the outliers that show a photon count significantly in excess of the remaining guide star population might be due to observations that were obtained without the pupil stop, which results in a higher photon count.

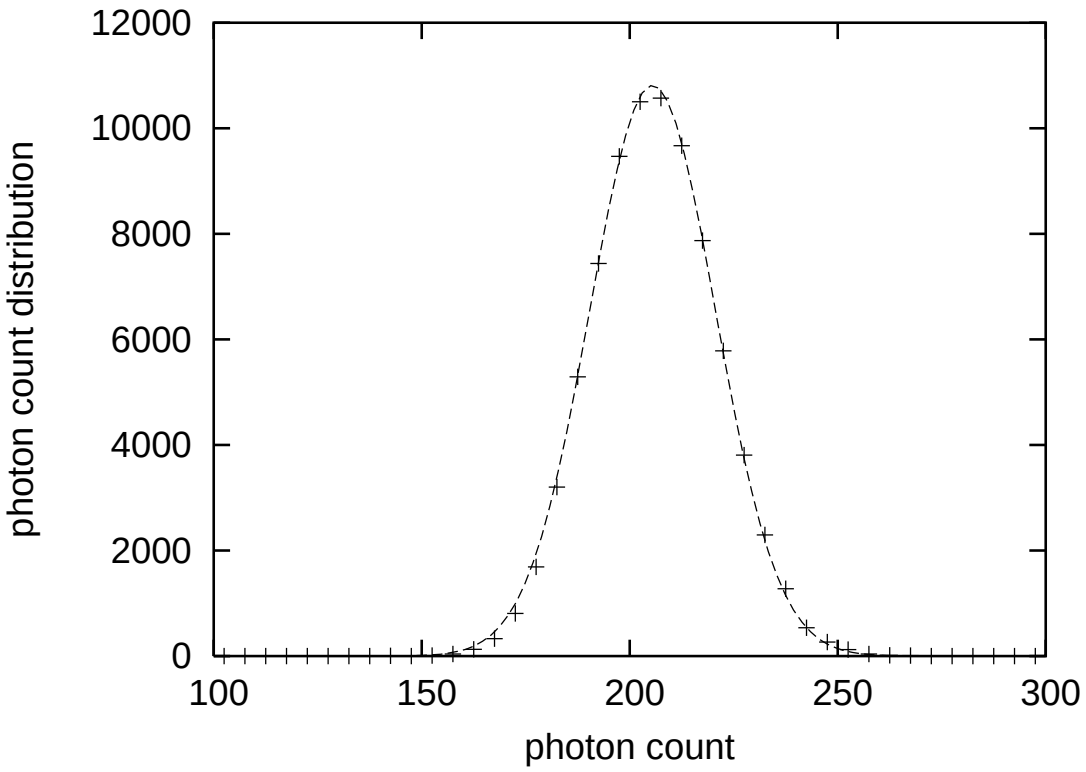

Figure 6.5 Typical photon count distribution of a 13 magnitude star from our FGS sample. The photon count distribution is described well by a normal distribution (dashed line) with a standard deviation that is 5% larger than Poisson noise.

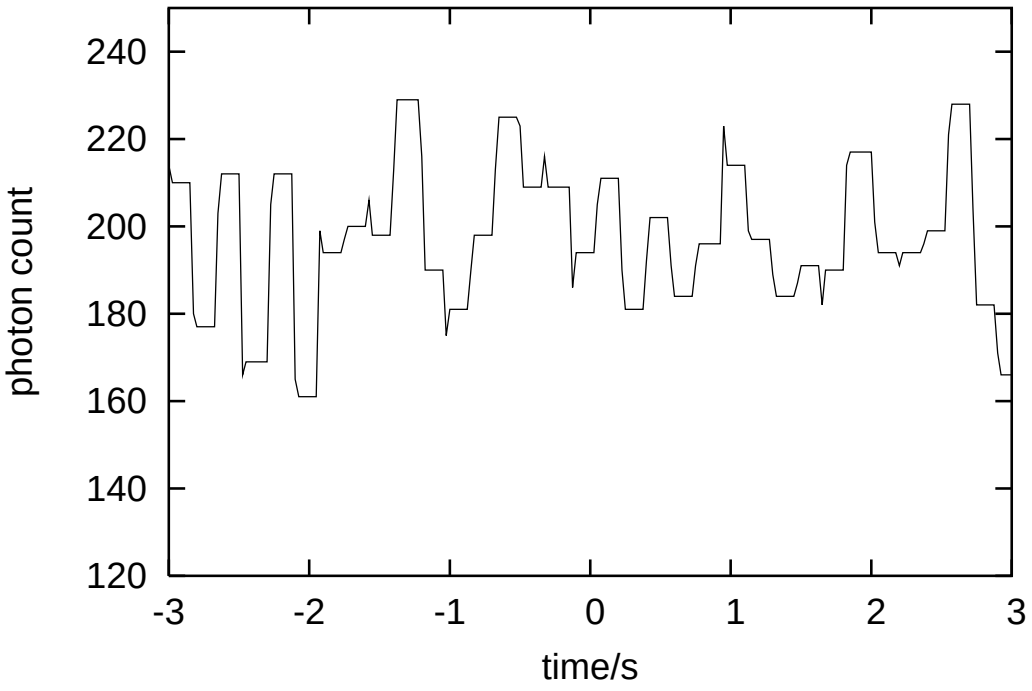

Figure 6.6 Photon count as a function of time for a photometric series that was sampled at a lower frequency.

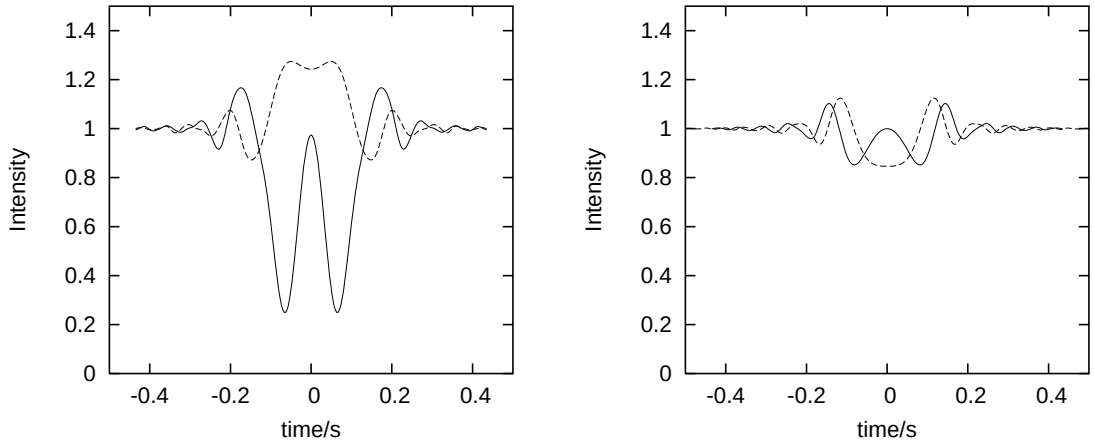

Figure 6.7 Two example light curves that are produced by a 300 m KBO and 1000 m KBO occulting a background star integrated over a wavelength range from 400-700 nm and for zero impact parameter (solid line) and an impact parameter of 1 Fresnel scale (1.3 km; dashed line). The relative velocity between HST and the KBO was assumed to be 15 km/s. In the Fraunhofer regime (300 m object, right panel) the shape of the light curve is solely determined by the impact parameter. The size of the KBO sets the amplitude of the diffraction pattern.

stars have angular sizes below the Fresnel scale (see Fig. 6.3) and, therefore, we treat them as point sources. The diffraction pattern is wavelength dependent. As a result, the observed diffraction pattern is generated by a superposition of single-wavelength diffraction patterns. The light curve templates that we use in our detection algorithm are integrated over a wavelength range of the FGS observations which corresponds to 400-700 nm. Occultations by objects less than the Fresnel scale (i.e., < 1.3 km in size) are in the Fraunhofer regime. As a result the diffraction pattern is not sensitive to the object shape. Furthermore, in the Fraunhofer regime the shape of the diffraction pattern is solely determined by the impact parameter, and the amplitude of the diffraction pattern is proportional to the surface area of the KBO (see Fig. 6.7). This significantly reduces the number of templates that need to be implemented in the search algorithm.

The duration of a given occultation event is independent of the object size, and is determined by the relative velocity between HST and the KBO and is known from the geometry of the observation (see Fig. 6.8). We compare the expected event

duration with the duration of candidate occultation events, and use this method to reject false positives. We analyze all the FGS data, without differentiating between observations at high and low ecliptic latitudes, and use high ecliptic latitude guide stars as a control sample. The angular size of the guide star, in addition to the ecliptic latitude, offers a way to reject false positives, since only stars with angular sizes less than the Fresnel scale will give rise to a diffraction pattern when occulted by a KBO. This latter test is, however, not very powerful in rejecting false positives since most guide stars have angular sizes less than the Fresnel scale. Finally, since nominal HST operation employs two FGSs for guiding simultaneously, false positives due to instrumental effects and, for example, day/night-time variations due to HST's orbit around the Earth can be identified and removed.

6.4.2 Detection Threshold

We perform a template search with theoretical light curves and use a χ^2 fitting procedure to identify candidate events. The significance of candidate events can be measured by their $\Delta\chi^2$ which is defined here as the difference between the χ^2 calculated for a fit to a constant, which corresponds to no event, and the χ^2 of the best fit template. Candidate events have large $\Delta\chi^2$, since they are poorly fit by a constant. We use the actual FGS data together with a bootstrap method to determine the detection threshold for our search algorithm. Figure 6.9 displays the number of false events as a function of $\Delta\chi^2$ flagged by our search algorithm in the FGS data after the time sequence of the data was randomly re-arranged using a bootstrap method. The events were flagged using exactly the same search algorithm that is used to analyze the FGS data. Choosing a threshold of less than one false positive detection over the entire FGS data set corresponds to a significance level of $\Delta\chi^2 > 63.1$ (see Fig. 6.9). In addition, we compare the velocity derived from the best fit of the false events with the velocity calculated from the geometry of the observations (see Fig. 6.8). There is a 20% probability that the two velocities agree within ± 4 km/s by chance. Hence, the number of false events that could be mistaken for a real event once the velocity

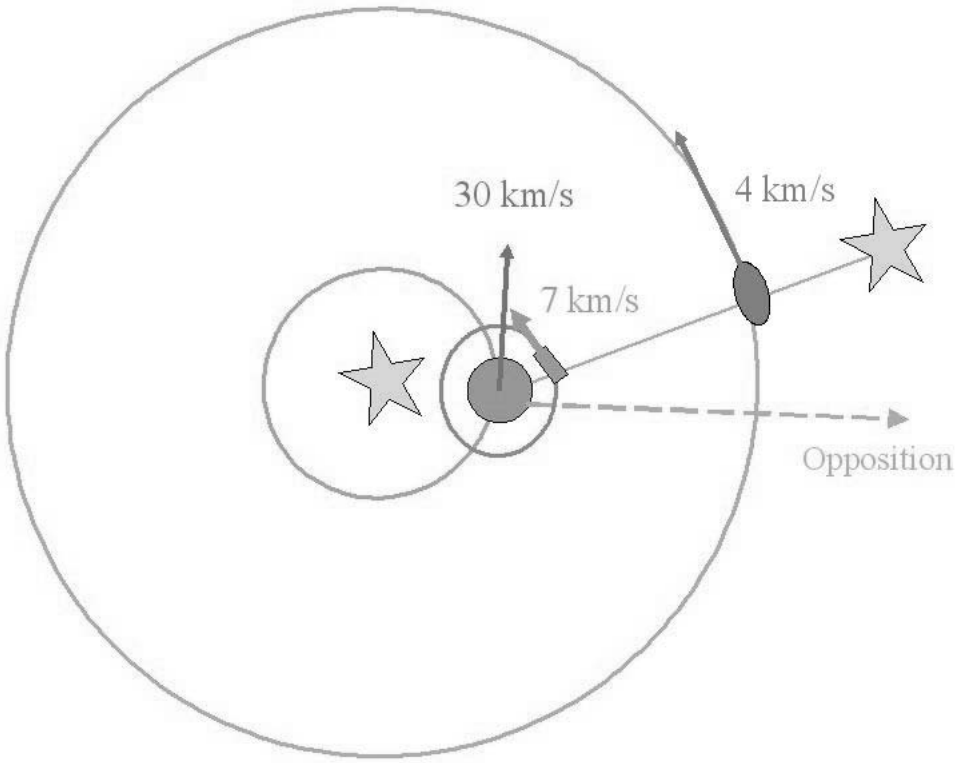

Figure 6.8 Diagram showing the different velocity components that determine the relative velocity between HST and the KBO. The velocity components of HST, the Earth and the KBO, assuming it is on a circular orbit, are known from the time and geometry of the observations. The relative velocity between the KBO and HST and hence the expected duration of the occultation event are therefore known and can be compared with the event duration of candidate events detected in the FGS data.

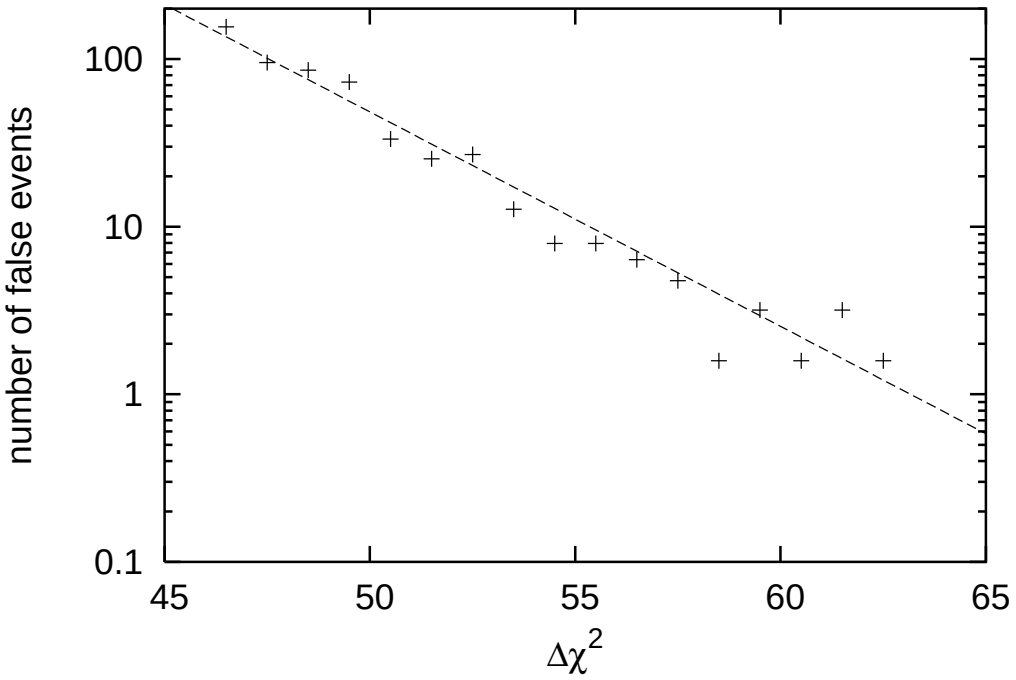

Figure 6.9 Number of false events as a function of $\Delta\chi^2$ and the line of best fit. The events were obtained from $\sim$ 66000 hours of FGS data which had its time sequence randomly re-arranged using a bootstrap method. The number of events was scaled to 110000 star hours which corresponds to the entire FGS survey. Since all the events represented in this figure are false positives a significance level of $\Delta\chi^2 > 63.1$ needs to be adopted to ensure less than one false positive detection over the entire FGS data set. The number of false events is reduced by a factor 5 compared to the number in Figure 6.9 once the velocity information is accounted for.

information is accounted for is 5 times less than the number of false events shown in Figure 6.9.

6.4.3 Detection Efficiency

Our ability to detect an occultation event of a given size KBO depends on the impact parameter of the KBO, the duration of the event and the signal-to-noise ratio of the data. An efficiency calculation is therefore necessary to determine the detection sensitivity of our survey and analysis. We implanted synthetic events into the observed photometric time series by convolving the actual FGS data with theoretical light

curves of KBO occultation events keeping the original noise. We implanted synthetic events corresponding to KBO sizes ranging from 130 m $<$ r $<$ 650 m and impact parameters from 0 to 4 Fresnel scales. A large fraction of the FGS observations are taken close to opposition. At opposition, the relative velocity between the Earth (+30 km/s) and the KBO (about −4 km/s, assuming a prograde zero-inclination orbit) is 26 km/s but the HST velocity component, which ranges from −7 km/s to +7 km/s, still needs to be added to obtain the actual relative velocity of the observations. For the purpose of determining the detection efficiency a relative velocity of 26 km/s was chosen, which corresponds to an occultation duration of ∼(2 Fresnel scales)/(relative velocity)∼ 0.1 s. The modified light curves were analyzed using the same search algorithm that is used to analyze the FGS data with the same significance threshold of $\Delta\chi^2 > 63.1$. The recovered events and their parameters were then used to determine the detection efficiency of our survey and to calculate the number of expected occultations. Figure 6.10 shows the detection efficiency as a function of KBO size. The detection efficiency is normalized by an impact parameter equal to 1 Fresnel scale, i.e., a detection efficiency of 1 means that all implanted events with impact parameters less than 1 Fresnel scale were successfully recovered; a detection efficiency of more than 1 means that in addition some events with impact parameters larger than 1 Fresnel scale were recovered. The detection efficiency of our survey is $\sim$ 10% for objects with r = 250 m. It exceeds 100% for KBOs with $r >$ 500 m. This means that objects larger than 500 m are always detected if they pass within 1 Fresnel scale of the star and can be detected even further away.

The expected number of occultation events in our survey due to KBOs with radii $r_1 < r < r_2$ can be estimated by

$$N(r_1 < r < r_2) \simeq \eta(r) n v_{rel} 2\mathcal{F}\Delta t \left(\left[\frac{r_1}{r_{break}} \right]^{-q+1} - \left[\frac{r_2}{r_{break}} \right]^{-q+1} \right) \qquad (6.1)$$

where v_{rel} is the typical relative velocity between the KBO and the observer and Δt is the total time of observations taken within 20 deg of the ecliptic. The detection efficiency for a given size KBO is $\eta(r)$ (see Fig. 6.10) and $\mathcal{F}$ is equal to 1 Fresnel

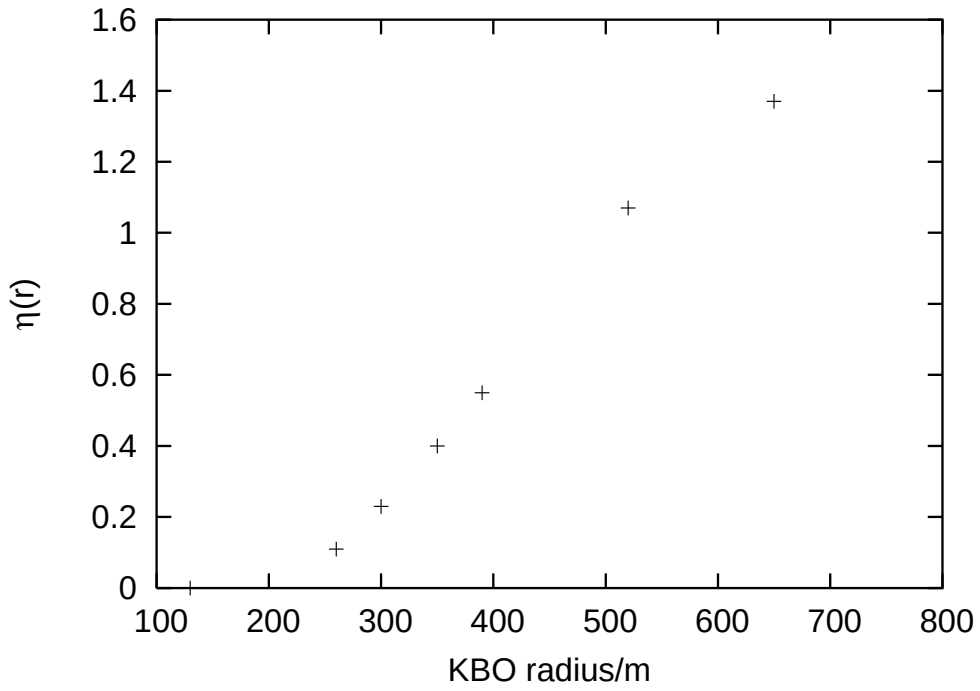

Figure 6.10 Detection efficiency, $\eta(r)$, of our FGS survey as a function of KBO radius, r. The detection efficiency is normalized by an impact parameter equal to 1 Fresnel scale, i.e., a detection efficiency of 1 means that all implanted events with impact parameters less than 1 Fresnel scale were successfully recovered, a detection efficiency of more than 1 means that, in addition, some events with impact parameters larger than 1 Fresnel scale were recovered. The detection efficiency of our survey is $\sim 10\%$ for objects with $r = 250$ m. It exceeds 100% for KBOs with $r > 500$ m. This means that objects larger than 500 m are always detected if they pass within 1 Fresnel scale of the star and can be detected even further away.

scale (i.e., 1.3 km) per our definition of $\eta(r)$. r_{break} is the radius at which the break is observed in the size distribution for larger KBOs. The number density of KBOs with sizes of r_{break} and larger, integrated along the line of sight to the star is given by n. Fuentes et al. (2009) report a break radius $r_{break} \sim 45$ km and a sky surface density for r_{break} sized KBOs of $\sim 23\,\mathrm{deg}^{-2}$, which translates to $n \sim 2 \times 10^{-25}$ cm^{-2}. Our entire FGS survey consists 37400 hours of observations that were taken within 20 deg of the ecliptic, a large fraction of the FGS observations are taken close to opposition in which case $v_{rel} \sim 26$ km/s (see discussion above). Figure 6.11 shows the expected number of events as a function of KBO radius for various size distributions. Most of the occultation events should be due to KBOs with radii of about 350 m. The total number of expected occultation events over the entire FGS survey is 52, 4, 0.3 for power-law slopes $q = 4$, 3.5, 3, respectively. Thus, with the completed survey, we will be able to distinguish between these 3 physically interesting size distributions.

6.5 Preliminary Results

We analyzed 3 years of archival FGS data, which corresponds to ∼21% of our entire FGS survey. These 3 years of FGS data consist of $\sim$ 7900 star hours of low ecliptic latitude ($-20\,\mathrm{deg} < i < +20\,\mathrm{deg}$) observations. We adapted a significance threshold of $\Delta\chi^2 > 63.1$, which corresponds to less than one false positive detection over the entire FGS data set (i.e., less than ~ 0.2 false positives in the data analyzed so far) and searched a relative velocity parameter space of 4-34 km/s. A total of 51 events were detected with a $\Delta\chi^2 > 63.1$. 40 out of the 51 events are due to a decrease in the read-out frequency (see Fig. 6.6 for an example) and are therefore clearly not related to an occultation event. 10 events show a very brief and rapid increase in photon counts, most likely due to cosmic rays. Both these type of events (i.e., the decreased sampling frequency and the cosmic rays) can be identified easily, since the former shows a correlation between successive read-outs and the latter gives a very poor χ^2 fit. One out of the 51 events, which has a $\Delta\chi^2$ of 67.3, displays a genuine looking occultation signature (see Fig. 6.12). The best fit parameters yield a relative

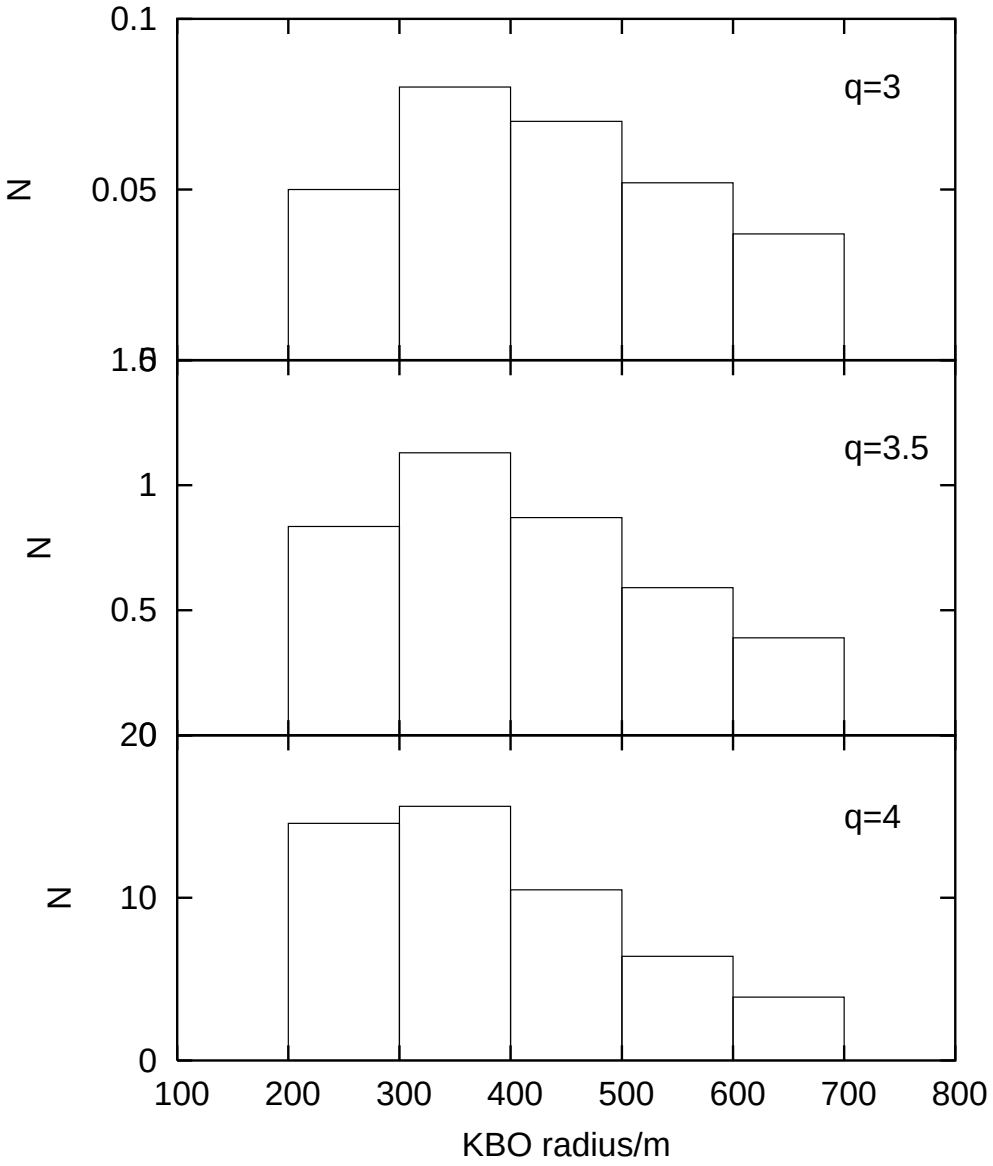

Figure 6.11 Expected number of events, N, as a function of KBO radius for various size distributions. Most of the occultation events should be due to KBOs with radii of about 350 m. The total number of expected occultation events is 52, 4, 0.3 for power-law slopes $q = 4$, 3.5, 3, respectively.

velocity between the KBO and the observer of $v_{rel} = 30.9^{+1.7}_{-1.2}$ km/s and a KBO size of $r = 486^{+54}_{-57}$ m. From the value of the $\Delta\chi^2$ alone the event has a 0.06 probability that it is caused by statistical fluctuations that lead to a false positive in the data analyzed so far. Once the entire FGS data set is analyzed, this probability will increase to 0.29. The actual probability for the candidate occultation event to be a false positive is about an order of magnitude less once the stellar properties and velocity information are taken into account (see discussion below).

6.5.1 PMTs and Instrumental Artifacts

There are several things that we can test for this event. Each FGS consists of 4 PMTs. We can, therefore, examine the photon counts recorded in PMT 1 & 2 and compare them with those recored in PMT 3 & 4. Note, we cannot compare the photon counts of PMT 1 with that of PMT 2 since they are not independent (see §6.2 for details), the same is ture for PMT 3 and 4. The upper right- and left-hand side of Figure 6.13 show that the occultation signal is present in the combined photon count of PMT 1 & 2 and PMT 3 & 4, respectively. The signal is therefore not caused by some artifact related to the PMTs. The combined photon count of all 4 PMTs is shown in the lower left corner of Figure 6.13. Next we can check if the signal was caused by some instrument jitter or day/night-time variations of HST by comparing the photon counts recorded by two different FGS at a given time. The two FGS are operating simultaneously, but each monitors a different guide star. The photon count recorded by each FGS is therefore different, but global instrumental artifacts will display in both FGS. The lower panel of Figure 6.13 shows the photon counts that were recorded by two different FGS at the same time. The occultation signal is only present in one of them and is therefore not cause by instrument jitter or other global instrumental effects. Furthermore, we did not find any correlated noise in the photometric time series of the candidate occultation event.

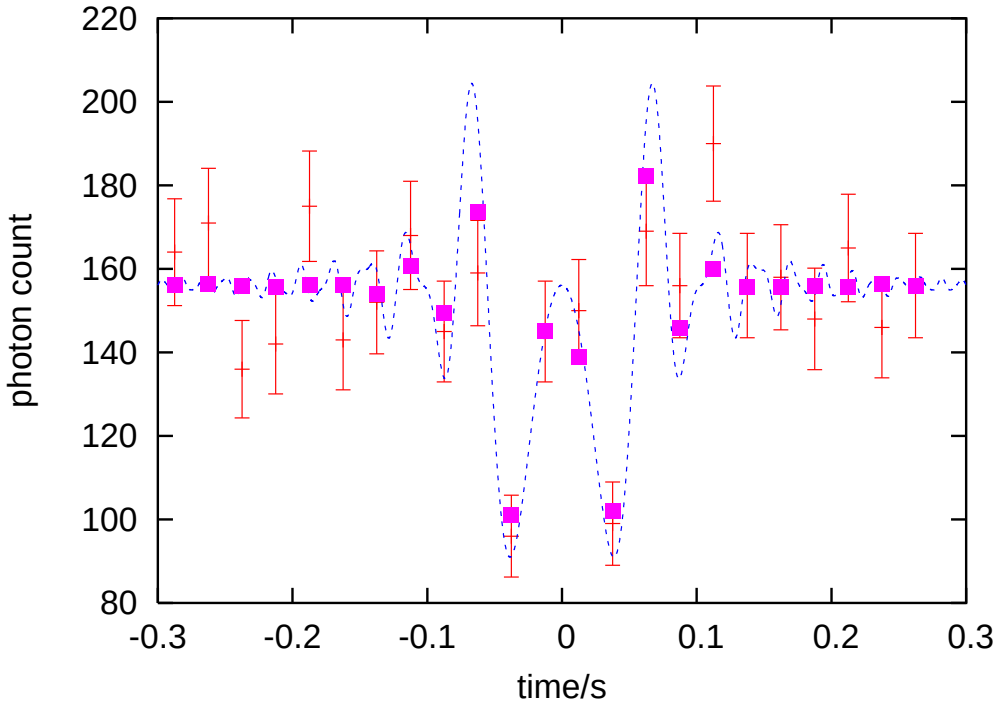

Figure 6.12 Photon count as a function of time of the candidate occultation event. The grey crosses and error bars are the FGS data points, the dashed line is the theoretical diffraction pattern, and the squares correspond to the theoretical light curve integrated over 40 Hz intervals. The best fit template yields a KBO radius of 486^{+54}_{-57} m and a relative velocity of $30.9^{+1.7}_{-1.2}$ km/s.

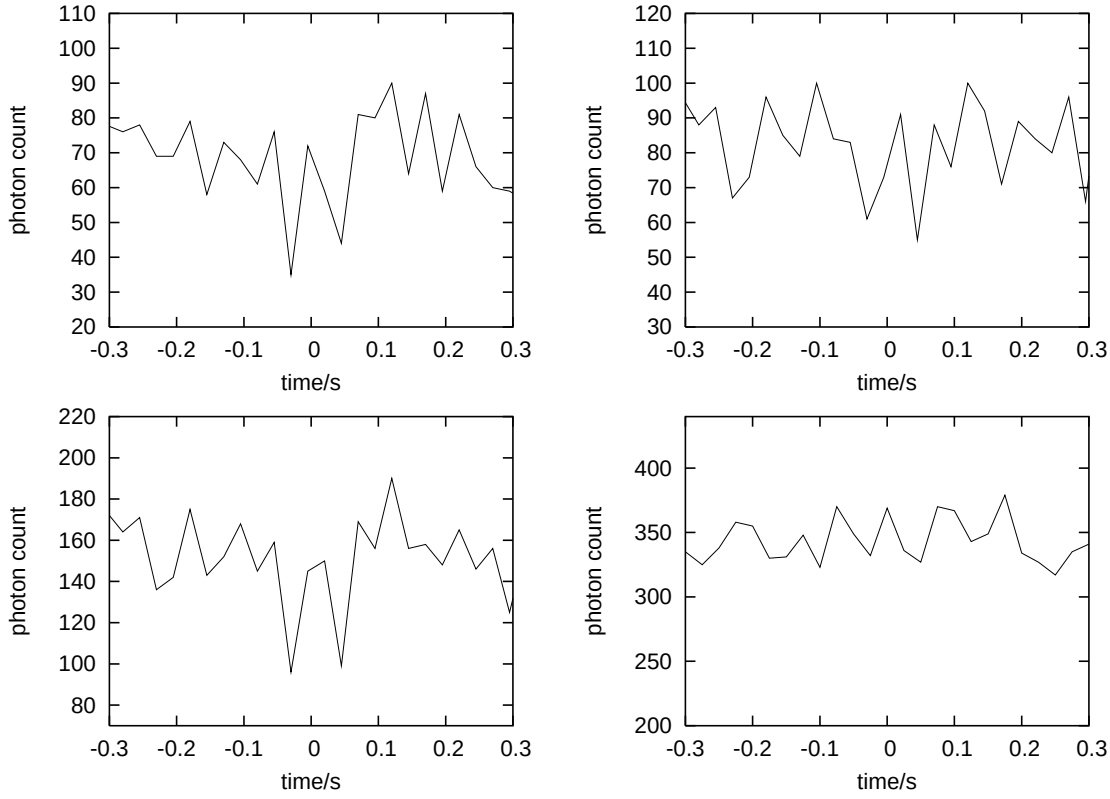

Figure 6.13 Photon counts as a function of time. The upper panel shows the occultation signal in the combined photon count of PMT 1 & 2 (left) and PMT 3 & 4 (right), respectively. The lower panel shows the combined photon count of all 4 PMTs of the occultation event (left) and the simultaneous photon count of the second FGS that was observing a different guide star (right).

6.5.2 Stellar Properties

In addition we checked if the stellar angular size and ecliptic latitude are consistent with an occultation event. The guide star has an ecliptic latitude of +14 and subtends an angular size of 0.3 of the Fresnel scale. Both are therefore consistent with an actual occultation event. The probability that a guide star has a low ecliptic latitude (i.e., $-20\,\mathrm{deg} \leq i \leq +20\,\mathrm{deg}$) that would be considered to be consistent with an occultation event is 0.34. This therefore reduces the probability that we might mistake a false positive for a real event by an additional factor of 0.34.

6.5.3 Relative Velocity

The relative velocity derived from the geometry of the observations, assuming that the KBO is on a circular orbit at 40 AU, is 32.8 km/s which is in good agreement with the relative velocity of $30.9^{+1.7}_{-1.2}$ km/s that was obtained from the best fit template of the occultation event. The actual velocity error is somewhat larger than just the estimate from the best-fit since an eccentric KBO can introduce a velocity error $\sim \pm 2$ km/s. The probability that the velocities from the fit and from the geometry of the observations agree to within ± 4 km/s by chance is 0.2 (see §6.4.2). The probability that we will mistake a false positive event for an occultation is therefore reduced by an additional factor of 0.2.

The probability that both the stellar properties and the velocity information agree with that of a candidate event by chance is given by the product of their respective probabilities (i.e., 0.2×0.34). Therefore, the chance that we will mistake a false positive event for an occultation event is reduced by a factor of 0.068 from the value inferred from the $\Delta\chi^2$ alone. For the event presented here, and the data we analyzed so far, this yields a probability of $0.06 \times 0.068 \sim 0.004$ (i.e., 0.4%) for being due to a false positive. This probability will increase to 2% once the entire FGS data set is analyzed. We therefore conclude that it is likely that the candidate event is a real occultation.

Figure 6.14 shows a comparison between the number of false positive events from

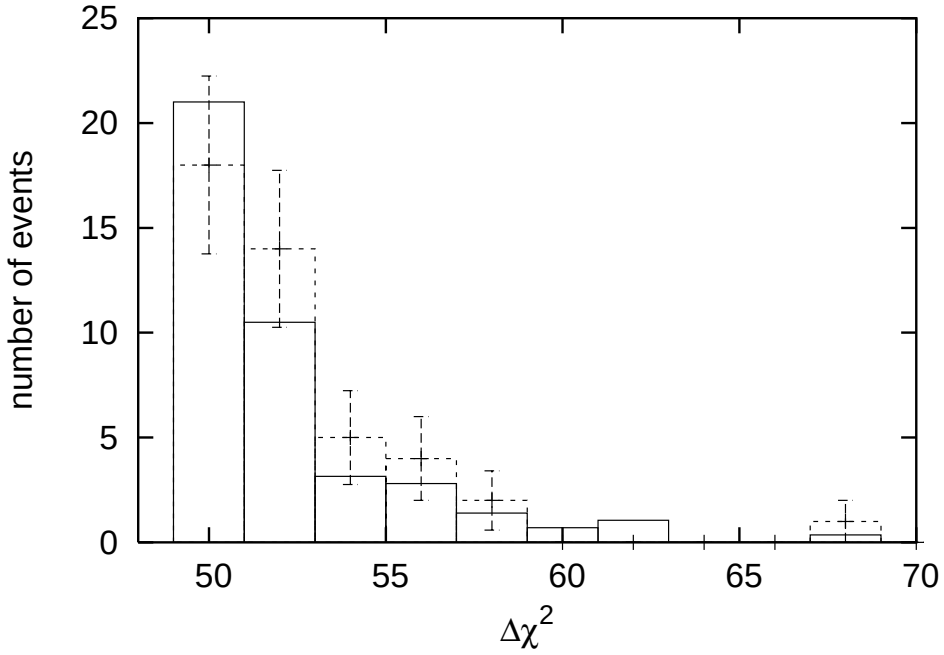

Figure 6.14 Histogram of number of events as a function of $\Delta\chi^2$. The solid line corresponds to the false positive events from the bootstrap method and were scaled to match exactly the same number of star hours as analyzed in our FGS survey to date. The dashed line and error bars correspond to the number of events detected in our FGS survey.

the bootstrap method and number of events detected in our survey to date. The number of false positives from the bootstrap method were scaled to match exactly the number of star hours analyzed in our FGS survey to date. Figure 6.14 suggests that there might be an excess in the number of events in the FGS data above the number of false positives from the bootstrap analysis, however, this excess is not statistically significant at this stage. If this excess is a real signal then it will become more pronounced as the remaining FGS data is analyzed. In the future we plan to examine the distribution of the detected events as a function of ecliptic latitude and plan to test whether the distributions of low and high ecliptic latitude observations differ.

6.6 Conclusion and Future Work

We presented here the analysis and first results from our archival FGS survey. Our current analysis spans 3 years of FGS data, which corresponds to ∼21% of the entire survey, and consist of ∼ 7900 star hours of low ecliptic latitude ($-20\,\mathrm{deg} < i < +20\,\mathrm{deg}$) observations. With only ∼ 21% of the data analyzed so far, our survey is already an order of magnitude more powerful than any ongoing visible-light search for KBO occultations. We reported our first candidate occultation event. We were not able to attribute the candidate event to instrumental artifacts (see §6.5) and show that its probability of being a false positive due to statistical fluctuations in the data is only 0.4%. We therefore conclude that it is likely that the candidate event is a real occultation. With the detection of at most one occultation we are able to constrain the surface density of KBOs with radii larger than 350m to $< 4.9 \times 10^7$ deg^{-2} at the 95% confidence level. This is the best constraint to date and improves the previous best estimate for the KBO surface density (Bianco et al., 2009) by an order of magnitude. We rule out a power-law index of $q > 3.9$ for the size distribution of sub-km sized KBOs at the 95% confidence level. This confirms that the size distribution of sub-km sized KBOs is shallower than that of larger KBOs (i.e., $r > 50$ km) and is consistent with the idea that small KBOs underwent collisional evolution that modified their size distribution.

In the future we will analyze the remaining FGS data which holds the promise for further occultation events. With the analysis of the entire data set we will be able to constrain the power-law index of the size distribution to values below 3.5, which means that we will be able to test whether small KBOs are dominated by material strength ($q = 3.5$, Dohnanyi (1969)) or held together predominately by gravity ($q \sim 3$, Pan & Sari (2005)). Finally, as part of this work, we are constructing an easy-to-access archive of the FGS observations, which we intend to make available to the entire astronomical community.

Acknowledgments First of all, I would like to thank Dr. Avishay Gal-Yam for having the excellent idea to use the archival FGS data to search for serendipitous stellar occultations. I would like to highlight the contributions of Dr. Eran Ofek and Dr. Michael Wenz to the work presented here. Dr. Eran Ofek calculated the stellar angular sizes, determined the ecliptic latitude distribution of the guide stars, analyzed the FGS data for correlated noise and calculated the velocity information for the observations. Dr. Mike Wenz extracted the FGS photometry streams from the files archived at GSFC, screened the data to retain only measurements taken in fine-lock mode and provided coordinates and magnitudes of the guide stars observed. Finally, I would like to thank my advisor, Dr. Re'em Sari, for the countless stimulating discussions we had about this project and for his guidance with the work presented here.

Chapter 7

Summary

In this thesis we have presented a series of theoretical projects ranging from planetesimal formation during the early stages of planet formation to the creation of multiple systems of Trans-Neptunian objects in the outer solar system. We conclude with an ongoing observational project that aims to detect sub-km sized objects in the Kuiper Belt. Our main results and conclusions are:

1. **Semi-collisional accretion may have given rise to the preference for prograde rotation observed in the terrestrial planets and, perhaps, the largest asteroids.**

We have shown that planetesimal accretion might be in the semi-collisional or collisional regime, which leads to the formation of a prograde accretion disk around the protoplanet. The accretion of such a disk gives rise to a maximally spinning protoplanets with prograde rotation. As a result of semi-collisional accretion, the final spin of a terrestrial planet after giant impacts is not completely random, but is biased toward prograde rotation. The dominance of prograde rotation might be increased further by the accretion of leftover planetesimals in the post-giant-impact phase, provided that semi-collisional or collisional accretion still applies. We suggest that in our solar system, semi-collisional accretion gave rise to the preference for prograde rotation observed in the terrestrial planets and, perhaps, the largest asteroids (Schlichting & Sari, 2007).

2. **For sub-Hill KBO velocities, binaries in the Kuiper Belt formed primarily due to dynamical friction (L^2s mechanism) rather than three-**

body encounters (L^3 mechanism), while for super-Hill velocities the L^3 mechanism dominates over the L^2s mechanism.

We accurately determined the L^2s and L^3 formation rates for sub-Hill velocities and showed that for sub-Hill velocities, binaries in the Kuiper Belt are formed primarily due to dynamical friction (L^2s Mechanism) rather than three-body encounters (L^3 Mechanism). This result is independent of the velocity dispersion of the small bodies in the Kuiper Belt, their surface density, and the importance of collisions among the small bodies. For super-Hill velocities the L^3 mechanism dominates over the L^2s mechanism. Binary formation via the L^3 mechanism competes with binary destruction by passing bodies. Given sufficient time, a statistical equilibrium abundance of binaries forms. We show that the frequency of long-lived transient binaries drops exponentially with the system's lifetime and that such transient binaries are not important for binary formation via the L^3 mechanism. For the L^2s mechanism we find that the typical time that transient binaries must last to form Kuiper Belt binaries (KBBs) increases only logarithmically with decreasing strength of dynamical friction. Longevity of transient binaries only becomes important for very weak dynamical friction and is most likely not crucial for KBB formation (Schlichting & Sari, 2008a)

3. **Binaries that form by dynamical friction (L^2s mechanism) are always retrograde**

We showed that various binary formation scenarios form prograde and retrograde binaries in different abundances. This is caused by stable retrograde orbits that exist much further out in the Hill sphere than prograde orbits. The relative abundance of prograde to retrograde binary orbits enables us, therefore, to differentiate between various proposed binary formation scenarios observationally, provided that the sense of the binary orbits was not altered after formation. We predict that if binary formation proceeded while sub-Hill velocities prevailed, the vast majority of all binaries with comparable masses formed with retrograde orbits. This dominance of retrograde binary orbits is a result of binary formation via the L^2s mechanism, or any

other mechanism that dissipates energy in a smooth and gradual manner. For super-Hill velocities, binary formation proceeds via the L^3 mechanism, which produces a roughly equal number of prograde and retrograde binaries (Schlichting & Sari, 2008b).

4. **Haumea's collisional family may have been ejected while in orbit around Haumea**

We proposed a new formation scenario for the Haumea family. In our scenario Haumea's initial giant impact forms a single moon that tidally evolves outward until it suffers a destructive collision from which the family is created. The advantage of this scenario is that it naturally gives rise to a lower velocity dispersion among the family members than expected from direct ejection from Haumea's surface. We show that this formation scenarios yields a velocity dispersion of $\sim$ 190m/s among the family members, which is in good agreement with the measured dispersion $\sim$ 140m/s in semi-major axis, eccentricity, and inclination of the family members (Brown et al., 2007; Ragozzine & Brown, 2007). Our formation scenario is consistent with the detection of one collisional family in the Kuiper Belt. Ejecting the family members from Haumea's orbit has the additional advantage that it is easy to reconcile with Haumea's initial giant impact. In our scenario Haumea's giant impact can occur before the excitation of the Kuiper belt and the ejection of the family members afterwards. One can therefore preserve the dynamical coherence of the family and explain Haumea's original giant impact whose collision timescale is a million times shorter in the primordial dynamically cold Kuiper Belt compared to the dynamically excited Kuiper Belt today. We suggest that Hi'iaka and Namaka, the two moons of Haumea, were produced in the same satellite-break-up that created the other family members, only that in their case the impulse was not sufficient to escape Haumea.

5. **The surface density of KBOs with radii larger than 350m is** $< 4.9 \times 10^7 \mathrm{deg}^{-2}$**.**

We searched for serendipitous stellar occultations in 3 years of archival FGS data consisting of $\sim$ 7900 star hours of low ecliptic latitude ($-20 < i < +20\,\mathrm{deg}$) observations. We constrain the surface density of KBOs with radii larger than 350m to

$< 4.9 \times 10^7 \mathrm{deg}^{-2}$ at the 95% confidence level. This improves the previous best estimate for the KBO surface density by an order of magnitude. We rule out a power-law index of $q > 3.9$ for the size distribution of sub-km sized KBOs at the 95% confidence level. Our findings confirm that the size distribution of sub-km sized KBOs is shallower than that of large KBOs (i.e., $r > 50$ km) and is consistent with the idea that small KBOs underwent collisional evolution that modified their size distribution. In addition, we present our first candidate occultation event and show that it is unlikely to be due to instrumental artifacts. Its probability of being a false positive due to statistical fluctuations in the data is only 0.4% and we conclude that it is likely that the candidate event is a real occultation.

A promising future for research in planet formation lies ahead. Ongoing ground-based surveys, as well as current and future space-based missions like Spitzer, Kepler and Wise, will continue to supply us with valuable observational constraints and are likely to surprise us with exciting new discoveries. The growing wealth of information on circumstellar disks, extrasolar planets and the Kuiper Belt continues to provide novel insights into planet formation and continues to improve our understanding of the origin of our solar system.

Bibliography

Agnor, C. & Asphaug, E. 2004, ApJ, 613, L157

Agnor, C. B., Canup, R. M., & Levison, H. F. 1999, Icarus, 142, 219

Alcock, C., Dave, R., Giammarco, J., Goldader, J., Lehner, M., King, S.-K., Lee, T., Wang, A., Wang, S.-Y., Wen, C.-Y., Chen, W. P., Cook, K., Marshall, S., Porrata, R., Byun, Y.-I., de Pater, I., Rice, J., & Lissauer, J. 2003, Earth Moon and Planets, 92, 459

Altenhoff, W. J., Bertoldi, F., & Menten, K. M. 2004, A&A, 415, 771

Astakhov, S. A., Lee, E. A., & Farrelly, D. 2005, MNRAS, 360, 401

Axelrod, T. S., Alcock, C., Cook, K. H., & Park, H.-S. 1992, in Astronomical Society of the Pacific Conference Series, Vol. 34, Robotic Telescopes in the 1990s, ed. A. V. Filippenko, 171–181

Bailey, M. E. 1976, Nature, 259, 290

Barkume, K. M., Brown, M. E., & Schaller, E. L. 2006, ApJ, 640, L87

Bean, J. L., Benedict, G. F., Charbonneau, D., Homeier, D., Taylor, D. C., McArthur, B., Seifahrt, A., Dreizler, S., & Reiners, A. 2008, A&A, 486, 1039

Benedict, G. F., McArthur, B., Chappell, D. W., Nelan, E., Jefferys, W. H., van Altena, W., Lee, J., Cornell, D., Shelus, P. J., Hemenway, P. D., Franz, O. G., Wasserman, L. H., Duncombe, R. L., Story, D., Whipple, A. L., & Fredrick, L. W. 1999, AJ, 118, 1086

Benz, W. & Asphaug, E. 1999, Icarus, 142, 5

Bernstein, G. M., Trilling, D. E., Allen, R. L., Brown, M. E., Holman, M., & Malhotra, R. 2004, AJ, 128, 1364

Bianco, F. B., Protopapas, P., McLeod, B. A., Alcock, C. R., Holman, M. J., & Lehner, M. J. 2009, ArXiv e-prints

Bickerton, S. J., Kavelaars, J. J., & Welch, D. L. 2008, AJ, 135, 1039

Binney, J. & Tremaine, S. 1987, Galactic dynamics (Princeton, NJ, Princeton University Press, 1987, 747 p.)

Blocker, A. W., Protopapas, P., & Alcock, C. R. 2009, ArXiv e-prints

Bottke, W. F., Durda, D. D., Nesvorný, D., Jedicke, R., Morbidelli, A., Vokrouhlický, D., & Levison, H. 2005, Icarus, 175, 111

Brown, M. E., Barkume, K. M., Ragozzine, D., & Schaller, E. L. 2007, Nature, 446, 294

Brown, M. E., Bouchez, A. H., Rabinowitz, D., Sari, R., Trujillo, C. A., van Dam, M., Campbell, R., Chin, J., Hartman, S., Johansson, E., Lafon, R., Le Mignant, D., Stomski, P., Summers, D., & Wizinowich, P. 2005, ApJ, 632, L45

Brown, M. E. & Suer, T.-A. 2007, IAU Circ, 8812, 1

Brown, M. E., van Dam, M. A., Bouchez, A. H., Le Mignant, D., Campbell, R. D., Chin, J. C. Y., Conrad, A., Hartman, S. K., Johansson, E. M., Lafon, R. E., Rabinowitz, D. L., Stomski, Jr., P. J., Summers, D. M., Trujillo, C. A., & Wizinowich, P. L. 2006a, ApJ, 639, L43

—. 2006b, ApJ, 639, L43

Cameron, A. G. W. & Ward, W. R. 1976, in Lunar and Planetary Institute Conference Abstracts, Vol. 7, Lunar and Planetary Institute Conference Abstracts, 120

Canup, R. M. 2004, Icarus, 168, 433

—. 2005, Science, 307, 546

Chambers, J. E. 2001, Icarus, 152, 205

Chandrasekhar, S. 1943, ApJ, 97, 255

Chang, H.-K., King, S.-K., Liang, J.-S., Wu, P.-S., Lin, L. C.-C., & Chiu, J.-L. 2006, Nature, 442, 660

Chapman, C. R. 1986, Memorie della Societa Astronomica Italiana, 57, 103

Collins, B. F. & Sari, R. 2006, AJ, 132, 1316

—. 2008, AJ, 136, 2552

Collins, B. F., Schlichting, H. E., & Sari, R. 2007, AJ, 133, 2389

Davidsson, B. J. R. & Gutiérrez, P. J. 2006, Icarus, 180, 224

Davis, D. R. & Farinella, P. 1997, Icarus, 125, 50

Davis, D. R., Weidenschilling, S. J., Farinella, P., Paolicchi, P., & Binzel, R. P. 1989, in Asteroids II, ed. R. P. Binzel, T. Gehrels, & M. S. Matthews, 805–826

Dohnanyi, J. W. 1969, J. Geophys. Res., 74, 2531

Dones, L. & Tremaine, S. 1993a, Icarus, 103, 67

—. 1993b, Science, 259, 350

Drummond, J. D., Fugate, R. Q., Christou, J. C., & Hege, E. K. 1998, Icarus, 132, 80

Dyson, F. J. 1992, QJRAS, 33, 45

Estrada, P. R. & Mosqueira, I. 2006, Icarus, 181, 486

Fabrycky, D. C. & Winn, J. N. 2009, ArXiv e-prints

Fischer, D. A. & Valenti, J. 2005, ApJ, 622, 1102

Fraser, W. C. & Brown, M. E. 2009, ApJ, 695, L1

Fraser, W. C. & Kavelaars, J. J. 2009, AJ, 137, 72

Fraser, W. C., Kavelaars, J. J., Holman, M. J., Pritchet, C. J., Gladman, B. J., Grav, T., Jones, R. L., Macwilliams, J., & Petit, J.-M. 2008, Icarus, 195, 827

Fuentes, C. I., George, M. R., & Holman, M. J. 2009, ApJ, 696, 91

Fuentes, C. I. & Holman, M. J. 2008, AJ, 136, 83

Funato, Y., Makino, J., Hut, P., Kokubo, E., & Kinoshita, D. 2004, Nature, 427, 518

Gil-Hutton, R. 1997, Planet. Space Sci., 45, 229

Goldreich, P., Lithwick, Y., & Sari, R. 2002, Nature, 420, 643

—. 2004a, ApJ, 614, 497

—. 2004b, ARA&A, 42, 549

Goldreich, P. & Tremaine, S. 1980, ApJ, 241, 425

Greaves, J. S., Holland, W. S., Wyatt, M. C., Dent, W. R. F., Robson, E. I., Coulson, I. M., Jenness, T., Moriarty-Schieven, G. H., Davis, G. R., Butner, H. M., Gear, W. K., Dominik, C., & Walker, H. J. 2005, ApJ, 619, L187

Grundy, W. M., Noll, K. S., & Stephens, D. C. 2005a, Icarus, 176, 184

—. 2005b, Icarus, 176, 184

Grundy, W. M., Noll, K. S., Virtanen, J., Muinonen, K., Kern, S. D., Stephens, D. C., Stansberry, J. A., Levison, H. F., & Spencer, J. R. 2008, Icarus, 197, 260

Haisch, Jr., K. E., Lada, E. A., & Lada, C. J. 2001, ApJ, 553, L153

Hamilton, D. P. & Burns, J. A. 1991, Icarus, 92, 118

Hamilton, D. P. & Krivov, A. V. 1997, Icarus, 128, 241

Harrison, T. E., McNamara, B. J., Szkody, P., & Gilliland, R. L. 2000, AJ, 120, 2649

Hartmann, W. K. & Davis, D. R. 1975, Icarus, 24, 504

Hayashi, C. 1981, Progress of Theoretical Physics Supplement, 70, 35

Henon, M. 1970, A&A, 9, 24

Henon, M. & Petit, J.-M. 1986, Celestial Mechanics, 38, 67

Hill, G. W. 1878, Am. J. Math., 1, 5

Hillenbrand, L. A. 2008, Physica Scripta Volume T, 130, 014024

Holsapple, K. A. 1994, Planet. Space Sci., 42, 1067

Ida, S. 1990, Icarus, 88, 129

Innanen, K. A. 1979, AJ, 84, 960

Jewitt, D., Luu, J., & Marsden, B. G. 1992, IAU Circ, 5611, 1

Jones, T. A., Levine, A. M., Morgan, E. H., & Rappaport, S. 2008, ApJ, 677, 1241

Kalas, P., Graham, J. R., & Clampin, M. 2005, Nature, 435, 1067

Kenyon, S. J. & Luu, J. X. 1999, AJ, 118, 1101

Laskar, J. & Robutel, P. 1993, Nature, 361, 608

Lee, E. A., Astakhov, S. A., & Farrelly, D. 2007, MNRAS, 379, 229

Lehner, M. J., Alcock, C., Axelrod, T., Bianco, F., Byun, Y.-I., Chen, W.-P., Cook, K. H., Dave, R., de Pater, I., Giammarco, J., King, S.-K., Lee, T., Lissauer, J., Marshall, S. L., Mondal, S., Nihei, T., Rice, J., Schwamb, M., Wang, A., Wang, S.-Y., Wen, C.-Y., & Zhang, Z.-W. 2006, Astronomische Nachrichten, 327, 814

Levison, H. F., Morbidelli, A., Vokrouhlický, D., & Bottke, W. F. 2008, AJ, 136, 1079

Lissauer, J. J., Berman, A. F., Greenzweig, Y., & Kary, D. M. 1997, Icarus, 127, 65

Lissauer, J. J. & Kary, D. M. 1991, Icarus, 94, 126

Lissauer, J. J. & Safronov, V. S. 1991, Icarus, 93, 288

Love, S. G. & Ahrens, T. J. 1997, Nature, 386, 154

Magnusson, P., Barucci, M. A., Drummond, J. D., Lumme, K., & Ostro, S. J. 1989, in Asteroids II, ed. R. P. Binzel, T. Gehrels, & M. S. Matthews, 67–97

Malhotra, R., Duncan, M. J., & Levison, H. F. 2000, Protostars and Planets IV, 1231

Mayor, M. & Queloz, D. 1995, Nature, 378, 355

McArthur, B. E., Benedict, G. F., Lee, J., van Altena, W. F., Slesnick, C. L., Rhee, J., Patterson, R. J., Fredrick, L. W., Harrison, T. E., Spiesman, W. J., Nelan, E., Duncombe, R. L., Hemenway, P. D., Jefferys, W. H., Shelus, P. J., Franz, O. G., & Wasserman, L. H. 2001, ApJ, 560, 907

McCue, J. & Dormand, J. R. 1993, Earth Moon and Planets, 63, 209

McKinnon, W. B. 1989, ApJ, 344, L41

Melosh, H. J., Nemchinov, I. V., & Zetzer, Y. I. 1994, in Hazards Due to Comets and Asteroids, ed. T. Gehrels, M. S. Matthews, & A. M. Schumann, 1111–1132

Melosh, H. J. & Ryan, E. V. 1997, Icarus, 129, 562

Nesvorný, D., Enke, B. L., Bottke, W. F., Durda, D. D., Asphaug, E., & Richardson, D. C. 2006, Icarus, 183, 296

Noll, K. S., Grundy, W. M., Chiang, E. I., Margot, J.-L., & Kern, S. D. Binaries in the Kuiper Belt (The Solar System Beyond Neptune), 345–363

Ortiz, J. L., Sota, A., Moreno, R., Lellouch, E., Biver, N., Doressoundiram, A., Rousselot, P., Gutiérrez, P. J., Márquez, I., González Delgado, R. M., & Casanova, V. 2004, A&A, 420, 383

Pan, M. & Sari, R. 2005, Icarus, 173, 342

Petit, J.-M. & Henon, M. 1986, Icarus, 66, 536

Petit, J.-M., Kavelaars, J., Gladman, B., & Laredo, T. Size Distribution of Multikilometer Transneptunian Objects (The Solar System Beyond Neptune), 71–87

Petit, J.-M., Kavelaars, J., Gladman, B., Margot, J. L., Nicholson, P., Jones, R., Parker, J., Ashby, M., & Campo Bagatin, A. 2009, in AAS/Division for Planetary Sciences Meeting Abstracts, Vol. 40, AAS/Division for Planetary Sciences Meeting Abstracts, 47.11

Pravec, P., Harris, A. W., & Michalowski, T. 2002, Asteroids III, 113

Rabinowitz, D. L., Barkume, K., Brown, M. E., Roe, H., Schwartz, M., Tourtellotte, S., & Trujillo, C. 2006, ApJ, 639, 1238

Rabinowitz, D. L., Schaefer, B. E., Schaefer, M., & Tourtellotte, S. W. 2008, AJ, 136, 1502

Rafikov, R. R. 2003, AJ, 125, 942

Ragozzine, D. & Brown, M. E. 2007, AJ, 134, 2160

—. 2009, ArXiv e-prints

Roques, F., Doressoundiram, A., Dhillon, V., Marsh, T., Bickerton, S., Kavelaars, J. J., Moncuquet, M., Auvergne, M., Belskaya, I., Chevreton, M., Colas, F., Fernandez, A., Fitzsimmons, A., Lecacheux, J., Mousis, O., Pau, S., Peixinho, N., & Tozzi, G. P. 2006, AJ, 132, 819

Roques, F., Moncuquet, M., Lavillonière, N., Auvergne, M., Chevreton, M., Colas, F., & Lecacheux, J. 2003, ApJ, 594, L63

Safronov, V. S., Pechernikova, G. V., Ruskol, E. L., & Vitiazev, A. V. 1986, Protosatellite swarms (IAU Colloq. 77: Some Background about Satellites), 89–116

Santos, N. C., Israelian, G., & Mayor, M. 2004, A&A, 415, 1153

Sari, R. & Goldreich, P. 2006, ApJ, 642, L65

Schlichting, H. E. & Sari, R. 2007, ApJ, 658, 593

—. 2008a, ApJ, 673, 1218

—. 2008b, ApJ, 686, 741

Stansberry, J., Grundy, W., Brown, M., Cruikshank, D., Spencer, J., Trilling, D., & Margot, J.-L. Physical Properties of Kuiper Belt and Centaur Objects: Constraints from the Spitzer Space Telescope (The Solar System Beyond Neptune), 161–179

Stapelfeldt, K. R., Holmes, E. K., Chen, C., Rieke, G. H., Su, K. Y. L., Hines, D. C., Werner, M. W., Beichman, C. A., Jura, M., Padgett, D. L., Stansberry, J. A., Bendo, G., Cadien, J., Marengo, M., Thompson, T., Velusamy, T., Backus, C., Blaylock, M., Egami, E., Engelbracht, C. W., Frayer, D. T., Gordon, K. D., Keene, J., Latter, W. B., Megeath, T., Misselt, K., Morrison, J. E., Muzerolle, J., Noriega-Crespo, A., Van Cleve, J., & Young, E. T. 2004, ApJS, 154, 458

Stern, S. A. & Colwell, J. E. 1997, ApJ, 490, 879

Stern, S. A., Weaver, H. A., Steffl, A. J., Mutchler, M. J., Merline, W. J., Buie, M. W., Young, E. F., Young, L. A., & Spencer, J. R. 2006, Nature, 439, 946

Thomas, P. C., Parker, J. W., McFadden, L. A., Russell, C. T., Stern, S. A., Sykes, M. V., & Young, E. F. 2005, Nature, 437, 224

Trujillo, C. A. & Brown, M. E. 2003, Earth Moon and Planets, 92, 99

Trujillo, C. A., Jewitt, D. C., & Luu, J. X. 2001, AJ, 122, 457

Weaver, H. A., Stern, S. A., Mutchler, M. J., Steffl, A. J., Buie, M. W., Merline, W. J., Spencer, J. R., Young, E. F., & Young, L. A. 2006, Nature, 439, 943

Weidenschilling, S. J. 2002, Icarus, 160, 212

Weidenschilling, S. J., Spaute, D., Davis, D. R., Marzari, F., & Ohtsuki, K. 1997, Icarus, 128, 429

Wetherill, G. W. & Stewart, G. R. 1993, Icarus, 106, 190

Zhang, S.-P. & Innanen, K. A. 1988, Icarus, 75, 105

Zhang, Z.-W., Bianco, F. B., Lehner, M. J., Coehlo, N. K., Wang, J.-H., Mondal, S., Alcock, C., Axelrod, T., Byun, Y.-I., Chen, W. P., Cook, K. H., Dave, R., de Pater, I., Porrata, R., Kim, D.-W., King, S.-K., Lee, T., Lin, H.-C., Lissauer, J. J., Marshall, S. L., Protopapas, P., Rice, J. A., Schwamb, M. E., Wang, S.-Y., & Wen, C.-Y. 2008, ApJ, 685, L157